Doklady Physics, Vol. 50, No. 6, 2005, pp. 283–285. Translated from Doklady Akademii Nauk, Vol. 402, No. 4, 2005, pp. 472–474.

PHYSICS

Problems and Horizons of the Search for Tracks of Heavy and Superheavy Nuclei in Olivine Crystals from Meteorites (OLIMPIYA Project)

Academician V. L. Ginzburg, Academician E. L. Feĭnberg, N. G. Polukhina, N. I. Starkov, and V. A. Tsarev

Received February 1, 2005

In this paper, we consider the nuclear-physical and astrophysical aspects of investigations associated with the search for heavy and superheavy nuclei in the composition of cosmic rays. We also discuss the potentiality of searching for tracks of these nuclei in the olivine crystals found in meteorites with the use of the completely automated PAVICOM setup, which was designed for the scanning and processing of tracks of particles.

The detection of heavy and superheavy nuclei of cosmic rays and the search for transfermium nuclei with charges $Z \geq 110$ are among the most important and topical problems of modern nuclear physics and astrophysics [1].

1. The question of the existence of superheavy nuclei is of the utmost importance for understanding the properties of nuclear matter. What is of interest here is, first of all, verifying the considerable enhancement of nuclear stability that has been predicted [2] near the magic numbers $Z = 114$ and $N = 184$ (N is the number of neutrons in a nucleus), which may result in the existence of so-called stability islands for the superheavy nuclei in this region. The very first corroboration of this prediction was recently obtained at the JINR during the accelerator experiments carried out under the supervision of Yu.Ts. Oganesyan, in which the 114th and 116th elements were discovered [3]. In spite of this success, the search for superheavy nuclei is in fact continued. Moreover, the results of the Dubna experiment provide an impetus to the continuation of these searches. Only two events associated with a nucleus having $Z = 114$ and one event associated with $Z = 116$ were detected in this experiment. Undoubtedly, these results call for further verification and confirmation. It is also necessary to search for other possible superheavy nuclei. If the regularities associated with the magic numbers continue to hold for very large values of N and Z, the existence of stability islands for even heavier nuclei must not be ruled out.

Verification of the existence of unusual stable forms of nuclear matter containing, for example, strange [4] or other even heavier quarks [5] would also be of obvious interest.

2. The measurement of fluxes and of the spectra of heavy and superheavy nuclei composing cosmic rays is a sensitive method for studying the composition of cosmic-ray sources, the processes occurring in both the sources and the interstellar medium through which the cosmic rays propagate, as well as the models of cosmic-ray confinement in the galaxy. There are extremely limited experimental data available on the abundance of heavy nuclei (i.e., those with $Z > 30$) and on the spectra and fluxes of these nuclei, while reasonably reliable data on transfermium nuclei are entirely absent. Absent, as well, are any data on the possible existence of exotic superheavy nuclei.

The current notion is that atomic nuclei, beginning with the carbon and heavier ones, are produced in the interior of stars and during supernova explosions. Heavy and superheavy chemical elements located on the periodic table beyond bismuth are formed in the course of rapid processes (r-processes) occurring at high neutron concentrations and may give rise to superheavy nuclei with neutron numbers up to $N = 184$.

In addition to these traditional mechanisms, the possibility of producing very heavy nuclei (with mass numbers up to 500) at high neutron densities (on the order of 10^{30} cm^{-3}) and moderate temperatures ($T \leq 10^8$ K) has also been discussed [6]. This scenario could be realized in nonequilibrium shells of neutron stars, eruptions from which would give rise to the appearance of superheavy nuclei in the interstellar medium, stars, and planets [7].

As mentioned above, along with normal superheavy nuclei consisting of protons and neutrons, the possibility of the existence of other stable forms of nuclear matter containing strange and other even heavier quarks

Lebedev Physical Institute, Russian Academy of Sciences, Leninskiĭ pr. 53, Moscow, 117924 Russia
e-mail: polukhina@sci.lebedev.ru

1028-3358/05/5006-0283$26.00

also is an object of speculation [4, 5]. Particles of such matter in the form of exotic superheavy nuclei (strangelets, technets, etc.) retained since the early-universe epoch or produced in astrophysical objects could be present in the cosmic-ray flux. The aforementioned theoretical schemes call for thorough verification and comparison against experimental data.

Initially, the experimental search for superheavy nuclei in cosmic rays was carried out with the use of thick nuclear-emulsion layers exposed on balloons in the upper atmosphere [8]. Later, multilayer detectors made of polymeric materials in combination with Cherenkov detectors were also employed for this purpose [9]. In addition, tracks of superheavy cosmic-ray nuclei in meteoritic silicate olivine crystals were sought in some laboratories, including JINR, where these studies were carried out under the supervision of G.N. Flerov. An efficient procedure was developed for revealing tracks on the basis of annealing and etching samples. Among the found tracks of nuclei with $Z \geq 60$, about 150 were assigned to tracks of uranium-group nuclei. A 365-μm-long track was also found, which could be attributed to a nucleus with $Z \geq 110$ [10–12].

3. Recently, a group of researchers from the Lebedev Physical Institute (LPI) proposed the OLIMPIYA experiment (Olivines from meteorites: search for heavy and superheavy nuclei). In this experiment, it is suggested that the PAVICOM modern high-performance completely automated measuring setup developed at this Institute for scanning samples of olivine crystals from meteorites, will be used with the goal of searching for and processing tracks of heavy and superheavy cosmic-ray nuclei. Employment of this automated setup provides fundamental advantages in terms of processing rate, measurement accuracy, and reliability.

In common with previous studies on olivines, the OLIMPIYA experiment is based on the application of the solid-state track-detector technique, in which the radiation damages produced by ionizing particles in the detector material are used to detect these particles. In the search for relict tracks that are produced by cosmic-ray particles in minerals incorporated into some meteorites [10–13], use is made of the ability of silicate crystals from meteorites (olivine, pyroxene) to register and preserve over a long period of time ($>10^8$ yr) tracks of nuclei with $Z \geq 20$ [14]. The typical age of meteorites and, consequently, the time of their irradiation by the cosmic ray flux, is estimated as 10^7–10^9 yr. Therefore, meteorites can contain a wealth of tracks of cosmic-ray nuclei. According to the estimates obtained in [10–12], for the time of 10^8 yr, in 1 cm^3 of such crystals located at a depth of ≤5 cm beneath the preatmospheric meteorite surface, 10^2–10^3 tracks of nuclei with $Z \geq 90$ could be produced. At the same time, in crystals from the meteorite-surface areas (depth ≤1 cm), this number could be as high as 10^4.

Therefore, the employment of the long exposure time of meteorites in space provides for the tremendous advantage of this method as compared to methods based on the use of various satellite-borne and balloon-borne detectors. By measuring track parameters and the depth variation of the track diameter as the particle penetrates into the meteorite, one can not only identify particles but also determine their spectra.

The sample scanning and measurement of characteristics of particle tracks are both the most important and laborious parts of the work on track revealing and studying in solid-state track detectors (in particular, in olivine crystals). Visual scanning with a microscope by an operator is highly time consuming. It requires strenuous and exhausting work and actually sets limits on the feasibility of the track technique because it predetermines the low event statistic. Moreover, the results obtained are difficult to verify in terms of the possible malfunctions that arise in the course of data processing (for example, the loss of particle tracks by operators and other errors).

The novelty of the proposed approach consists principally in the means it provides for tackling these difficulties. This has become feasible owing to the progress achieved in the last few years in the production of a precision technique and the advent of optical tables with the high-precision movement on computer commands, the widespread use of modern charge-coupled devices for detection and digitization of optical images, and the high potentialities of modern computers. Taken together, these achievements make possible the complete automation of scanning and measurements and speed up data processing by approximately three orders of magnitude as compared to that achieved when so-called semiautomatic devices are used.

In Russia, the PAVICOM is the only completely automated setup combining two devices of this kind. This setup was constructed at the Lebedev Physical Institute, Russian Academy of Sciences [15] for processing data of both nuclear emulsions and solid-state track detectors that are used in nuclear and high-energy physics. Currently (from the middle of 2000), the PAVICOM is being successfully used by scientists of the LPI and by groups from a number of Russian Institutes (JINR, ITEP, MSU, INR, etc.). In the OLIMPIYA project, problems associated with scanning and measurements will be solved through the use of the PAVICOM.

The PAVICOM program package for seeking and processing tracks provides scanning over three coordinates, and the determination of characteristics of found tracks including their lengths with an accuracy of about 1 μm. Image sewing is also performed if the track length exceeds the size of the microscope field of view. In the case of intersecting tracks, the events are automatically recognized, and each track is processed separately. Upon etching olivine, dislocation zones and other defects can look like nuclear tracks. Therefore, the tracks are analyzed from their origin to the vertex so that they may be distinguished from etched defects.

The result of the proposed study would be a track-length distribution that both enables the charge distribution in the flux of galactic cosmic particles to be estimated and makes it possible to search for superheavy nuclei.

REFERENCES

1. V. L. Ginzburg, Usp. Fiz. Nauk **169**, 419 (1999) [Phys. Usp. **42**, 353 (1999)].
2. V. M. Strutinsky, Nucl. Phys. A **95**, 420 (1967).
3. Yu. Ts. Oganesyan, Vestn. Ross. Akad. Nauk **71**, 590 (2001).
4. De Rujula and S. L. Glashow, Nature **312**, 734 (1984).
5. J. A. Frieman and G. F. Guidice, Nucl. Phys. B **355**, 162 (1991).
6. Ya. B. Zeldovich, Zh. Éksp. Teor. Fiz. **38**, 1123 (1960).
7. G. S. Bisnovatyĭ-Kogan and V. M. Chechetkin, Usp. Fiz. Nauk **127**, 263 (1979) [Sov. Phys. Usp. **22**, 89 (1979)].
8. P. H. Fowler, C. Alexandre, V. H. Clapham, *et al.*, in *Proc. 15th ICRC, Plovdiv, 1977*, Vol. 11, p. 165.
9. E. K. Shirk and P. B. Price, Astrophys. J. **220**, 719 (1978).
10. V. P. Perelygin and S. G. Stetsenko, Pis'ma Zh. Éksp. Teor. Fiz. **32**, 622 (1980).
11. D. Lhagvasuren, O. Otgonsuren, V. P. Perelygin, *et al.*, *Solid-State Nuclear Track Detectors*, Ed. by Francaus *et al.* (Pergamon Press, New York, 1980).
12. V. P. Perelygin and S. G. Stetsenko, Pis'ma Zh. Éksp. Teor. Fiz. **49**, 257 (1989).
13. D. Lai, Space Sci. Rev. **14**, 3 (1972).
14. R. L. Fleischer, P. B. Price, R. M. Walker, *et al.*, J. Geophys. Res. **72**, 331 (1967).
15. A. B. Aleksandrov, I. Yu. Apacheva, E. L. Feinberg, *et al.*, Nucl. Instrum. Methods Phys. Res. A **535**, 542 (2004).

Translated by V. Tsarev

Doklady Physics, Vol. 50, No. 6, 2005, pp. 286–289. Translated from Doklady Akademii Nauk, Vol. 402, No. 4, 2005, pp. 475–478.

PHYSICS

Radiative Transitions of High-Energy Neutrinos in a Dense Medium

A. E. Lobanov

Presented by Academician A.A. Slavnov November 24, 2004

Received December 3, 2004

As massive neutrinos propagate through a dense medium, electromagnetic radiation caused by constituent fermions of the medium can arise [1, 2]. In this case, by virtue of radiative self-polarization, a neutrino can change its helicity. As distinct from Cherenkov radiation, this effect does not disappear even if the refractive index of the medium is considered to be unity. This conclusion is true for the model of neutrino interactions that violate spatial parity. On the basis of analogy with the dependence of synchrotron-radiation power on electron spin orientation, such an effect was called the neutrino spin light (see [3]).

The quasi-classical theory of radiation and of the radiative self-polarization of neutral particles has served a basis for the description of spin-light properties [4, 5]. This theory employs the Bargmann–Michel–Telegdi equation [6] and its generalizations [7, 8]. The applicability of this theory is restricted by the condition of the low energy of emitted photons compared to the energy of a radiating particle. This condition narrows the region of astrophysical applications in which the results obtained can be used.

In this paper, based on the successive quantum approach, we study the properties of spin light, making it possible to allow for neutrino recoil in the radiation emission process. Thereby, the above-indicated restriction is eliminated. On the other hand, detailed analysis of the results obtained shows that the possibility that the effect will arise depends on the neutrino type, neutrino helicity, and on the composition of the medium. This allows us to draw the conclusion that depending on the situation, the spin light can be a cause both of neutrino transition from the active form to the virtually sterile one and of the inverse process.

When the substance is sufficiently dense and the neutrino interaction with fermions of the medium is considered to be coherent, the neutrino propagation in the substance is described by the Dirac equation with the effective potential given in [9, 10]. In the framework of the minimally extended standard model, and for the uniform and isotropic medium under consideration, the form of this equation is unambiguously determined by arguments similar to those given in [11]:

$$\left(i\hat{\partial} - \frac{1}{2}\hat{f}(1+\gamma^5) - m_\nu\right)\Psi_\nu = 0. \quad (1)$$

The function f^μ is a linear combination of current 4-vectors and polarizations of fermions of the medium. If the medium is immobile and unpolarized, then $\mathbf{f} = 0$. The f^0 component calculated in the lowest order of the perturbation theory is determined by the formula (see [12–14])

$$f^0 = \sqrt{2}G_F\left\{\sum_f (I_{e\nu} + T_3^{(f)} - 2Q^{(f)}\sin^2\theta_W)(n_f - n_{\bar{f}})\right\}. \quad (2)$$

Here, n_f, $n_{\bar{f}}$ are, respectively, the densities of fermions and antifermions in the medium, $T_3^{(f)}$ is the third component of the weak isospin, and $Q^{(f)}$ is the electric charge. The parameter $I_{e\nu} = 1$ for the interaction of an electron neutrino with electrons of the medium; in other cases, $I_{e\nu} = 0$. The summation is performed for all fermions.

We now analyze the process of photon emission by a massive neutrino in such a medium. In the case of spontaneous radiation, the probability of a radiative transition for a neutral fermion with an anomalous magnetic moment μ_0 is determined by the formula[1]

$$P = -\frac{1}{2p^0}\int d^4x\, d^4y \int \frac{d^4q\, d^4k}{(2\pi)^6}\delta(k^2)\delta(q^2 - m_\nu^2) \times \mathrm{Sp}\{\Gamma_\mu(x)\varrho_i(x, y; p, \zeta_i)\Gamma_\nu(y)\varrho_f(y, x; q, \zeta_f)\} \times \varrho_{ph}^{\mu\nu}(x, y; k). \quad (3)$$

Moscow State University, Vorob'evy gory, Moscow, 119992 Russia
e-mail: lobanov@th466.phys.msu.ru

[1] In the formula for the radiation energy $\mathscr{E}$, the common multiplier k^0, i.e., the emitted-photon energy, appears in the integrand.

1028-3358/05/5006-0286$26.00

Here, $\varrho_i(x, y; p, \zeta_i)$ and $\varrho_f(y, x; q, \zeta_f)$ are the density matrices of the initial (i) and final (f) states of particles, $\varrho_{ph}^{\mu\nu}(x, y; k)$ is the density matrix of an emitted photon, and the vertex function is $\Gamma^\mu = -\sqrt{4\pi}\,\mu_0\sigma^{\mu\nu}k_\nu$. The density matrix for a longitudinally polarized neutrino in the immobile unpolarized medium, which was constructed with allowance for the solutions of Eq. (1), is of the form

$$\varrho(x, y; p, \zeta) = \frac{1}{2}\Delta_{p\zeta}^2(\hat{p} + m_\nu)(1 - \zeta\gamma^5\hat{S}_p) \times e^{-i(x^0 - y^0)(p^0 + f^0/2) + i(\mathbf{x} - \mathbf{y})\mathbf{p}\Delta_{p\zeta}}, \quad (4)$$

where p^μ is the neutrino kinetic momentum, $\Delta_{p\zeta} = 1 + \frac{\zeta f^0}{2|\mathbf{p}|}$, and $S_p^\mu = \left\{\frac{|\mathbf{p}|}{m_\nu}, \frac{p^0\mathbf{p}}{|\mathbf{p}|m_\nu}\right\}$. Thus, $\zeta = \pm 1$ determines the sign of the spin projection onto the direction of the neutrino kinetic momentum.

The calculated results can be conveniently expressed in terms of the dimensionless variables $\gamma = \frac{p^0}{m_\nu}$, $d = \frac{|f^0|}{2m_\nu}$, $\bar{\zeta}_{i,f} = \zeta_{i,f}\operatorname{sgn} f^0$. The transition probability per unit of time is determined by the formula

$$W_{\bar{\zeta}_f} = \frac{\mu_0^2 m_\nu^3}{4}\{(1 + \bar{\zeta}_f)[Z(z_1, 1)\Theta(\gamma - \gamma_1) + Z(z_2, -1)\Theta(\gamma - \gamma_2)] + (1 - \bar{\zeta}_f)[Z(z_1, 1)\Theta(\gamma_1 - \gamma) + Z(z_2, -1)\Theta(\gamma_2 - \gamma)] \times \Theta(\gamma - \gamma_0)\}(1 - \bar{\zeta}_i). \quad (5)$$

Here,

$$Z(z, \bar{\zeta}_f) = \frac{1}{\gamma(\gamma^2 - 1)}\left\{\ln z\left[\gamma^2 + d\sqrt{\gamma^2 - 1} + d^2 + \frac{1}{2}\right] + \frac{1}{4}(z^2 - z^{-2})\left[d^2(2\gamma^2 - 1) + d\sqrt{\gamma^2 - 1} + \frac{1}{2}\right] + \frac{\bar{\zeta}_f}{4}(z - z^{-1})^2[2d\sqrt{\gamma^2 - 1} + 1]d\gamma - (z - z^{-1})[d^2 + d\sqrt{\gamma^2 - 1} + 1]\gamma - \bar{\zeta}_f(z + z^{-1} - 2)[d\sqrt{\gamma^2 - 1} + \gamma^2]d\right\}, \quad (6)$$

where

$$z_1 = \gamma + \sqrt{\gamma^2 - 1} - 2d, \quad z_2 = \gamma - \sqrt{\gamma^2 - 1} + 2d;$$

$$\gamma_0 = \sqrt{1 + d^2},$$

$$\gamma_1 = \frac{1}{2}\{(1 + 2d) + (1 + 2d)^{-1}\}, \quad (7)$$

$$\gamma_2 = \frac{1}{2}\{(1 - 2d) + (1 - 2d)^{-1}\}, \quad d < \frac{1}{2},$$

$$\gamma_2 = \infty, \quad d \geq \frac{1}{2}.$$

Hence, the radiative-transition probability summed over the final-neutrino polarizations is

$$W_{\bar{\zeta}_f = 1} + W_{\bar{\zeta}_f = -1} = \frac{\mu_0^2 m_\nu^3}{2}(1 - \bar{\zeta}_f) \times \{Z(z_1, 1) + Z(z_2, -1)\}\Theta(\gamma - \gamma_0). \quad (8)$$

If the condition $d\gamma \ll 1$ holds, expression (5) transforms into the formula

$$W_{\bar{\zeta}_f} = \frac{16\mu_0^2 m_\nu^3 d^3}{3\gamma}(\gamma^2 - 1)^{3/2}(1 - \bar{\zeta}_i)(1 + \bar{\zeta}_f). \quad (9)$$

This formula was derived in the quasi-classical approximation in [2]. In the ultrarelativistic case ($\gamma \gg 1$, $d\gamma \gg 1$), we have

$$W_{\bar{\zeta}_f} = \mu_0^2 m_\nu^3 d^2\gamma(1 - \bar{\zeta}_i)(1 + \bar{\zeta}_f). \quad (10)$$

We now consider the radiation power. To this end, we introduce the function

$$\tilde{Z}(z, \bar{\zeta}_f) = \gamma Z(z, \bar{\zeta}_f) - Y(z, \bar{\zeta}_f), \quad (11)$$

where

$$Y(z, \bar{\zeta}_f) = \frac{1}{\gamma(\gamma^2 - 1)}\left\{-\ln z[d^2 + d\sqrt{\gamma^2 - 1} + 1]\gamma - \frac{1}{4}(z^2 - z^{-2})[d^2 + d\sqrt{\gamma^2 - 1} + 1]\gamma + \frac{1}{12}(z - z^{-1})^3\left[d^2(2\gamma^2 - 1) + d\sqrt{\gamma^2 - 1} + \frac{1}{2}\right] + \frac{1}{2}(z - z^{-1})[2d^2\gamma^2 + 2d\sqrt{\gamma^2 - 1} + \gamma^2 + 1]\right. \quad (12)$$

$$+\frac{\bar{\zeta}_f}{12}((z+z^{-1})^3-8)[2d\sqrt{\gamma^2-1}+1]d\gamma$$

$$-\frac{\bar{\zeta}_f}{12}(z-z^{-1})^2[d\sqrt{\gamma^2-1}+\gamma^2]d\Big\}.$$

Formulas for the total radiation power are obtained from (5) and (8) provided that the replacement $Z(z, \bar{\zeta}_f) \longrightarrow \tilde{Z}(z, \bar{\zeta}_f)$ is performed in them. In the case when the relation $d\gamma \ll 1$ is valid, the radiation power is determined by the formula

$$I_{\bar{\zeta}_f} = \frac{32\mu_0^2 m_\nu^4 d^4}{3}(\gamma^2-1)^2(1-\bar{\zeta}_i)(1+\bar{\zeta}_f), \qquad (13)$$

which is obtained in the quasi-classical approximation (see [1]). In the ultrarelativistic case, the radiation power is

$$I_{\bar{\zeta}_f} = \frac{1}{3}\mu_0^2 m_\nu^4 d^2\gamma^2(1-\bar{\zeta}_i)(1+\bar{\zeta}_f). \qquad (14)$$

As follows from (10) and (14), in the ultrarelativistic case, the average energy of emitted photons is $\langle\varepsilon_\gamma\rangle = \frac{\varepsilon_\nu}{3}$. It should be noted that the formulas obtained are valid not only for neutrinos, but also for antineutrinos. The operation of charge conjugation results in the variation of the effective-potential sign and in the replacement of the left projector for the right one in Eq. (1). In this case, the sign ahead of the term containing γ^5 remains invariable.

The results obtained allow us to make the following conclusions. Neutrinos (antineutrinos) can emit photons in the case of coherent interaction with a medium only when the sign of their helicity is opposite to that of the effective potential. Otherwise, radiative transitions are absent. At low energies of an initial neutrino, only emission without the particle's spin flip is possible, the process probability being extremely low. At high energies, transitions including spin flip mainly contribute to the emission, and transitions without spin flip are absent or their probability is strongly suppressed. This results in the complete self-polarization effect: initial active left neutrinos (right antineutrinos) transform into virtually sterile right neutrinos (left antineutrinos). The situation is opposite for sterile particles: they can transform into the active form in media transparent for active neutrinos.

Using results of the first-order calculations for effective potential (2), we arrive at the following conclusions. If the medium consists only of electrons, then we have in the ultrarelativistic case,

$$W_{\bar{\zeta}_f} = \frac{\alpha\varepsilon_\nu}{32\hbar}\left(\frac{\mu_0}{\mu_B}\right)^2\left(\frac{\tilde{G}_F n_e}{m_e c^2}\right)^2(1-\bar{\zeta}_i)(1+\bar{\zeta}_f) \qquad (15)$$

for the transition probabilities of an electron neutrino (here, the Gaussian units are employed) and

$$I_{\bar{\zeta}_f} = \frac{\alpha\varepsilon_\nu^2}{96\hbar}\left(\frac{\mu_0}{\mu_B}\right)^2\left(\frac{\tilde{G}_F n_e}{m_e c^2}\right)^2(1-\bar{\zeta}_i)(1+\bar{\zeta}_f) \qquad (16)$$

for the total radiation power. Here, ε_ν is the neutrino energy; μ_B is the Bohr magneton; α is the fine-structure constant; m_e is the electron mass; and $\tilde{G}_F = G_F(1 + 4\sin^2\theta_W)$, where G_F and θ_W are the Fermi constant and the Weinberg angle, respectively. Thus, after the radiative transition, two thirds of the energy of initial active neutrinos is carried away by sterile finite neutrinos. At the same time, muon neutrinos do not emit in an electron medium. Muon neutrinos also do not emit in an electrically neutral medium in which the proton density and the electron density are equal. However, electron neutrinos can emit in this medium, provided that the electron density exceeds the neutron density. An example of such a medium is the Sun. The neutron medium is transparent for all active neutrinos but active antineutrinos can emit in a neutron medium, the corresponding formulas being obtained from expressions (15) and (16) by the replacements $\tilde{G}_F \longrightarrow G_F$ and $n_e \longrightarrow n_n$. Hence, spin light can change the relative number of active neutrinos of different types.

Naturally, the opposite of these conclusions is true when the medium consists of antiparticles. Therefore, the spin light of neutrinos constitutes a specific tool for the determination of types of astrophysical objects, as the radiative transitions of neutrinos in a dense medium can result in the emission of very high-energy photons. The effect under consideration may prove to be important for purposes of understanding the mechanism of dark-matter formation at early stages in the evolution of the Universe.

ACKNOWLEDGMENTS

The author is grateful to V.G. Bagrov, A.V. Borisov, and V.Ch. Zhukovskiĭ for fruitful discussions.

This work was supported in part by the Program of the President of Russian Federation for Support of Young Russian Scientists and Leading Scientific Schools, project no. NSh-2027.2003.2.

REFERENCES

1. A. Lobanov and A. Studenikin, Phys. Lett. B **564**, 27 (2003).
2. A. Lobanov and A. Studenikin, Phys. Lett. B **601**, 171 (2004).
3. V. A. Bordovitsyn, I. M. Ternov, and V. G. Bagrov, Usp. Fiz. Nauk **165**, 1083 (1995) [Phys. Usp. **38**, 1037 (1995)].
4. A. E. Lobanov and O. S. Pavlova, Phys. Lett. A **275**, 1 (2000).
5. A. E. Lobanov, hep-ph/0311021.
6. V. Bargmann, L. Michel, and V. Telegdi, Phys. Rev. Lett. **2**, 435 (1959).
7. A. Lobanov and A. Studenikin, Phys. Lett. B **515**, 94 (2001).
8. A. E. Lobanov and O. S. Pavlova, Vestn. Mosk. Univ., Ser. 3: Fiz., Astron. **40** (4), 3 (1999).
9. L. Wolfenstein, Phys. Rev. D: Part. Fields **17**, 2369 (1978).
10. S. P. Mikheev and A. Yu. Smirnov, Yad. Fiz. **42**, 1441 (1985) [Sov. J. Nucl. Phys. **42**, 913 (1985)].
11. L. L. Foldy, Phys. Rev. **87**, 688 (1952).
12. P. B. Pal and T. N. Pham, Phys. Rev. D: Part. Fields **40**, 259 (1989).
13. J. F. Nieves, Phys. Rev. D: Part. Fields **40**, 866 (1989).
14. D. Notzold and G. Raffelt, Nucl. Phys. B **307**, 924 (1988).

Translated by G. Merzon

Doklady Physics, Vol. 50, No. 6, 2005, pp. 290–294. Translated from Doklady Akademii Nauk, Vol. 402, No. 4, 2005, pp. 479–483.

PHYSICS

Magnetic Component of Thermodynamic Functions for Polymorphic Modifications of Iron

N. N. Sirota and N. A. Konoplin

Presented by Academician O.A. Bannykh December 8, 2004

Received December 8, 2004

At normal pressure, iron has three polymorphic modifications that exist in the equilibrium state within different temperature ranges. Below 1189 K, α modification with body-centered cubic (bcc) structure (A2) is stable, whereas within the range from 1189 to 1165 K, γ modification with the face-centered cubic structure (A1) is stable. At higher temperatures ranging from 1165 K to the melting point of iron (1808 K), there exists δ modification with the bcc structure (A2) [1]. Structurally, the α and δ modifications are isomorphic but differ in their magnetic properties. At temperatures below 1043 K (Curie point), the α modification is ferromagnetic. Magnetization M_S of the α modification progressively decreases with increasing temperature. On the contrary, the derivative $\frac{\partial M_S}{\partial T}$ increases with temperature and attains the maximum at the Curie point, which is typical of second-order phase transitions. Unlike the α modification, the δ modification is paramagnetic. Its free energy and other thermodynamic properties differ greatly from those of the α modification in terms of their magnetic components.

At the absolute zero temperature, the difference in enthalpy for the α and δ modifications $(H_\alpha - H_\delta)_0 = \Delta U_{\alpha-\delta,0}$ is specified by the value of the spontaneous-magnetization energy of the α modification.

According to the calorimetric data of [2], the experimental value of the magnetic component for enthalpy is the following:

$$\Delta H_{0\text{mag}} = \int_0^\infty C_{\text{mag}} dT = (8060 \pm 484)\ \text{J/mol}.$$

The magnetic component $\Delta H_{0\text{mag}}$ in the enthalpy difference for the α and δ modifications (as $T \longrightarrow 0$) corresponds, in fact, to the (α–δ) phase transition energy as $T \longrightarrow 0$. In the approximation of the molecular-field theory, this quantity is directly proportional to the saturation spontaneous magnetization M_S squared for a mole of iron at $T = 0$ K:

$$\Delta H_{0\text{mag}} = U_{\text{mag}} = kM_{S0}^2, \quad (1)$$

where k is the proportionality coefficient.

In a certain sense, we may consider that the other thermodynamic components of the free energies for the α and δ modifications (with the exception of the magnetic components caused by ferromagnetic long-range ordering) are virtually identical.

Table 1 presents experimental values of molar heat capacity C_p at a constant pressure, enthalpy ΔH_T, and entropy S_T for the α modification [3]. The calculated values of C_p, ΔH_T, and entropy S_T for the δ modification (for which the lattice components are foundational), as well as the calculated differences in the corresponding thermodynamic functions for the α and δ modifications, are also indicated. The thermodynamic functions for the δ modification were found with the use of the Debye functions at the characteristic Debye temperature $\Theta_D = 420$ K [4, 5]. We took into account the electron component that was determined for the heat capacity by the formula $C_{\text{el}} = aT + bT^3$, where the coefficients a and b are equal to 4.942×10^{-3} J/(mol K^2) [4, 6] and 0.19×10^{-9} J/(mol K^4), respectively [7]. The values of heat capacity C_p were calculated from the known Grüneisen relation $C_p = C_V(1 + \gamma\alpha_V T)$, where C_V is the heat capacity at a constant volume and $\gamma = \frac{\alpha_V V}{C_V \chi}$ is the Grüneisen coefficient. To calculate the Grüneisen coefficient, we used the temperature dependences for the coefficient of volumetric expansion $\alpha_V(T)$ and for molar volume $V(T)$, the latter having been taken from [8, 9].

Moscow State University of Nature Design, ul. Pryanishnikova 19, Moscow, 127550 Russia
e-mail: n.sirota@ru.net

1028-3358/05/5006-0290$26.00

The values for the iron compressibility factor $\chi(T)$ [10] were extrapolated to the high-temperature range. The anharmonic component in the thermodynamic functions was ignored.

Figure 1 shows the calculated temperature dependences (for the δ modification) of the heat capacities C_p and C_V ($C_V = C_{Deb} + C_{el}$), as well as their lattice C_{Deb} and electron C_{el} components.

Within the temperature range in which the δ modification exists in the equilibrium state, the character of the temperature dependences of its thermodynamic functions is in good agreement with the experimental data of [3, 6].

The difference found in the thermodynamic functions for the α and δ modifications within the temperature range lower than the temperature of the α–γ transition (1189 K [1], 1184 K [3]) can be considered to be consistent with the magnetic component of the thermodynamic functions for the α modification. The calculated values of the magnetic components are close to those obtained in [4, 7, 11].

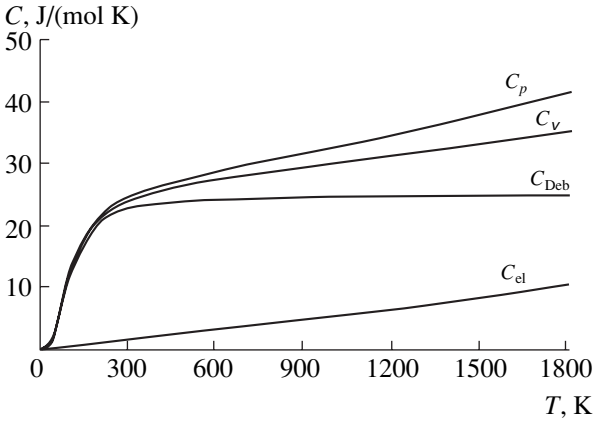

Fig. 1. Temperature dependences of heat capacities C_p and C_V and their components for the δ modification of iron.

Table 1. Thermodynamic functions of the α [3] and δ modifications of iron and their difference

T, K	α modification			δ modification			α – δ		
	C_p, J/(mol K)	$H - H_0$, J/mol	S, J/(mol K)	C_p, J/(mol K)	$H - H_0$, J/mol	S, J/(mol K)	C_p, J/(mol K)	$H - H_0$, J/mol	S, J/(mol K)
0	0	0	0	0	0	0	0	–	–
100	12.05	421	5.98	12.03	441	6.40	0.02	–	–
200	21.42	2184	17.82	21.35	2187	18.35	0.07	–	–
300	25.02	4531	27.28	24.59	4529	27.66	0.43	–	–
400	27.41	7151	34.80	26.25	7078	34.71	1.16	−7988	0.09
500	29.58	10004	41.17	27.57	9770	41.00	2.01	−7826	0.17
600	31.67	13067	46.74	28.71	12579	46.23	2.96	−7572	0.51
700	34.35	16359	51.80	29.67	15499	50.68	4.68	−7200	1.12
800	38.07	19970	56.61	30.66	18515	54.75	7.41	−6605	1.86
900	43.51	24025	61.42	31.59	21710	58.44	11.92	−5746	2.98
1000	55.52	28865	66.53	32.56	24843	61.95	22.96	−4037	4.57
1042	89.96	31585	69.56	32.93	26423	63.66	57.03	−2898	5.51
1100	44.52	34472	71.87	33.45	28161	65.08	11.07	−1749	6.79
1184	38.99	37945	74.80	34.37	31000	67.55	4.62	−1116	7.25
1200	38.53	38564	75.43	34.51	31561	68.14	4.02	−1057	7.30
1300	38.91	42426	78.53	35.40	35084	70.91	3.51	−719	7.62
1400	39.58	46355	81.44	36.40	38703	73.66	3.18	−408	7.78
1500	40.21	50342	84.19	37.53	42448	76.34	2.68	−166	7.85
1600	40.84	54392	86.80	38.65	46384	78.94	2.19	−52	7.87
1665	41.25	57061	88.06	39.52	49028	80.55	1.73	−26	7.88
1700	41.46	58509	89.30	39.86	50457	81.41	1.60	−8	7.89
1800	42.13	62689	91.69	41.08	54629	83.77	1.05	−1	7.92

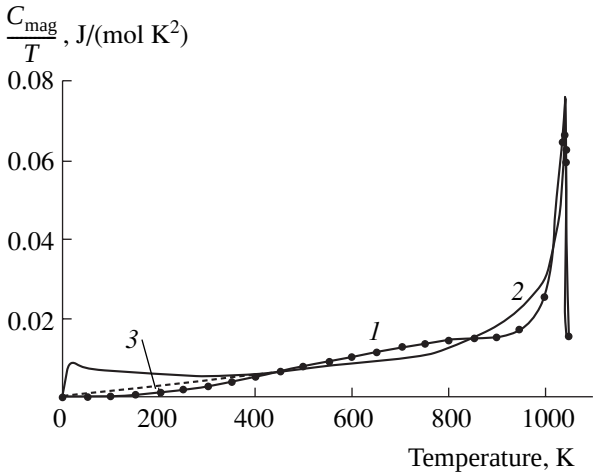

Fig. 2. Dependence $\frac{C_{mag}}{T}(T)$: (*1*) calculations by formula (6); (*2*) calculations by formula (2) on the basis of experimental values of M_S; and (*3*) extrapolation of the low-temperature branch of curve *2*.

In accordance with (1), the magnetic components of the heat capacity C_{mag}, internal energy ΔU_{mag}, enthalpy ΔH_{mag}, and entropy S_{mag} are as follows:

$$C_{mag} = k\frac{\partial M_S^2}{\partial T}, \tag{2}$$

$$\Delta H_{mag} = \Delta U_{mag} = \int_0^T C_{mag}dT = k\int_0^T \frac{\partial M_S^2}{\partial T}dT, \tag{3}$$

$$S_{mag} = \int_0^T \frac{C_{mag}}{T}dT = k\int_0^T \frac{\partial M_S^2}{\partial T}\frac{\partial T}{T}. \tag{4}$$

Table 2 presents the experimental values of magnetization M_S [12, 13] and the calculated values for the magnetic components of the thermodynamic functions for the α modification. These data were calculated on the basis of experimental values of the magnetization and formulas (2)–(4). The coefficient k was assumed to be constant and was taken to be equal to 2.58×10^9 J m^2/(mol A^2) according to formula (1), where $H_{0mag} = 8060$ J/mol and $M_{S0} = 1.766 \times 10^6$ A/m.

Using the expression for the temperature dependence of the saturation magnetization

$$M_S = M_{S0}e^{-\frac{1}{2}\chi(T)} \tag{5}$$

taken from [14], where

$$\chi(T) = \mu\left(\frac{T}{T_C}\right)^4 + c\tan^2\left(\frac{\pi}{2}\alpha\frac{T}{T_C}\right),$$

$\mu = 1.2$, $c = 0.002$, and $\alpha = 0.98$, we can calculate the magnetic components of the thermodynamic functions ΔH_{mag}, S_{mag}, and of the heat capacity:

$$C_{mag} = k\frac{\partial M_S^2}{\partial T} = kM_{S0}^2\frac{\partial \chi(T)}{\partial T}e^{-\chi(T)}. \tag{6}$$

The values obtained are presented in Table 2.

Table 2. Temperature dependence of the magnetic components ΔH_{mag} and S_{mag} of enthalpy and entropy, respectively, for the α modification of iron according to calculations based on experimental [12, 13] and theoretical [formula (5)] values of the saturation magnetization M_S

T, K	Experiment				Calculation according to (5)		
	M_S, 10^6 A/m	ΔH_{mag}, J/mol	S_{mag}, J/(mol K)	S_{mag}, J/(mol K) (extrapolation)	M_S, 10^6 A/m	ΔH_{mag}, J/mol	S_{mag}, J/(mol K)
0	1.766	−8060	0	0	1.766	−8060	0
100	1.766	−8019	0.69	0.08	1.762	−8059	0.01
200	1.764	−7917	1.39	0.29	1.750	−8045	0.10
300	1.758	−7754	2.01	0.65	1.732	−7991	0.32
400	1.743	−7549	2.65	1.17	1.709	−7846	0.72
500	1.709	−7219	3.37	1.79	1.671	−7553	1.37
600	1.651	−6757	4.21	2.60	1.617	−7046	2.29
700	1.559	−6156	5.14	3.53	1.543	−6283	3.46
800	1.426	−5326	6.24	4.65	1.436	−5258	4.83
900	1.246	−4076	7.74	6.16	1.255	−4011	6.29
1000	0.952	−1904	9.99	8.43	0.859	−2345	8.04
1043	0.352	−79	11.82	10.26	0.173	−320	9.91

The magnetic component S_{mag} of the entropy was found graphically from the dependences $(\frac{C_{mag}}{T}(T))$ shown in Fig. 2. Table 2 also contains the values of S_{mag} that were obtained by the linear extrapolation of the low-temperature branch of the curve $\frac{C_{mag}}{T}(T)$, which was calculated from the experimental values of the saturation magnetization M_S.

The magnetic components of the thermodynamic functions, which are caused by the ferromagnetic (long-range) ordering of spins, were found from the experimental values given in [12, 13] and those calculated by formula (5) for the saturation magnetization M_S. The results obtained are close to each other. At low temperatures, they approach the calculated difference in the thermodynamic functions for the α and δ isomorphic modifications. With increasing temperature, the difference between them increases due to the enhanced role of the short-range spin ordering, which was ignored in our calculations.

The values of $\frac{M_S}{M_{S0}}$ for the α modification, which were calculated by formula (5) and found experimentally, are presented in Fig. 3. We note the good agreement between the experimental and calculated data. The curves shown in Fig. 4 correspond to dependences $C_{mag}(T)$ calculated by formula (6) (curve *1*), by formula (2) using the experimental values of M_S [12, 13] (curve *2*), and using the difference in heat capacities of the α and δ modifications of iron (curve *3*).

As a result of introducing the correlation function, the existing tails [13] caused by different factors, including the presence of the short-range spin ordering, are cut off. The maximum of the temperature dependence of the heat-capacity magnetic component C_{mag} calculated by formula (6) corresponds to the experimental value of the Curie point.

As was shown in [14], the critical temperature T_C can be found by the formula

$$T_C = \left(\frac{U_0\Theta_D^3}{\gamma}\right)^{1/4},$$

where γ is a constant (γ = 0.47), Θ_D = 410 K, and U_0 = 8060 J/mol is the energy of the spontaneous magnetization as $T \longrightarrow 0$. Therefore, $T_C \approx 1043$ K. The Curie temperature thus obtained coincides with its experimental value.

Thus, the magnetic components of thermodynamic functions for the α modification of iron that were calculated in this study determine a significant part of these functions. The method used of the quantitative description of the magnetic components enables one to discover their temperature-dependent values at an acceptable level of accuracy.

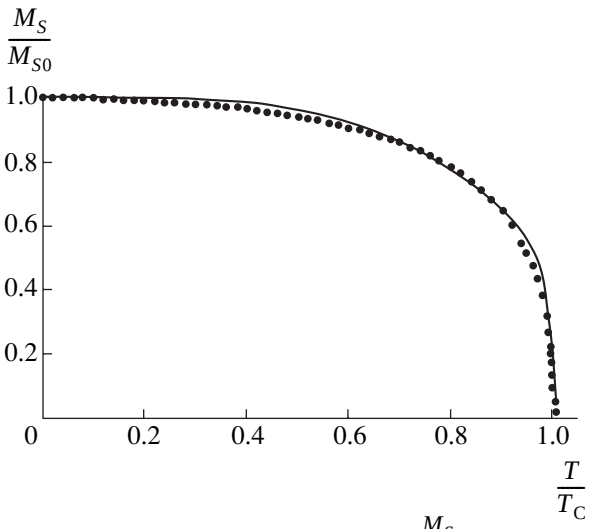

Fig. 3. Relative saturation magnetization $\frac{M_S}{M_{S0}}$ of iron as a function of temperature: solid curve corresponds to data calculated by formula (5) (μ = 1.2, c = 0.002, and α = 0.98) and dotted curve corresponds to the experimental data of [12, 13].

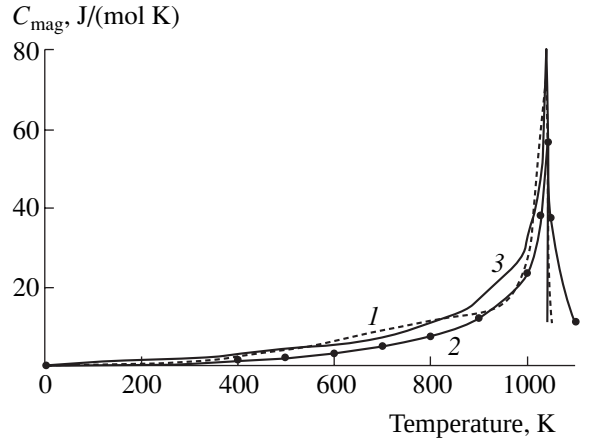

Fig. 4. Temperature dependence of the magnetic component of the heat capacity for the α modification: (*1*) calculation by formula (6) (μ = 1.2, c = 0.002, and α = 0.98); (*2*) calculation based on the experimental data for the saturation magnetization M_S [12, 13]; and (*3*) results obtained from the difference of the heat capacities $C_{p\alpha}$ and $C_{p\delta}$.

REFERENCES

1. R. Haltgren, P. D. Desai, D. T. Hawkins, *et al.*, *Selected Values of the Thermodynamic Properties of the Elements* (Amer. Soc. Metals, New York, 1973).
2. R. J. Weiss and K. J. Tauer, J. Phys. Chem. Solids **2**, 237 (1957).
3. B. M. Mogutnov, I. A. Tomilin, and L. A. Shvartsman, *Thermodynamics of Iron–Carbon Alloys* (Metallurgiya, Moscow, 1972) [in Russian].

4. R. J. Weiss and K. J. Tauer, Phys. Rev. **102**, 1490 (1956).
5. L. S. Darken and R. P. Smith, J. Industr. Eng. Chem. **43**, 1815 (1951).
6. P. D. Desai, J. Phys. Chem. Ref. Data **15**, 967 (1986).
7. R. Kohlhaas and M. Braun, Phys. Stat. Sol. **12**, 429 (1965).
8. Z. S. Basinski, W. Hume-Rothery, and A. L. Sutton, Proc. Roy. Soc. **229**, 459 (1955).
9. S. I. Novikova, *Thermal Expansion of Solids* (Nauka, Moscow, 1974) [in Russian].
10. *Elastic Constants and Elasticity Moduli of Metals and Non-Metals*, *Handbook*, Ed. by I. N. Frantsevich, F. F. Voronov, and S. A. Bakuta (Naukova Dumka, Kiev, 1974) [in Russian].
11. J. A. Hofman, A. Paskin, K. J. Tauer, *et al.*, J. Phys. Chem. Solids **1**, 45 (1956).
12. Landolt-Börnstein, in *Magnetic Properties of Metals*, New Series, Ed. by H. P. J. Wijn (Springer, Berlin, 1994), Vol. 3/19il, p. 238.
13. B. Averbakh, in *Magnetic Properties of Metals and Alloys* (Inostrannaya Literatura, Moscow, 1961; Seminar on Magnetic Properties of Metals and Alloys, Cleveland, October 25–26, 1958).
14. N. N. Sirota, Dokl. Akad. Nauk **402**, 329 (2005) [Dokl. Phys. **50**, 242 (2005)].

Translated by Yu. Vishnyakov

Doklady Physics, Vol. 50, No. 6, 2005, pp. 295–298. Translated from Doklady Akademii Nauk, Vol. 402, No. 4, 2005, pp. 484–487.

PHYSICS

Effect of the Evaporation Coefficient on the Unsteady Process of Aerosol-Droplet Size Variation

Yu. I. Yalamov and M. K. Kuz'min

Presented by Academician R.F. Ganiev November 16, 2004

Received November 17, 2004

At present, the development of a general theory that describes the unsteady processes involved in the evaporation and condensation growth of aerosol droplets remains a rather urgent physical problem. A particularly significant component of this problem is the physically correct formulation of boundary conditions at the droplet–environment interface. In this case, it is extremely important to give adequate account to the evaporation (condensation) coefficient of the droplet substance [1].

In the present paper, we propose to take into direct account the evaporation coefficient while analyzing the unsteady processes of the evaporation and condensation growth of an immobile spherical droplet. Using the Laplace integral transformations, we have managed to obtain general expressions for the distributions of both the vapor concentration and temperature field in the medium surrounding the droplet, as well as for the concentration of saturated vapors on the droplet surface as a function of time. Expressions for the droplet-radius variation rate are found. The results of the present paper are compared with those previously obtained by the authors for a case in which the evaporation coefficient was taken into account implicitly (i.e., in terms of gas-kinetic coefficients for jumps of the concentration and temperature) [2]. In addition, we have studied here the problem associated with the effect of temperature variation inside the aerosol droplet on the rate of the unsteady process of droplet evaporation and condensation growth.

The distribution of the (relative) vapor concentration c_1 and the temperature T of the vapor–gas mixture satisfy the set of equations

$$\frac{\partial c_1}{\partial t} = D\left(\frac{\partial^2 c_1}{\partial r^2} + \frac{2}{r}\frac{\partial c_1}{\partial r}\right), \quad (1)$$

$$\frac{\partial T}{\partial t} = a\left(\frac{\partial^2 T}{\partial r^2} + \frac{2}{r}\frac{\partial T}{\partial r}\right) \quad (2)$$

with the boundary conditions

$$c_1(r,t)\big|_{t=0} = c_{10}, \quad c_1(r,t)\big|_{r\to+\infty} = c_{1\infty} = c_{10}, \quad (3)$$

$$T(r,t)\big|_{t=0} = T_0, \quad T(r,t)\big|_{r\to+\infty} = T_\infty = T_0, \quad (4)$$

$$Lm_1 nD\frac{\partial c_1}{\partial r}\bigg|_{r=R} = -\kappa\frac{\partial T}{\partial r}\bigg|_{r=R}, \quad (5)$$

$$c_{1s}(t) = c_{1s0}\{1 + \nu_{s0}[T_s(t) - T_0]\}, \quad (6)$$

$$-D\frac{\partial c_1}{\partial r}\bigg|_{r=R} = \alpha\nu(c_{1s} - c_1)\big|_{r=R}. \quad (7)$$

Here, r is the radial coordinate of a spherical coordinate system with the origin at the droplet center, and t is time. The quantities entering into Eqs. (1) and (2) are the following: $D = \frac{nm_2D_{12}}{\rho}$, where D_{12} is the coefficient of mutual diffusion for the components of the binary mixture whose first and second components are formed by droplet-substance molecules and carrier-gas molecules, respectively. Furthermore, $n = n_1 + n_2$; n_1 and m_1 and n_2 and m_2 are the concentrations and masses of molecules belonging to the first and second components, respectively; ρ is the density of the vapor–gas mixture, and a is the thermal diffusivity of a binary mixture. The following quantities enter into boundary condition (5): L is the specific heat of the phase transition for the droplet substance and κ is the thermal conductivity of the vapor–gas mixture. Condition (6) is the linear approximation of the Clapeyron–Clausius equation and contains the terms $c_{1s}(t) = c_1(T_s) = \frac{n_1(T_s)}{n}$, where $n_1(T_s)$ is the concentration of saturated vapors of the droplet substance at the surface temperature $T_s =$

Moscow State Regional University,
ul. Radio 10A, Moscow, 105005 Russia
e-mail: rectorat@mgou.ru

1028-3358/05/5006-0295$26.00

$T_s(t) = T(r, t)|_{r=R}$; $c_{1s0} = c_{1s}(t)|_{t=0}$; and $\nu_{s0} = \dfrac{Lm_1 - kT_0}{kT_0^2}$,

where k is the Boltzmann constant. In accordance with the reference data of [3], we suppose that $\nu_{s0} > 0$.

Boundary condition (7) makes it possible to immediately take into account the effect of the evaporation coefficient α in the process under consideration. Here, the quantity $\nu = \sqrt{\dfrac{kT_0}{2\pi m_1}}$ represents a quarter of the average absolute thermal velocity of vapor molecules. It is worth noting that the validity of relationships (7) follows from simple statistical considerations [4].

In order to solve the problem, we introduce the notation

$$S(r, p) = \int_0^\infty c_1(r, t)\exp(-pt)dt,$$

$$\theta(r, p) = \int_0^\infty T(r, t)\exp(-pt)dt, \qquad (8)$$

$$S_s(p) = \int_0^\infty c_{1s}(t)\exp(-pt)dt$$

and make use of the Laplace integral transformations [5].

Employing initial conditions (3) and (4), we find the corresponding images of Eqs. (1) and (2):

$$DS'' + \frac{2D}{r}S' - pS + c_{10} = 0,$$
$$a\theta'' + \frac{2a}{r}\theta' - p\theta + T_0 = 0. \qquad (9)$$

They are ordinary differential equations expressed in terms of unknown functions $S(r, p)$, $\theta(r, p)$, where r is the independent variable and p plays the role of a parameter. Solutions to Eqs. (9) in the image space must satisfy certain relationships that correspond to boundary conditions (3)–(7). Taking into account all of these relationships, we find in the image space

$$S(r, p) = \frac{c_{10}}{p} - \frac{\varepsilon_\alpha \kappa R}{r}\frac{p_2}{p\delta}\exp(-\alpha_c\sqrt{p}), \qquad (10)$$

$$\theta(r, p) = \frac{T_0}{p} - \frac{\varepsilon_\alpha l R}{r}\frac{p_1}{p\delta}\exp(-\alpha_T\sqrt{p}), \qquad (11)$$

$$S_s = \frac{c_{1s0}}{p} + \frac{\varepsilon_\alpha \kappa_D p_1}{p\delta}. \qquad (12)$$

Here,

$$\varepsilon_\alpha = \alpha\nu(c_{10} - c_{1s0}), \quad l = Lm_1 nD, \quad \kappa_D = c_{1s0}\nu_{s0}l,$$
$$\alpha_c = \frac{r-R}{\sqrt{D}}, \quad \alpha_T = \frac{r-R}{\sqrt{a}};$$
$$p_1 = \sqrt{\frac{p}{D}} + \frac{1}{R}, \quad p_2 = \sqrt{\frac{p}{a}} + \frac{1}{R},$$
$$\delta = g_0 p + g_1\sqrt{p} + g_2, \quad g_0 = \kappa\sqrt{\frac{D}{a}},$$
$$g_1 = \frac{1}{R\sqrt{Da}}[D\kappa(\sqrt{D} + \sqrt{a}) + \alpha\nu R(\kappa_D\sqrt{a} + \kappa\sqrt{D})],$$
$$g_2 = \frac{1}{R^2}[D\kappa + \alpha\nu R(\kappa_D + \kappa)].$$

We note that the expansion $\delta = g_0(\sqrt{p} + \beta_1)(\sqrt{p} + \beta_2)$ is valid, where β_1, β_2 are positive quantities that are not equal to each other.

We use the following denotations for functions in the original space:

$$\Phi(\alpha, \beta, t) = \operatorname{erfc}\left(\frac{\alpha}{2\sqrt{t}}\right)$$
$$- \exp(\beta^2 t + \alpha\beta)\operatorname{erfc}\left(\frac{\alpha}{2\sqrt{t}} + \beta\sqrt{t}\right),$$
$$\varphi(\beta, t) = \exp(\beta^2 t)\operatorname{erfc}(\beta\sqrt{t}).$$

Passing to the space of originals, we find in accordance with expressions (10)–(12) and by virtue of notation (8) that the vapor-concentration distribution, the temperature field in the medium surrounding the droplet, and also the dependence of the saturated-vapor concentration at the droplet surface as functions of time are the following:

$$c_1(r, t) = c_{10} - \frac{\varepsilon_\alpha \kappa}{r\sqrt{a}}\sum_{j=1}^{2} A(\beta_j)\Phi(\alpha_c, \beta_j, t), \qquad (13)$$

$$T(r, t) = T_0 - \frac{\varepsilon_\alpha l}{r\sqrt{D}}\sum_{j=1}^{2} B(\beta_j)\Phi(\alpha_c, \beta_j, t), \qquad (14)$$

$$c_{1s}(t) = c_{1s0} + \frac{\varepsilon_\alpha \kappa_D}{R\sqrt{D}}\left[\frac{\sqrt{D}}{g_2} - \sum_{j=1}^{2} B(\beta_j)\varphi(\beta_j, t)\right], \qquad (15)$$

where

$$A(\beta_j) = \frac{R\beta_j - \sqrt{a}}{g_0\beta_j^2 - g_2}, \quad B(\beta_j) = \frac{R\beta_j - \sqrt{D}}{g_0\beta_j^2 - g_2}.$$

As is well known from [6], the rate of the unsteady variation of the droplet radius is determined by the

formula

$$\frac{dR}{dt} = \frac{Dnm_1}{\gamma}\frac{\partial c_1}{\partial r}\bigg|_{r=R}, \quad (16)$$

where γ is the density of the droplet substance, and the value of the quantity can be found from Eq. (13). Thus, we arrive at

$$\frac{dR}{dt} = \frac{\varepsilon_\alpha n m_1 D\kappa}{\gamma R^2}\left[\frac{1}{g_2} + \frac{1}{\sqrt{Da}}\sum_{j=1}^{2} C(\beta_j) j(\beta_j, t)\right], \quad (17)$$

where

$$C(\beta_j) = \frac{R^2\beta_j^2 - R(\sqrt{D}+\sqrt{a})\beta_j + \sqrt{Da}}{g_0\beta_j^2 - g_2}.$$

It should be noted that the value $\frac{\partial c_1}{\partial r}\Big|_{r=R}$ can be immediately found as an original of the image $\frac{\partial S}{\partial r}\Big|_{r=R}$. As follows from relation (10), the expression for this original is of the form

$$\frac{\partial S}{\partial r}\bigg|_{r=R} = \frac{\varepsilon_\alpha \kappa p_1 p_2}{p\delta}$$

$$= \frac{\alpha\nu(c_{10}-c_{1s0})\kappa p_1 p_2}{p[D\kappa p_1 p_2 + \alpha\nu(\kappa_D p_1 + \kappa p_2)]}. \quad (18)$$

Relationships (17) and (18) are obtained without allowance for the temperature variation inside the droplet. We now clarify the question associated with the effect of the temperature variation inside the droplet on the rate of the unsteady variation of its radius. The temperature $T_i = T_i(r, t)$, $(0 \le r \le R)$ of a spherical droplet obeys the thermal-conduction equation

$$\frac{\partial T_i}{\partial t} = a_i\left(\frac{\partial^2 T_i}{\partial r^2} + \frac{2}{r}\frac{\partial T_i}{\partial r}\right) \quad (19)$$

and boundary conditions

$$T_i(r, t)\big|_{t=0} = T_0, \quad T_i(r, t)\big|_{r=R} = T(r, t)\big|_{r=R}, \quad (20)$$

$$l\frac{\partial c_1}{\partial r}\bigg|_{r=R} = \left(-\kappa\frac{\partial T}{\partial r} + \kappa_i\frac{\partial T_i}{\partial r}\right)\bigg|_{r=R}, \quad (21)$$

where a_i, κ_i are the thermal diffusivity and conductivity of the droplet substance. Thus, in order to take into account the temperature variation inside an aerosol droplet in the process we considered, one should investigate the set of Eqs. (1), (2), (19) assuming the validity of initial and boundary conditions (3), (4), (6), (7), (20), and (21) [boundary condition (5) is replaced by (21)].

As before, we apply the Laplace integral transformations [5] with due regard to the fact that the temperature $T_i(r, t)$ at the droplet center ($r = 0$) cannot be infinitely high. Then, we find that in the image space

$$\left(\frac{\partial S}{\partial r}\right)_i\bigg|_{r=R}$$

$$= \frac{\alpha\nu(c_{10}-c_{1s0})p_1(\kappa p_2 + \kappa_i F_i)}{p[(Dp_1 + \alpha\nu)(\kappa p_2 + \kappa_i F) + \alpha\nu\kappa_D p_1]}, \quad (22)$$

where $F_i = F_i(p) = \sqrt{\frac{p}{a_i}}\coth R\sqrt{\frac{p}{a_i}} - \frac{1}{R}$.

Since

$$\lim_{p\to\infty} p\left(\frac{\partial S}{\partial r}\right)_i\bigg|_{r=R} = \frac{\varepsilon_\alpha}{D},$$

$$\lim_{p\to 0} p\left(\frac{\partial S}{\partial r}\right)_i\bigg|_{r=R} = \frac{\varepsilon_\alpha\kappa}{D\kappa + \alpha\nu R(\kappa_D + \kappa)},$$

and using the limiting theorem [5], we obtain in accordance with formula (16)

$$\lim_{t\to 0_+}\left(\frac{dR}{dt}\right)_i = \frac{Dnm_1}{\gamma}\frac{\varepsilon_\alpha}{D} = \frac{\varepsilon_\alpha n m_1}{\gamma},$$

$$\lim_{t\to+\infty}\left(\frac{dR}{dt}\right)_i = \frac{\varepsilon_\alpha n m_1 D\kappa}{\gamma[D\kappa + \alpha\nu R(\kappa_D + \kappa)]}.$$

Hence, it follows that the allowance for temperature variation inside the droplet affects the rate of the unsteady variation of the droplet radius neither at the initial instant of the process nor for extended times.

We now analyze the solutions obtained. Expressions (18) and (22) both tend to zero as $\alpha \longrightarrow 0$. Thus, in accordance with formula (16), the rates of the droplet-radius variation will tend to zero both with and without allowance for the temperature change inside the droplet.

We now consider the expression

$$\left(\frac{\partial S}{\partial r}\right)_\chi\bigg|_{r=R} = \frac{\varepsilon\kappa p_1 p_2}{p(\chi p_1 p_2 + \kappa_D p_1 + \kappa p_2)}, \quad (23)$$

which was derived in [2]. In this expression, the evaporation coefficient is taken into account implicitly via the coefficients of jumps of the concentration and temperature $K_c^{(c)}$, $K_c^{(T)}$, $K_T^{(T)}$, $K_T^{(c)}$ [1]. In expression (23), the notation

$$\varepsilon = c_{10} - c_{1s0} - c_{1s0}\nu_{s0}(T_0 - T_{s0})$$

is used (below, in comparing the formulas, we suppose that $T_0 - T_{s0} = 0$) and

$$\chi = \kappa K_c^{(c)} - \frac{l}{T_0}K_c^{(T)} + \kappa_D K_T^{(T)} - c_{1s0}\nu_{s0}\kappa T_0 K_T^{(c)}.$$

As is seen from relationship (23), jumps in the concentration and temperature affect the rate of the drop-

Table

T_0, K	$\frac{dR}{dt}\left(\frac{dR}{dt}\right)^{-1}_{\chi}$			
	0.5 μm	1 μm	5 μm	10 μm
293	1.21	1.11	1.02	1.01
323	1.33	1.17	1.04	1.02

let-radius variation via the function χ. Taking the expressions for the coefficients $K_c^{(c)}$, $K_c^{(T)}$, $K_T^{(T)}$, $K_T^{(c)}$ from the monograph [1], we find the quantity χ as a function of the evaporation coefficient α: $\chi = \frac{\chi_1}{\alpha} + \chi_2$, where χ_1, χ_2 are known quantities independent of α. As far as in the general case, $\chi_1 \neq 0$, we arrive at $\alpha \longrightarrow 0$ as $\left(\frac{\partial S}{\partial r}\right)_{\chi}\Big|_{r=R} \longrightarrow 0$. Hence, according to formula (16), we deal with the tendency $\left(\frac{dR}{dt}\right)_{\chi} \longrightarrow 0$.

We note that all functions (13)–(15) and (17) obtained in the space of originals linearly depend on the quantity $\varepsilon_\alpha = \alpha\nu(c_{10} - c_{1s0})$.

Further, we continue the analysis of expressions for the rate of the droplet-radius variation. Formula (17) is derived for all times from 0 to +∞. We consider the asymptotic expansion of the function $\varphi(\beta_j, t)$ for large values of t, namely,

$$\varphi(\beta_j, t) = \frac{1}{\beta_j\sqrt{\pi t}}\left[1 + \sum_{m=1}^{\infty}(-1)^m \frac{1\times 3\times\ldots\times(2m-1)}{(2\beta_j^2 t)^m}\right]. \quad (24)$$

Employing expansion (24) and in accordance with formula (17), we can obtain the expression for the droplet-radius variation rate in the form of an infinite series for large values of time. Taking the zero approximation in expansion (24), we obtain the corresponding approximation of formula (17):

$$\frac{dR}{dt} = \frac{\varepsilon_\alpha n m_1 D\kappa}{\gamma[D\kappa + \alpha\nu R(\kappa_D + \kappa)]}. \quad (25)$$

We now compare formula (25) with the analogous approximate formula

$$\left(\frac{dR}{dt}\right)_{\chi} = \frac{\varepsilon n m_1 D\kappa}{\gamma[\chi + R(\kappa_D + \kappa)]} \quad (26)$$

found in [2]. To arrive at concrete conclusions, we consider the process of unsteady evaporation ($\varepsilon_\alpha < 0$) of water droplets in dry air ($c_{10} = 0$) at a pressure $p = 10^5$ Pa. In this case, we restrict our analysis to two characteristic values 293 and 323 K of the initial temperature T_0. We assume $\alpha = 1$ and calculate the values of expressions (25) and (26) at the indicated initial temperatures for different values of R. Afterwards, we compose the table of ratios $\frac{dR}{dt}\left(\frac{dR}{dt}\right)^{-1}_{\chi}$.

From both the table and expressions (25) and (26), we can conclude that the larger an evaporating droplet, the smaller the discrepancy between the variation rates of its radius, which were calculated on the basis of various methods that took into account the evaporation coefficient.

Thus, although the method proposed in this study is very simple, it is rather important because of its practical applications; and it is capable of directly allowing for the evaporation coefficient, which is highly consistent with results obtained by us on the basis of another, more complicated method. This conclusion particularly relates to the case of the evaporation of large droplets ($R > 7$ μm).

REFERENCES

1. Yu. I. Yalamov and V. S. Galoyan, *Dynamics of Droplets in Inhomogeneous Viscous Media* (Luĭs, Yerevan, 1985) [in Russian].
2. Yu. I. Yalamov and M. K. Kuz'min, *Generalization of Theory of Unsteady Size Variation for an Aerosol Droplet with Its Evaporation and Condensation Growth* (VINITI, Moscow, 2004), No. 630 [in Russian].
3. N. B. Vargaftik, *Tables of the Thermophysical Properties of Liquids and Gases*, 2nd ed. (Nauka, Moscow, 1972; Halsted Press, New York, 1975).
4. L. D. Landau and E. M. Lifshitz, *Statistical Physics* (Fizmatlit, Moscow, 2002), Part 1 [in Russian].
5. G. Doetsch, *Ainleitung zum practischen Gebrauch der Laplace-Transformation und der Z-Transformation* (R. Oldenbourg, Munchen, 1967; Nauka, Moscow, 1971).
6. N. A. Fuks, *Evaporation and Growth of Droplets in a Gaseous Medium* (Akad. Nauk SSSR, Moscow, 1958) [in Russian].

Translated by G. Merzon

Doklady Physics, Vol. 50, No. 6, 2005, pp. 299–302. Translated from Doklady Akademii Nauk, Vol. 402, No. 5, 2005, pp. 613–616.

PHYSICS

Temperature and Pressure Effects on the Isomorphic Transition between the α and γ Phases of Cerium

N. N. Sirota and A. V. Morozov

Presented by Academician V.V. Osiko December 16, 2004

Received December 20, 2004

The equilibrium $\alpha \longleftrightarrow \gamma$ transition between the isomorphic phases of cerium for various pressures and temperatures up to the end point, i.e., critical point, is a feature of this element. Cerium is the only known element for which the critical point exists in the *p*–*T* phase diagram.

The critical transition was experimentally studied in, e.g., [1–4], where the following coordinates of the critical point on the *p*–*T* phase diagram were obtained: $T_c = 550$ K and $p_c = 1.8$ GPa [1, 2], $T_c = 630$ K and $p_c = 2$ GPa [3], and $T_c = 480$ K and $p_c = 1.45$ GPa [4]. The α–γ transition has been theoretically analyzed in numerous works [5–11]. However, the critical transition in cerium remains poorly studied.

In this work, we quantitatively describe the difference between the volumes of the α and γ phases as a function of temperature and pressure, particularly along the line of the isomorphic α–γ phase transition up to the critical point (T_c, p_c).

At various temperatures and normal pressure, four equilibrium polymorphic phases α, β, γ, and δ are possible for cerium. The α and γ phases are structure isomorphic (see table) and they have the A1 fcc structure with four atoms in the unit cell. The size of the unit cell of the γ phase is much larger than that of the α phase. The difference between their specific volumes is equal to 15–20% at $T = 297$ K [3, 5].

Direct $\alpha \longrightarrow \gamma$ and $\gamma \longrightarrow \alpha$ transitions are observed for increased pressures (above 0.2 GPa), as well as for overcooling.

The difference $\Delta H_{\alpha\gamma} = H_\alpha - H_\gamma$ between the enthalpies of the α and γ phases as a function of temperature and pressure can be described by the expression [15]

$$\Delta H_{\alpha\gamma} = \Delta H_0 \exp\left(-a\left[\frac{T}{T_c}\right]^4 + \left(\frac{p}{p_c}\right)^4\right)\eta, \qquad (1)$$

where the pressure is taken into account and $\Delta H_{\alpha\gamma} = (H_\alpha - H_\gamma)_{T,p}$, $\Delta H_0 = (H_\alpha - H_\gamma)_{0,p_0}$ is the difference between the enthalpies of the α and γ phases for temperature T and pressure p ($T = 0$ and pressure p_0). For $\eta = 1$, $a = \mu_0$, where the constant $\mu_0 = 0.75$ is determined from the condition of the maximum of the derivative $\frac{\partial \Delta H_{\alpha\gamma}}{\partial T}$. For $\eta \neq 1$ $a = \mu_0 \frac{\sqrt{2}}{2}$. For the temperature T_c and pressure p_c at the critical point, $\Delta H_{\alpha\gamma} = 0$, and the temperature and pressure derivatives of $\Delta H_{\alpha\gamma}$ are maximal when $\eta \neq 1$. In what follows, we take the correlating limiting function η in the form

$$\eta = \exp\left(-c\tan^2\left[\frac{\pi}{2}\alpha\frac{\left(\frac{T}{T_c}\right)^4 + \left(\frac{p}{p_c}\right)^4}{2}\right]^2\right),$$

where c and α are constants. For $\eta = 1$, $\alpha = 1$. For $\eta \neq 1$, α lies in the range 0.97–1 and it corrects the position of the maxima of the derivatives $\frac{\partial \Delta H_{\alpha\gamma}}{\partial T}$ and $\frac{\partial \Delta H_{\alpha\gamma}}{\partial p}$. The constant c cutting the function η lies in the range 0.001–0.01.

For variable pressure and constant temperature $T = T_1$,

$$\Delta H_{\alpha\gamma_{T_1,p}} = \Delta H_{\alpha\gamma_{T_1,p_0}} \exp\left(-a\left[\left(\frac{T_1}{T_c}\right)^4 + \left(\frac{p}{p_c}\right)^4\right]\right)\eta. \quad (1a)$$

For variable temperature and constant pressure $p = p_1$,

$$\Delta H_{\alpha\gamma_{T,p_1}} = \Delta H_{\alpha\gamma_{0,p_1}} \exp\left(-a\left[\left(\frac{T}{T_c}\right)^4 + \left(\frac{p_1}{p_c}\right)^4\right]\right)\eta. \quad (1b)$$

The difference between the enthalpies of the γ and α phases varies when $T \longrightarrow 0$, because the number of valence electrons and the distribution of their interatomic electron density in the crystal lattice of cerium

Moscow State University of Environmental Engineering, ul. Pryanishnikova 9, Moscow, 127550 Russia
e-mail: n.sirota@ru.net, an12tonm@mail.ru

1028-3358/05/5006-0299$26.00

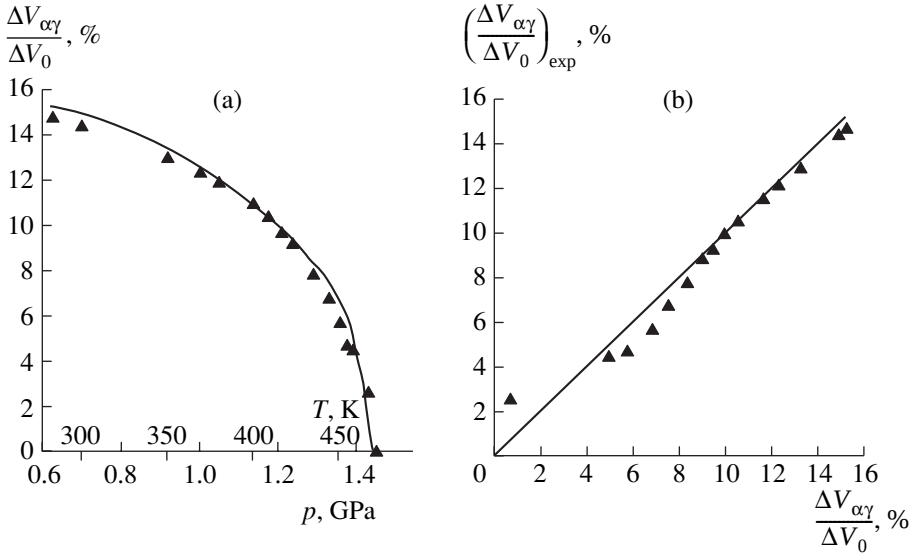

Fig. 1. (a) Variation in the relative difference between the volumes of the α and γ phases along the α–γ phase equilibrium curve and (b) experimental-versus-calculated relative differences between the specific volumes of the α and γ phases along the phase equilibrium curve.

vary. The difference between the enthalpies is quantitatively described as a function of pressure and temperature by Eqs. (1), (1a), and (1b). When pressure and temperature increase, the difference between the enthalpies decreases to a minimum at the end point (T_c, p_c), where $\Delta H_{\alpha\gamma} = 0$ and, therefore, the α and γ phases become completely identical.

If the difference between the specific volumes V_α and V_γ of the α and γ phases is proportional to the difference between the enthalpies as a function of temperature and pressure, we obtain

$$\Delta V_{\alpha\gamma} = \Delta V_0 \exp\left(-a\left[\left(\frac{T}{T_c}\right)^4 + \left(\frac{p}{p_c}\right)^4\right]\right)\eta. \qquad (2)$$

Figure 1a shows variation in the difference between the molar volumes of the α and γ phases with temperature and pressure along the phase equilibrium curve. This difference is calculated by Eq. (2) for T_c = 480 K and p_c = 1.45 GPa [4], a = 0.5, c = 0.0067, and α = 1. The experimental points taken from [4] are also shown in Fig. 1a. Figure 1b demonstrates good agreement between experimental and calculated values.

The difference between the specific heats of the α and γ phases as a function of temperature is determined as the temperature derivative $\frac{\partial \Delta H_{\alpha\gamma}}{\partial T}$ of the difference between enthalpies, assuming that the lattice components of the specific heats, as well as the characteristic

Cerium phases at normal pressure, lattice constants, density ρ, phase transition temperature T_t, and changes in enthalpy ΔH and volume ΔV in the polymorphic transition

Phase	Structure	Spatial group	Lattice constant, nm [14]	ρ, g/cm^3 [14]	T_t, K [12, 13]	ΔH, J/mol [12, 13]	ΔV, cm^3/mol [12]
α	fcc	$Fm3m$	a = 0.485, T = 77 K	8.23	α → β		
					143	1955	3.2
β	dhcp	$P6_3/mmc$	a = 0.368, c = 1.186, c/a = 0.16063, T = 298 K	6.66	β → γ		
					~346	54.4	−0.074
γ	fcc	$Fm3m$	a = 0.516, T = 296 K	6.768	γ → δ		
					1003	2973	−0.037
δ	bcc	$Im3m$	a = 0.412, T = 1030 K	6.770	δ → liquid		
					1077	5234	−0.140

temperatures of the α and γ phases, are equal to each other in this temperature range:

$$\Delta C_{p_{\alpha\gamma}} = \Delta H_0 \exp\left(-a\left[\left(\frac{T}{T_c}\right)^4 + \left(\frac{p}{p_c}\right)^4\right]\right)\eta \times\left(\frac{-4a}{T_c}\left(\frac{T}{T_c}\right)^3 + \frac{\partial\eta}{\partial T}\right). \quad (3)$$

Figure 2 shows variation in the difference between the specific heats with temperature and pressure along the phase-transition line. As is seen in this figure, a sharp extremum corresponding to a second order phase transition appears on the curve $\Delta C_{p_{\alpha\gamma}}(T)$ at temperature T_c in the critical transition region.

The temperature dependence of the difference between the thermal expansion coefficients is determined by the temperature derivative of the difference between the molar volumes of the α and γ phases, which is divided by the averaged volume $\bar{V}_0 = \frac{V_{\alpha 0} + V_{\gamma 0}}{2}$ of these phases:

$$\frac{1}{\bar{V}_0}\frac{\partial \Delta V_{\alpha\gamma}}{\partial T} = \beta_\alpha - \beta_\gamma = \frac{\Delta V_0}{\bar{V}_0}\exp\left(-a\left[\left(\frac{T}{T_c}\right)^4 + \left(\frac{p}{p_c}\right)^4\right]\right)\eta\left(\frac{-4a}{T_c}\left(\frac{T}{T_c}\right)^3 + \frac{\partial\eta}{\partial T}\right). \quad (4)$$

The temperature dependence of the difference between the thermal expansion coefficients of the α and γ phases displays a sharp peak near the critical point and is similar to the curve $\Delta C_{p_{\alpha\gamma}}(T)$ in Fig. 2. The presence of a sharp peak in the temperature dependence of the difference between the thermal expansion coefficients of the α and γ phases at transition temperatures was experimentally indicated in [4], but the shape of the peak in that work differs from that obtained in our work.

The ratio of the pressure derivative of the difference between the molar volumes of the α and γ phases to $\bar{V}_0$ determines the pressure and temperature dependences of the difference between the compressibility factors χ_α and χ_γ of these phases.

Using Eqs. (1) and (2), we calculate the end curve for the difference between the isomorphic α and γ phases on the *p*–*T* phase diagram. This curve corresponds to $\Delta H_{\alpha\gamma} = \Delta V_{\alpha\gamma} = 0$. Figure 3 shows the end curve in the *p*–*T* phase diagram in the regions of the metastable existence of the α phase and equilibrium existence of the γ phase, as well as the metastable existence of the γ phase and equilibrium existence of the α phase. Figure 3 also shows the contours of the ratio $\frac{\Delta V_{\alpha\gamma}}{\Delta V_0}$, as well as the experimental points taken from [4] for the difference between the volumes of the α and γ phases along the phase equilibrium curve [4]. The experimental points agree with the contours.

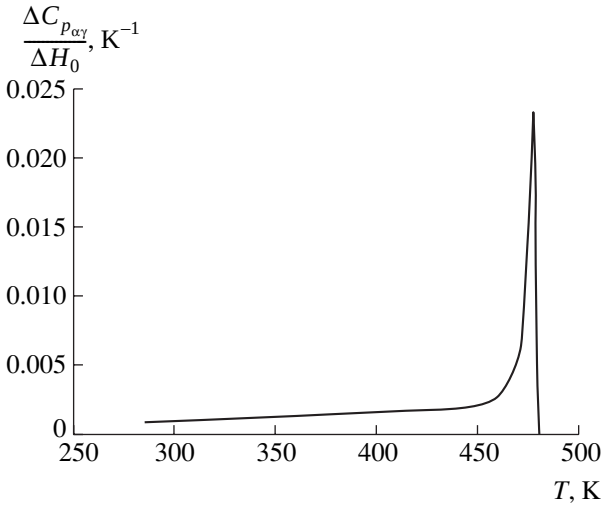

Fig. 2. The variation in the difference between the specific heats of the α and γ phases that is divided by ΔH_0 along the α–γ phase equilibrium curve near the end temperature.

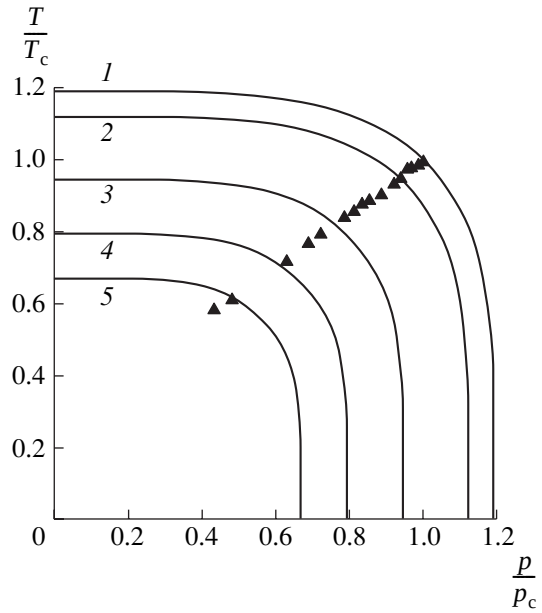

Fig. 3. (*1*) Variation in the position of the end point ($\Delta V_{\alpha\gamma} = 0$) with temperature and pressure and contours of the relative difference between the volumes of the α and γ phases $\frac{\Delta V_{\alpha\gamma}}{\Delta V_0}$ = (*2*) 6.96, (*3*) 11.02, (*4*) 13.5, and (*5*) 14.93%.

Thus, the temperature and pressure dependences of the thermodynamic and thermal properties of cerium

are satisfactorily described by an exponential law, which approximates the differences between their enthalpies and molar volumes as functions of temperature and pressure.

REFERENCES

1. E. G. Ponyatovskiĭ, Dokl. Akad. Nauk SSSR **120** (5), 1021 (1958) [Sov. Phys. Dokl. **2**, 498 (1958)].
2. A. Jayaraman, Phys. Rev. **137**, A179 (1965).
3. R. I. Beecroft and C. A. Swenson, J. Phys. Chem. Solids **15**, 234 (1960).
4. A. R. Kutsar, *Structure of Phases, Phase Transformations, and Phase Diagrams of Metallic Systems* (Nauka, Moscow, 1974), p. 76 [in Russian].
5. W. H. Zachariasen, Phys. Rev. **76**, 301 (1949).
6. J. W. Allen and R. M. Martin, Phys. Rev. Lett. **49**, 1106 (1982).
7. B. Johansson, Philos. Mag. **30**, 469 (1974).
8. P. B. Coqblin and A. Blandin, Adv. Phys. **17**, 281 (1968).
9. R. Ramirez and L. M. Falikov, Phys. Rev. B **3**, 2425 (1971).
10. I. L. Aptekar' and E. G. Ponyatovskiĭ, Fiz. Met. Metalloved. **25**, 777 (1968).
11. B. Johansson, I. Abrikosov, M. Alden, *et al.*, Phys. Rev. Lett. **74**, 2335 (1995).
12. K. A. Gschneider, R. Elliot, and R. McDonald, J. Phys. Chem. Solids **23**, 555 (1962).
13. F. H. Spedding, J. J. McKeown, and A. H. Daane, J. Phys. Chem. **64**, 289 (1960).
14. *The Rare Earths*, Ed. by F. H. Spedding and A. H. Daane (Wiley, New York, 1961; Metallurgiya, Moscow, 1965).
15. N. N. Sirota, Dokl. Akad. Nauk **402**, 329 (2005) [Dokl. Phys. **50**, 42 (2005)].

Translated by R. Tyapaev

Doklady Physics, Vol. 50, No. 6, 2005, pp. 303–307. Translated from Doklady Akademii Nauk, Vol. 402, No. 6, 2005, pp. 754–758.

PHYSICS

Spinodal and the Melting Curve of a Lennard-Jones Crystal at Negative Pressure

V. G. Baĭdakov* and S. P. Protsenko

Presented by Academician V.P. Skripov November 12, 2004

Received December 3, 2004

Liquids and crystals can exist in the metastable phase at negative pressures. Such metastability is primarily attributed to the instability of condensed phases with respect to the formation of a gaseous phase in these liquids and crystals. The maximum tensions of fluids and crystals are limited by spinodals, i.e., lines on which their isothermal elasticity vanishes.

Two macroscopic phases that are instable with respect to the formation of a certain third phase in them may coexist in equilibrium [1, 2]. Thus, the fluid–crystal phase equilibrium line must have an analytic continuation to the negative-pressure region. At pressures below the triple point, both a fluid that is overcooled beyond this line and a crystal that is overheated beyond this line are doubly metastable. The positions of the melting curve and spinodals of the fluid and crystal on the thermodynamic surface of state and their low-temperature asymptotic behaviors are of interest. In this work, these problems are solved using the molecular dynamic method.

We analyze a system consisting of 2048 Lennard-Jones particles with a mass of $m = 66.336 \times 10^{-27}$ kg. The potential parameters are $\sigma = 0.3405$ nm and $\frac{\varepsilon}{k} = 119.8$ K, where k is the Boltzmann constant. In what follows, σ, ε, and m values are used as the reduction parameters for thermodynamic quantities. Reduced (dimensionless) quantities are marked by asterisks.

We consider that particles are situated in a cubic cell at whose boundaries periodic boundary conditions are imposed. In order to integrate the classical equations of motion of particles, the Beemon scheme is used [3]. The time integration step is taken to be 0.01 and 0.005 ps for the fluid and crystal, respectively. The interparticle interaction potential is cut at a distance of $r_c^* = \frac{r_c}{\sigma} = 6.78$ for a density of $\rho^* = \rho\sigma^3 \le 0.82$. The cutoff radius is taken to be half the cell edge length if $\rho^* > 0.82$. The thermodynamic properties (temperature, pressure, potential and kinetic energies, and specific heat at constant volume) of the fluid and crystalline phases are calculated in the N, V, E ensemble along 11 isotherms in the interval $T^* = \frac{kT}{\varepsilon} = 0.1$–$2.0$. The calculation procedure was described in [4].

Calculations always begin from the stable region. A random arrangement and an fcc lattice are taken as the initial configurations of particles in a cell for the fluid and crystal, respectively. For temperatures $T^* = 0.7$–2.0, the metastable region of the fluid is reached by sequential isothermal compression of particles in the cell. The final configuration of particles at each given density is the initial configuration for calculation of the state with a higher density. Data on the thermodynamic properties of the fluid in the negative-pressure region are obtained by isochoric cooling of the particle configuration that is in equilibrium at $T^* = 0.7$ and $\rho^* = 0.85$ to temperatures $T^* = 0.55$ and 0.4, with subsequent tension and compression. The characteristic time in which the system reaches equilibrium is equal to 0.5 and 1 ns in the stable and metastable regions, respectively. The calculated quantities were averaged over a time interval from 5 to 10 ns.

Figure 1a shows pressure calculated for the fluid phase. The last points corresponding to the highest densities on the isotherms determine the maximum overcooling of the fluid in the model. The last points corresponding to the lowest density on the isotherms $T^* = 0.4$, 0.55, and 0.7 determine the maximum tension preceding the boiling of the fluid.

According to Fig. 1a, an increase in density (pressure) is accompanied by an increase in the isothermal elasticity of the irregular structure. Thus, thermodynamic stability under infinitely small long-wavelength density perturbations does not decrease for the fluid phase to the maximum overcooling point. This statement is consistent with the absence of the spinodal for an overcooled single-component fluid [5] and is corroborated by the density dependences of the internal

Institute of Thermal Physics, Ural Division, Russian Academy of Sciences, ul. Amundsena 106, Yekaterinburg, 620016 Russia

** e-mail: baid@itp.uran.ru*

1028-3358/05/5006-0303$26.00

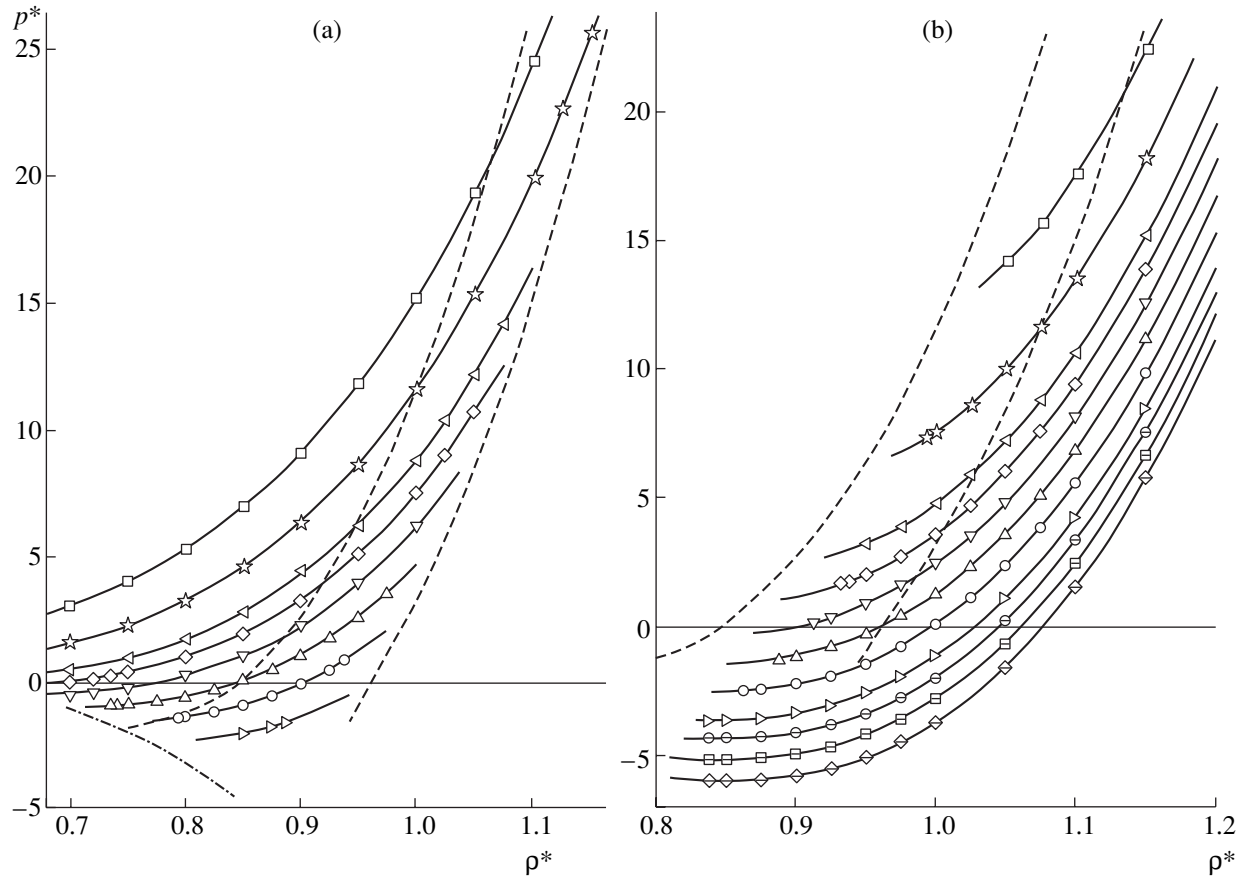

Fig. 1. Isotherms of the (a) fluid and (b) crystal for $T^* = (\diamondsuit)$ 0.1, $(\boxminus)$ 0.2, $(\ominus)$ 0.3, $(\triangleright)$ 0.4, $(\bigcirc)$ 0.55, $(\triangle)$ 0.7, $(\triangledown)$ 0.85, $(\diamond)$ 1.0, $(\triangleleft)$ 1.15, $(\star)$ 1.5, and $(\square)$ 2.0. The dashed lines are the fluid–crystal phase transition lines and the dash–dotted line is the spinodal of the extended fluid.

energy u and specific heat at constant volume c_v. Specific heat at constant volume on the isotherm reaches a maximum at the boundary of the overcooled-state region for the fluid phase. According to the thermodynamic relation

$$\rho^2\left(\frac{\partial c_v}{\partial \rho}\right)_T = -T\left(\frac{\partial^2 p}{\partial T^2}\right)_\rho, \qquad (1)$$

the pressure isochore changes its curvature from convex to concave at the extreme point of c_v. This property ensures the validity of the condition $\left(\frac{\partial p}{\partial T}\right)_\rho \longrightarrow 0$ for $T \longrightarrow 0$ and the absence of the envelope, i.e., spinodal, for isochores.

In calculations of the properties of the crystalline phase, the initial state on the isotherm is always the state with the highest density. Calculations were performed up to the extensions at which the crystalline order of particles disappears in the model. When approaching this point, the thermodynamic stability of the crystalline phase decreases (Fig. 1b). The dependence $p(\rho)$ is consistent with the existence of such points on isotherms, at which $\left(\frac{\partial p}{\partial \rho}\right)_T = 0$, i.e., with the existence of a spinodal. According to Fig. 1b, the destruction of the crystal structure at high temperatures occurs quite far away from the spinodal. As temperature decreases, the derivative $\left(\frac{\partial p}{\partial \rho}\right)_T$ at the boundary of the spontaneous-disorder region decreases, and the destruction of the crystal structure at $T^* \le 0.4$ occurs for tensions close to spinodal tensions. This conclusion is consistent with general concepts from the thermal activation theory of nucleation [6]. For low temperatures, although the work W_* of the formation of the critical nucleus decreases as supersaturation increases, the probability of the formation of the nucleus decreases as $\exp\left(-\frac{W_*}{kT}\right)$ due to the temperature factor ($T \longrightarrow 0$). In real systems at temperatures close to absolute zero, the thermal activation mechanism of nucleation changes to the quantum one [7].

In computer experiments, weak quantum effects can be taken into account in terms of the semiclassical

expansion of the partition function [8]. The calculation of the first quantum correction shows its immaterial effect on the behavior of the stability of the crystalline phase for temperatures $T^* > 0.4$ and for densities close to the boundary of the spontaneous-disorder region.

Data for P, ρ, and T in the fluid and crystalline phases of the Lennard-Jones system are approximated by the local equations of state of the form

$$p^* = \sum_{j=0}^{n}\sum_{i=0}^{m} a_{ij}\rho^{*j}T^{*i}. \quad (2)$$

The coefficients of Eqs. (2), as well as the maximum values of the exponents n and m, were determined using the regression analysis method. For the fluid phase, $a^{l}_{01} = 12.727$, $a^{l}_{02} = -31.7465$, $a^{l}_{05} = 14.9614$, $a^{l}_{12} = -18.1082$, $a^{l}_{13} = 75.0892$, $a^{l}_{14} = -61.2481$, $a^{l}_{15} = 19.1732$, $a^{l}_{21} = 1.80406$, $a^{l}_{22} = -5.71191$, and $a^{l}_{32} = 0.64104$. The standard deviation of p is equal to 0.0266 over the entire data set. For the crystalline phase with nearly the same error of description of data that are obtained for p, ρ, and T in the molecular dynamic experiment, the regression analysis leads to a set of equations in which the continuation of isotherms over the spontaneous-disorder line exhibits a different character. Owing to this circumstance, the approximation of the spinodal of the crystalline phase at high temperatures is not unique. One of the resulting sets of the coefficients, which will be used to determine the phase-equilibrium line, is as follows: $a^{cr}_{00} = -69.8834$, $a^{cr}_{01} = 286.813$, $a^{cr}_{02} = -412.723$, $a^{cr}_{03} = 191.151$, $a^{cr}_{10} = 9.46960$, $a^{cr}_{20} = -31.8944$, $a^{cr}_{21} = 47.2784$, $a^{cr}_{22} = -17.2507$, $a^{cr}_{30} = 71.9482$, $a^{cr}_{31} = -170.891$, $a^{cr}_{32} = 135.637$, and $a^{cr}_{33} = -36.0205$. The error of the approximation of pressure by the equation with these coefficients is equal to 0.0146. Figure 1 shows results from the description of p, ρ, and T for the fluid and crystal by Eqs. (2).

The single-component two-phase system is in equilibrium when the temperature, pressure, and chemical potential of one coexisting phase are equal to the respective quantities of the other coexisting phase. The molecular dynamic method does not allow direct calculations of the chemical potential and free energy. However, the internal energy is calculated quite simply in this method. The internal energy is related to the thermal equation of state as

$$\left(\frac{\partial u}{\partial \rho}\right)_T = \left(\frac{\partial\left(\beta\frac{p}{\rho^2}\right)}{\partial p}\right)_\rho, \quad (3)$$

where $\beta = \frac{1}{T}$. Integration of Eqs. (2) and (3) with respect to density yields the function u that includes a certain temperature function $u_0(T)$, which is determined from the results of the molecular dynamic calculation of the internal energy. Using the function $u(\rho, T)$ and integrating the Gibbs–Helmholtz equation

$$\left(\frac{\partial(\beta f)}{\partial \beta}\right)_T = u, \quad (4)$$

we determine the free energies of the fluid and crystalline phases that include a certain constant f_0. This constant is determined from the parameters calculated for the triple point of the Lennard-Jones system in a special computer experiment. According to our data, which is consistent with the results of [9], $T^*_t = 0.692$, $p^*_t = 0.0012$, $\rho^*_{t,l} = 0.847$, and $\rho^*_{t,cr} = 0.962$.

Figures 1 and 2 show the melting curve calculated for the positive- and negative-pressure regions. In Figs. 1a and 2, the spinodal of the extended fluid is shown as calculated for $T^* \le 0.7$ from equation of state (2) and for $T^* > 0.7$ from the equation of state for the Lennard-Jones fluid taken from [10]. As is seen in Fig. 2a, the melting curve in the negative-pressure region ends on the spinodal of the extended fluid. As can be shown, at point A where the metastable continuation of the melting curve intersects the spinodal, the following relation is valid:

$$\left(\frac{dp}{dT}\right)_{m,A} = \left.\frac{\Delta s}{\Delta v}\right|_A \neq \left(\frac{dp}{dT}\right)_{sp,A} = \left(\frac{dp}{dT}\right)_{\rho,A}, \quad (5)$$

where Δs and Δv are the jumps of entropy and volume, respectively, on the melting curve. For the Lennard-Jones system, $T^*_A = 0.5286$, $p^*_A = -1.7128$, $\rho^*_{l,A} = 0.7374$, $\rho^*_{cr,A} = 0.9423$, $\left(\frac{dp^*}{dT^*}\right)_{sp,A} = 4.748$, and $\left(\frac{dp^*}{dT^*}\right)_{m,A} = 8.480$. Because the slopes of the tangent to the spinodal and melting curve at point A on the (p, T) plane are not equal to each other,

$$\left(\frac{\partial p}{\partial v}\right)_{T,A}\left(\frac{dv}{dT}\right)_{m,A} \neq 0. \quad (6)$$

Because $\left(\frac{\partial p}{\partial v}\right)_T = 0$ at the point of the intersection of the spinodal and melting curve, inequality (6) and condition $\left(\frac{dp}{dT}\right)_{m,A} > \left(\frac{dp}{dT}\right)_{sp,A}$ are valid if $\left(\frac{dT}{dv}\right)_{m,A} = 0$ and $\left(\frac{d^2T}{dv^2}\right)_{m,A} \neq 0$. In this case, point A on the

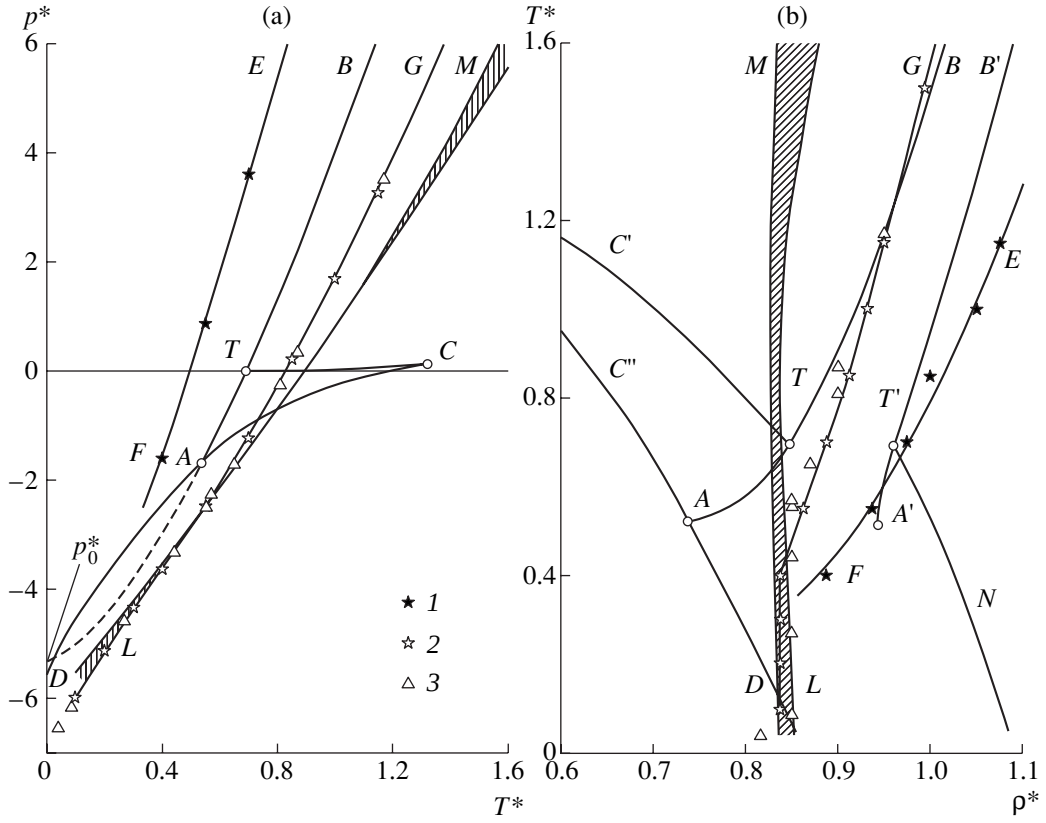

Fig. 2. (a) (p, T) and (b) (T, ρ) projections of the lines of the phase transitions fluid–crystal (*BTA* and *B*'*T*'*A*'), fluid–gas (*CT* and *C*'*T*), and crystal–gas (*T*'*N*); spinodals of the extended fluid (*CAD* and *C*''*AD*) and extended crystal (*ML*); lines of the attainable overcooling of the fluid (*EF*, *1*) and overheating of the crystal (*GL*, *2*, *3*). The critical point, triple point, and point of the intersection of the melting curve and spinodal are indicated as *C*, *T*, and *A*. Data *1* and *2* were obtained in this work and data *3* were taken from [15].

(T, $v = \frac{1}{\rho}$) plane is the point of a minimum of the fluid branch of the crystal–fluid phase equilibrium line. Thus, the point of the termination of crystal–fluid phase equilibrium is a singular point on the thermodynamic surface of states of the single-component system.

In Fig. 2a, the dashed line continuing over point *A* is the approximation of the melting curve by the Simon equation

$$p_m^* = p_0^*\left[\left(\frac{T^*}{T_0^*}\right)^c - 1\right], \qquad (7)$$

where $p_0^* = -5.328$, $T_0^* = 0.693$, and $c = 1.509$. This equation reproduces the melting curve with high accuracy in both the positive- and negative-pressure regions. In the limit $T \longrightarrow 0$, the limiting pressure $p_0^* = p_m^*(0)$ on the melting curve in the Simon-equation approximation is close to the limiting pressure $p_{sp,l}^*(0)$ on the spinodal of the fluid. Although the extrapolation of the melting curve over the spinodal has no physical meaning, the correlation between p_0^* and $p_{sp,1}^*(0)$ is important for the determination of the thermodynamic similarity of substances in the crystal–fluid and fluid–vapor phase transitions [2]. The possibility of the termination of metastable equilibrium in the fluid–crystal system on the spinodal of the extended fluid was mentioned in [6] and discussed in [11].

The spinodal that is constructed for the overheated Lennard-Jones crystal using the family of local equations of state is shown by a shaded band in Fig. 2. The width of this band determines the error of the spinodal approximation. The error increases with temperature. The spinodal of the crystalline phase on the (p, T) plane for low temperatures lies somewhat lower than the spinodal of the extended fluid phase. The condition $\left(\frac{\partial p}{\partial \rho}\right)_T = 0$ is valid for both phases at the point of intersection of the boundaries of thermodynamic stability of the fluid and crystal in the (p, T) coordinates.

Under the assumption that the destruction of metastable states in the model occurs through the nucleation mechanism (see [12]), the nucleation frequency at the extreme points of the isotherms of the overcompressed fluid and extended crystal is estimated by the formula $J = (V\bar{\tau})^{-1}$, where V is the metastable-phase volume and $\bar{\tau}$ is the mean expectation time for the first viable

nucleus. For the conditions of the molecular dynamic experiment under discussion, $V \simeq 8 \times 10^{-20}$ cm^3 and $\bar{\tau} \simeq 10$ ns (time over which the parameters are averaged). In this case, $J \simeq 10^{27}$ cm^{-3} s^{-1}. Figure 2a shows the boundaries of attainable overcooling of the fluid and overheating of the crystal in the Lennard-Jones system for a given nucleation frequency. The data presented here for the fluid and crystalline phases agree well with the results reported in [13–15]. As temperature decreases, the boundary of the attainable overheating of the crystal approaches the spinodal.

Thus, the computer experiment described above has revealed that the metastable continuation of the melting curve does not reach the $T = 0$ isotherm in the limit $T \longrightarrow 0$ but ends on the spinodal of the extended fluid for nonzero temperature. The point of the intersection of the melting curve and spinodal is a singular point on the thermodynamic surface of states of the single-component system. In the low-temperature limit, the spinodals of the extended fluid and crystal approach each other and display similar values of pressure and density at $T = 0$.

ACKNOWLEDGMENTS

This work was supported by the Presidium of the Russian Academy of Sciences (program "Thermal Physics and Mechanics of Intense Energy Actions") and the Russian Foundation for Basic Research (project no. 02-02-16106).

REFERENCES

1. V. P. Skripov, in *Nonequilibrium Phase Transitions and Thermophysical Properties of Substances* (Ural. Otd. RAN, Yekaterinburg, 1996), pp. 3–10 [in Russian].
2. V. P. Skripov and M. Z. Faĭzullin, *Crystal–Liquid–Vapor Phase Transitions and Thermodynamic Similarity* (Fizmatlit, Moscow, 2003) [in Russian].
3. D. J. Beemon, Comput. Phys. **20** (2), 130 (1976).
4. V. G. Baĭdakov and S. P. Protsenko, Teplofiz. Vys. Temp. **41** (2), 231 (2003).
5. V. P. Skripov and V. G. Baĭdakov, Teplofiz. Vys. Temp. **10** (6), 1226 (1974).
6. V. P. Skripov and V. P. Koverda, *Spontaneous Crystallization of Supercooled Liquids* (Nauka, Moscow, 1984) [in Russian].
7. V. G. Baĭdakov, *Overheating of Cryogenic Liquids* (Ural. Otd. RAN, Yekaterinburg, 1995) [in Russian].
8. L. D. Landau and E. M. Lifshitz, *Statistical Physics*, 3rd ed. (Nauka, Moscow, 1976; Pergamon Press, Oxford, 1980), Vol. 1, Parts 1 and 2.
9. M. A. Barroso and A. L. Ferreira, J. Chem. Phys. **116** (16), 7145 (2002).
10. G. Sh. Boltachev and V. G. Baĭdakov, Teplofiz. Vys. Temp. **41** (2), 314 (2003).
11. I. L. Iosilevskiĭ and A. Yu. Chigvintsev, http://zhurnal.ape.relarn.ru/articles/2003/003.pdf, pp. 957–961.
12. V. G. Baĭdakov and S. P. Protsenko, Dokl. Akad. Nauk **394** (6), 752 (2004) [Dokl. Phys. **49**, 69 (2004)].
13. V. G. Baĭdakov, A. E. Galashev, and V. P. Skripov, Fiz. Nizk. Temp. **2** (8), 957 (1976) [Sov. J. Low Temp. Phys. **2**, 469 (1976)].
14. V. G. Baĭdakov, A. E. Galashev, and V. P. Skripov, Fiz. Tverd. Tela (St. Petersburg) **22** (9), 2681 (1980) [Sov. Phys. Solid State **22**, 1565 (1980)].
15. A. Yu. Kuksin, G. E. Norman, and V. V. Stegailov, in *Proceedings of ICCP6-CCP2003* (Rinton, Beijing, 2004).

Translated by R. Tyapaev

Doklady Physics, Vol. 50, No. 6, 2005, pp. 308–310. Translated from Doklady Akademii Nauk, Vol. 402, No. 6, 2005, pp. 759–761.

PHYSICS

Transient Growth and Optimal Perturbations with the Simplest Dynamic Model As an Example

I. G. Shukhman

Presented by Academician A.M. Fridman January 14, 2005

Received January 17, 2005

There is a well-known discrepancy that arises in connection with describing the transition to turbulence in viscous shear flows. The linear stability theory often predicts the stability (exponential damping) for all eigenmodes of the linearized set of Navier–Stokes equations at sufficiently small Reynolds numbers for which actual flows are already turbulent (see, e.g., [1, 2]).

For example, the theory predicts the stability for the plane Poiseuille flow when Re < 5772 [3, 4] and for the cylindrical Poiseuille flows at all Reynolds numbers. The Couette flow between two plates is also stable for all Reynolds numbers. Experiments were performed in practically ideal conditions when the effect of various perturbing causes (including the roughness of the wall) on the flow was completely suppressed. Nevertheless, these experiments have shown that the flows are turbulent in the case of Reynolds numbers for which, in accordance with the linear stability theory, they must be exponentially stable. A more detailed list of similar situations with indicated exact Reynolds numbers for which the transition had occurred was discussed, e.g., in [5].

In recent years, certain expectations associated with the so-called optimal-perturbation theory [6] have appeared in hydrodynamics. The essence of this theory is the fact that, at a certain stage of evolution of an initial-perturbation, growth is possible in systems that are stable with respect to exponentially growing perturbations. This growth is called transient, insofar as it is usually replaced in the end by the usual ordinary viscous damping. The initial perturbation (among the infinite number of various possible ones) for which the amplification factor $\mathcal{K} \equiv \dfrac{E_{\max}}{E_0}$ attains the highest value is called optimal. Here, E is a certain positive definite quadratic functional (usually, the total energy) featuring the given perturbation and $E_{\max}$ and E_0 are its maximum value in the course of the evolution and its value at the initial instant of time, respectively. As has been shown by numerous calculations performed in recent years for different flow models, the value of $\mathcal{K}_{\text{opt}}$ can attain tens of thousands [7–9]. The expectations mentioned above are associated with the fact that the transient growth of optimal perturbations can result in a transition even in systems that are stable in the usual sense.

It is worth noting that the range of problems in which the concept of transient growth has been exploited is not restricted to the purely hydrodynamic flows of incompressible fluids. These concepts have also been actively discussed (being associated with various astrophysical applications) in connection with more complicated situations. We refer here to phenomena in which the gravitation and self-gravitation of a medium, as well as its compressibility, play an important role. As examples, we may point to the regenerative theory of spiral-structure formations in galaxies by Goldreich and Lynden-Bell [10], as well as estimates of the turbulent viscosity in both accretion disks and the Galaxy gas disk [11, 12].

The formal cause for the transient growth of shear flows in channels is associated with the fact that the set of linearized Navier–Stokes equations for three-dimen-

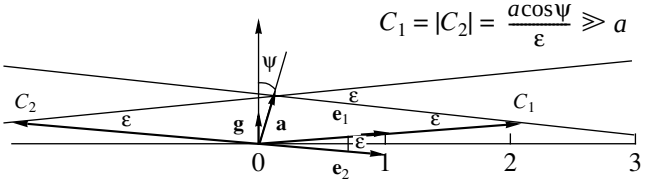

Decomposition of the vector **a** over almost parallel basis vectors $\mathbf{e}_1$ and $\mathbf{e}_2$. The angle $\varepsilon \ll 1$ is the angle between the vectors $\mathbf{e}_1$ and $\mathbf{e}_2$; the angle ψ is the angle between **a** and $\mathbf{g} = \mathbf{e}_1 - \mathbf{e}_2$. C_1 and $|C_2|$ are the lengths of the projections along the vectors $\mathbf{e}_1$ and $\mathbf{e}_2$, respectively.; $C_1 \approx -C_2 \approx a\cos\dfrac{\psi}{\varepsilon} \gg a$.

Institute of Solar–Terrestrial Physics, Siberian Division, Russian Academy of Sciences,
P. O. Box 4026, Irkutsk, 664033 Russia
e-mail: shukhman@iszf.iirk.ru

1028-3358/05/5006-0308$26.00

sional perturbations[1] is described by the so-called nonnormal operator [1, 6]. For example, in the most thoroughly studied case of three-dimensional perturbations of the plane oblique-wave type, in plane-parallel flows of an incompressible homogeneous fluid, the combination of Orr–Sommerfeld and Squire operators [1] is taken for this operator. The eigenfunctions of such nonnormal operators are not mutually orthogonal. Therefore, even in the case when all eigenfunctions correspond to the damping, nevertheless, temporal growth is possible. This idea is routinely used in the literature in explanation of the transient-growth phenomenon. However, in our opinion, this explanation is true but not evident, which hampers understanding its essence. The present study is aimed to fill in this gap.

Considering a simple dynamical system (with only two degrees of freedom) whose state is described by the usual two-dimensional vector lying in a plane, we now demonstrate the essence of transient growth as well as a method of separating the optimal perturbation.

Thus, let a dynamical system be described by the equation $\frac{d\mathbf{F}}{dt} = \hat{L}\,\mathbf{F}$ and have two eigenvectors $\mathbf{e}_1$ and $\mathbf{e}_2$ corresponding to the eigenvalues λ_1 and λ_2: $\hat{L}\,\mathbf{e}_1 = \lambda_1\mathbf{e}_1$, $\hat{L}\,\mathbf{e}_2 = \lambda_2\mathbf{e}_2$. Without a loss of generality, we can consider their length to be equal to unity, $|\mathbf{e}_1| = |\mathbf{e}_2| = 1$.

We show that when the vectors $\mathbf{e}_1$ and $\mathbf{e}_2$ are nonorthogonal (in the given example, it is implied in the usual sense, i.e., as $(\mathbf{e}_1 \times \mathbf{e}_2) \neq 0$), transient growth of the initial perturbation is possible even in the case when both eigenvalues correspond to the damping: $\lambda_1 \equiv -\gamma_1$, $\lambda_2 \equiv -\gamma_2$, and $\gamma_{1,2} > 0$. For greater clarity, we analyze the case in which the damping decrements are significantly different: $\gamma_1 \ll \gamma_2$, and the vectors $\mathbf{e}_1$ and $\mathbf{e}_2$, in themselves, are almost parallel, i.e., the angle ε is small, in other words, $\varepsilon \ll 1$.

Let the initial vector $\mathbf{a}$ ($t = 0$) be parallel to none of the basis vectors. (The case in which this vector is almost parallel to one of them is not of interest because, as is immediately evident, under these conditions, transient growth is impossible.) We now decompose the initial vector over this pair: $\mathbf{a}\ (t = 0) = C_1\mathbf{e}_1 + C_2\mathbf{e}_2$. It is easy to understand (see also the figure) that insofar as the vectors $\mathbf{e}_1$ and $\mathbf{e}_2$ are almost parallel, the coefficients of this decomposition must have opposite signs and must considerably exceed the length of the initial perturbation $a = |\mathbf{a}(t = 0)|$:

$$C_1 \approx -C_2 \approx a\cos\frac{\psi}{\varepsilon} \gg a. \qquad (1)$$

Here, ψ is the angle between the small vector $\mathbf{g} \equiv \mathbf{e}_1 - \mathbf{e}_2$, which is oriented almost perpendicularly to both basis vectors $\mathbf{e}_1$ and $\mathbf{e}_2$ (see figure) and the vector $\mathbf{a}(0)$.

At the instant of time t, we have

$$\mathbf{a}(t) = C_1\mathbf{e}_1\exp(-\gamma_1 t) + C_2\mathbf{e}_2\exp(-\gamma_2 t).$$

In the time $t \sim t_1$ after the evolution has begun, when $\frac{1}{\gamma_2} \ll t_1 \ll \frac{1}{\gamma_1}$, the projection of the vector $\mathbf{a}(t)$ of the perturbation onto the rapidly attenuating eigenvector $\mathbf{e}_2$ disappears, and the perturbation vector coincides with its initial component along the vector $\mathbf{e}_1$:

$$\mathbf{a}(t) \approx C_1\mathbf{e}_1\exp(-\gamma_1 t) \approx C_1\mathbf{e}_1.$$

In other words, it rotates along the vector $\mathbf{e}_1$ and its magnitude grows by the factor

$$K = \frac{C_1}{a} = \cos\frac{\psi}{\varepsilon} \gg 1. \qquad (2)$$

The significant growth of the initial perturbation is clearly seen. However, it is quite clear that this growth is only temporal (transient), since in the time $t \sim t_2 \gg \frac{1}{\gamma_1}$, the perturbation damps. From expression (2), it follows that the gain K in the perturbation amplitude

[1] For plane-parallel flows, with the velocity profile $U_x(y)$, perturbations are called three-dimensional provided that they depend on all three coordinates. In particular, perturbations can be oblique waves of the form $\sim f(y, t)\exp[i(k_x x + k_z z)]$, where $k_z \neq 0$. The dynamics of 3D perturbations considerably differs from that of 2D perturbations (independent of z and conserving the vorticity of a liquid particle in the nonviscous case) [1]. Generally speaking, the transient growth of perturbations is possible for both the 2D and 3D case. However, for 2D perturbations, there exists only one cause of transient growth. This is the so-called Orr mechanism [13] (see also [8]). For example, in the case of an initial perturbation in the form of a plane wave, in a flow with a constant shear, the growth is associated with the fact that, at certain relations between the shear signs for an unperturbed velocity $\alpha = \frac{dU_x}{dy}$ and the signs of the x and y components of the initial wave vector $\mathbf{k} = (k_x, k_y, 0)$ (namely, the quantities k_x, k_y, and α must be of the same sign), it turns out that in a certain time, the component $k_y(t)(\equiv k_y - \alpha t k_x)$ disappears, and the perturbation attains its maximum value at this instant of time. Then, even in the absence of viscosity, the power-like damping begins. The viscosity makes this damping more rapid (exponential). (It is worth noting that in studies devoted to the transient growth of perturbations in differential rotating gravitating disk-shaped systems [10–12], where the perturbations are two-dimensional by definition, this is the Orr 2D mechanism that is discussed in connection with the case of a circular flow.) For 3D perturbations, in addition to the Orr mechanism [13], there exists a more interesting and important mechanism of transient growth. This is the lift-up Landahl effect [14]. The essence of this effect is also very simple, and it becomes particularly obvious for initial perturbations that depend only on y and z ($k_x = 0$). In this case, the perturbation corresponds to the rotation of the entire liquid (with its shear of the streamwise velocity $\frac{dU_x}{dy}$) about the x axis. This rotation results in the algebraic (linear) growth of the streamwise velocity and in the formation of domains (over z) with higher and lower values of the streamwise velocity (streaks). In the particular case of a flow with a constant shear $U_x = \alpha y$, this algebraic growth was calculated for the first time in [15].

depends on the orientation ψ of the initial perturbation. In the case of

$$\psi = \psi_{opt} = 0, \tag{3}$$

this factor attains the maximum equal to $K_{opt} = \frac{1}{\varepsilon}$ so that

$$\mathcal{K}_{opt} = K_{opt}^2 = \frac{1}{\varepsilon^2}. \tag{4}$$

Thus, we have shown that the optimal initial vector $\mathbf{a}_{opt}$ is oriented almost along the normal to the basis vectors $\mathbf{e}_1$ and $\mathbf{e}_2$. The figure obviously illustrates the geometric sense of this amplification.

It follows from the example under consideration that transient growth is caused exclusively by the nonorthogonality of the basis vectors. This results in the fact that the decomposition coefficients, i.e., the lengths of the components along the basis vectors, exceed the length of the initial vector. After the extinction of the rapidly attenuating component, the resulting perturbation coincides with its slowly attenuating component, i.e., it is, in fact, noticeably increased compared to its initial value. It is also evident that this is impossible in a system in which eigenvectors are orthogonal, since the length of each of the projections of the initial vector is smaller than its length. Only monotonic damping can occur in this system.

In conclusion, we can show in more detail (in addition to the figure) why, in the case of the almost parallel unit basis vectors $\mathbf{e}_1$ and $\mathbf{e}_2$, the lengths of the components of an arbitrary vector $\mathbf{a}$ along each of them must significantly exceed the length of this vector (in the case, of course, when the direction of this vector is not nearly coincident with one of these basis directions).

The decomposition of the initial vector $\mathbf{a} = C_1\mathbf{e}_1 + C_2\mathbf{e}_2$ can also be represented as a decomposition over the almost orthogonal basis vectors $\mathbf{g}(=\mathbf{e}_1 - \mathbf{e}_2)$ and $\mathbf{e}_2$ (or $\mathbf{e}_1$). Indeed, we have

$$\mathbf{a} = C_1\mathbf{e}_1 + C_2\mathbf{e}_2 = C_1\mathbf{g} + (C_1 + C_2)\mathbf{e}_2.$$

The almost orthogonality of the vector $\mathbf{g}$ and the vectors $\mathbf{e}_1$ and $\mathbf{e}_2$ is evident from the figure and also follows formally from the simple estimate of the angle β between $\mathbf{g}$ and $\mathbf{e}_1$:

$$\cos\beta = \frac{\mathbf{g}\cdot\mathbf{e}_1}{|g|} = \frac{1-(\mathbf{e}_1\cdot\mathbf{e}_2)}{\varepsilon} = \frac{1-\cos\varepsilon}{\varepsilon} \approx \frac{\varepsilon}{2} \ll 1,$$

i.e.,

$$\beta = \frac{\pi}{2} - \frac{\varepsilon}{2}.$$

The length of the vector $\mathbf{g}$ is ε (see also the figure). Indeed, $\mathbf{g} = \sqrt{(\mathbf{e}_1 - \mathbf{e}_2)^2} = (2 - 2\cos\varepsilon)^{1/2} \approx \varepsilon$. From the almost orthogonality of the vectors $\mathbf{g}$ and $\mathbf{e}_2$ (or $\mathbf{g}$ and $\mathbf{e}_1$), simple expressions follow for the decomposition coefficients of the vector $\mathbf{a}$, i.e., we have for C_1 and $C_1 + C_2$

$$C_1\frac{(\mathbf{a}\cdot\mathbf{g})}{g^2} \approx a\cos\frac{\psi}{\varepsilon} = O\left(\frac{a}{\varepsilon}\right),$$
$$C_1 + C_2 = (\mathbf{a}\cdot\mathbf{e}_2) \approx a\sin\psi = O(a). \tag{5}$$

From expressions (5), we arrive at $C_1 \approx -C_2 \approx a\cos\frac{\psi}{\varepsilon} + O(a) \gg a$. Thus, we have formally confirmed the statement made above (which is evident from the figure) that the components of the vector $\mathbf{a}$ along the directions almost parallel to the basis vectors considerably exceed its length a.

ACKNOWLEDGMENTS

I am grateful to V.B. Levinski, V.L. Polyachenko, E.V. Polyachenko, A.V. Fridman, and S.M. Churilov, as their interest in the problem under discussion was a stimulus for the appearance of this paper.

REFERENCES

1. D. S. Henningson, L. N. Gustavsson, and K. S. Breuer, Appl. Sci. Res. **53**, 51 (1994).
2. F. Waleffe, Phys. Fluids **9**, 883 (1997).
3. S. A. Orszag, J. Fluid Mech. **50**, 689 (1971).
4. L. D. Landau and E. M. Lifshitz, *Fluid Mechanics*, 2nd ed. (Nauka, Moscow, 1986; Pergamon Press, Oxford, 1987).
5. S. C. Reddy, P. J. Schmid, J. S. Baggett, *et al.*, Fluid Mech. **365**, 269 (1988).
6. L. N. Trefethen, A. E. Trefethen, S. Reddy, *et al.*, Science **261**, 578 (1993).
7. K. M. Butler and B. F. Farrel, Phys. Fluids A **4**, 1637 (1992).
8. B. F. Farrel and P. J. Ioannou, Phys. Fluids A **5**, 1390 (1992).
9. B. F. Farrel, Phys. Fluids **31**, 2093 (1998).
10. P. Goldreich and D. Lynden-Bell, Mon. Not. R. Astron. Soc. **130** (2/3), 125 (1965).
11. A. M. Fridman, Pis'ma Astron. Zh. **15** (6), 1122 (1989) [Sov. Astron. Lett. **15** (6), 487 (1989)].
12. D. G. Lominadze, G. D. Chagelishvili, and R. G. Chanishvili, Pis'ma Astron. Zh. **14**, 856 (1988) [Sov. Astron. Lett. **14**, 364 (1988)].
13. W. M. Orr, Proc. R. Ir. Acad. (A) **27**, 9 (1907).
14. M. T. Landahl, J. Fluid Mech. **28**, 735 (1975).
15. T. Ellingsen and E. Palm, Phys. Fluids **18**, 487 (1975).

Translated by G. Merzon

Doklady Physics, Vol. 50, No. 6, 2005, pp. 311–314. Translated from Doklady Akademii Nauk, Vol. 402, No. 4, 2005, pp. 488–491.

MECHANICS

Vibrational Lift Force Acting on a Body in a Fluid Near a Solid Surface

A. A. Ivanova[1], V. G. Kozlov[2], and A. F. Kuzaev[1]

Presented by Academician G.G. Chernyĭ January 19, 2005

Received December 16, 2004

A free dense body in a vibrating cavity with an incompressible fluid executes vibrations under the action of an oscillating force. The hydrodynamic interaction of the vibrating body with the fluid creates a lift force, which depends strongly on the character of the vibration.

In the presence of the translational vibrations of the cavity, motion is induced in the fluid by body vibrations (in the absence of the body or when the densities of the body and fluid are equal to each other, the fluid is at rest in the cavity reference frame). High-frequency vibrations have traditionally been considered. In this case, the viscous boundary layer near the solid surface is negligibly narrow and viscosity can be disregarded when describing the vibrational motion of the fluid. The mean force appears due to the breaking of the symmetry of the pulsation velocity field and pressure field on the body surface. This scenario is realized when the body vibrates at a certain distance from the wall of the cavity (it is attracted to the wall) or near another body [1–3]. This interaction decreases rapidly when the distance increases.

Another mechanism is manifested in the case of combined, translational–rotational vibrations of the cavity, such as pendulum vibrations. Here, the rotational vibration component induces vibrations of the fluid with respect to the cavity that are not associated with the presence of the body, and the intense translational component generates synchronous vibrations of the body. In this case, the resulting lift force is manifested over the entire cavity volume and is so strong that it can ensure the flotation of the heavy body in the gravitational field [4, 5].

[1] *Perm State Pedagogical University, ul. Sibirskaya 24, Perm, 614990 Russia*
e-mail: a.ivanova@pspu.ac.ru

[2] *Institute of Continuous Media Mechanics, Ural Division, Russian Academy of Sciences, ul. Akademika Koroleva 1, Perm, 614013 Russia*
e-mail: kozlov@icmm.ru

The above problems refer to the high frequency limiting case. When the viscosity of the fluid is substantial, i.e., when the size of the body or the distance between bodies is comparable with the thickness of Stokes layers, the vibrational interaction between bodies becomes complicated and the direction of mean forces is often opposite, which is demonstrated in both physical experiments [5] and numerical calculations [6].

In this work, we carry out an experimental study on the lift force acting on the dense spherical body in the viscid incompressible fluid near the wall of the cavity that executes longitudinal vibrations.

Measurement of the vibrational lift force acting on a body is based on comparisons with the gravitational force: quasi-stationary suspended states are studied when the lift force is in balance with the weight of the body, more precisely, with its component perpendicular to the boundary. A procedure for reducing the effective action of the gravitational force is used [5]; i.e., the interaction of the body with the lateral wall of the cavity, which is inclined at a small angle α to the vertical line, is studied. The body vibrates along this wall, being continuously supported in the plane to which the wall is perpendicular. In the equilibrium suspended state, when the body does not touch the lateral wall, the vibrational force perpendicular to this wall is in balance with the tangent component of the gravitational force P_n. This component can vary over a wide range due to variation in the angle α. Using small angles, one can measure even weak vibrational forces under normal gravitational conditions.

A steel ball with a diameter of d = 5–9 mm (density ρ_S = 7.8 g/cm^3) is placed in a transparent rectangular Plexiglas $20 \times 40 \times 140$-mm cell with a water–glycerol solution (density is $\rho_L \sim 1.2$ g/cm^3 and viscosity varies in the range ν = 0.04–5.8 S). The cell executes back-and-forth vibrations with a frequency of f = 0–20 Hz and an amplitude of b = 5–25 mm. The frequency and amplitude are measured with an accuracy of 0.01 Hz and of no worse than 0.02 mm, respectively (the instability of frequency during an individual experiment does not exceed 0.2 Hz).

1028-3358/05/5006-0311$26.00

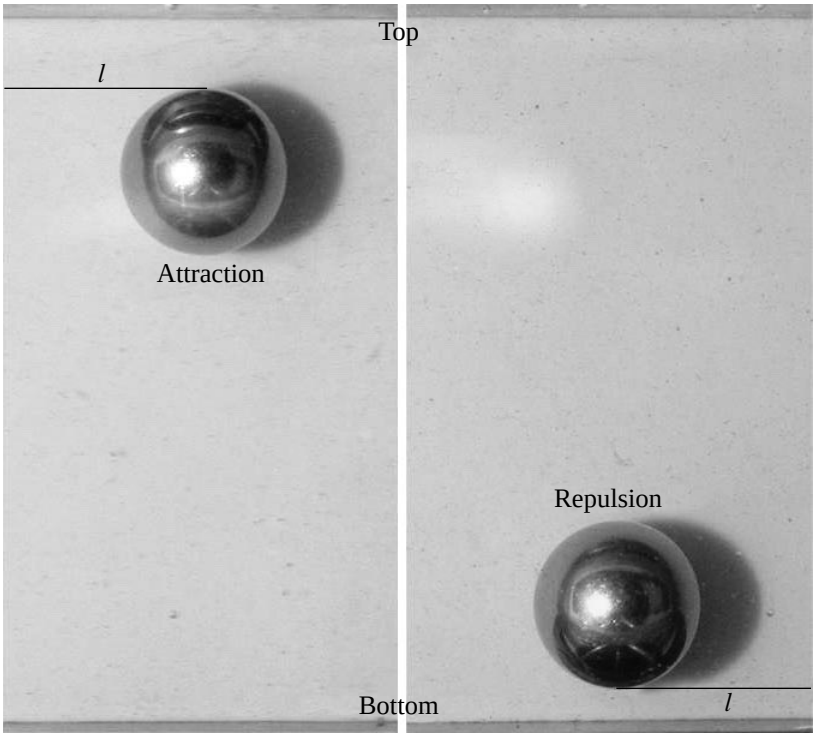

Fig. 1. Body position (d = 9.6 mm, ν = 0.5 S, α = 0.026 rad) in the quasi-stationary suspended state near the (left photo) top and (right photo) bottom of the layer for the same vibration parameters b = 17.2 mm and f = 11.2 Hz.

The vibration frequency increases (decreases) smoothly at a fixed angle α (in the range 0.05–0.3 rad) and a fixed amplitude b. At the critical frequency, the body is separated from the lateral wall (in the direction of the lift force), and a gap l appears between the body and wall. When the frequency decreases, the body returns to the initial state. The position and dynamics of the body are recorded by a video camera.

When vibrations are not intense, the body executes vibrations along the lateral wall, being in continuous contact with this wall and the cavity bottom. At the critical intensity of vibrations, the body is separated from the lateral wall and hovers at a certain distance l (see Fig. 1), executing vibrations and being supported only on the cavity bottom. This quasi-stationary state is stable. When the intensity of vibrations increases, the gap between the body and wall increases to the limiting value, which depends on the frequency of vibrations and viscosity of the fluid. The gap increases with the viscosity.

At high dimensionless frequencies, the body can also be in the quasi-equilibrium state near the top of the cavity but at larger distances (see Fig. 1). This behavior indicates that the vibrational repulsion force acting at a short distance is changed to the attraction force when the distance between the body and cavity increases.

In low-viscosity fluids, the separation of the body from the bottom occurs smoothly, the lifting height is low, and there is no hysteresis in the transitions. The critical frequency increases when the amplitude of vibrations decreases or the angle α increases.

In viscous fluids, the separation of the body from the surface is stepwise, and the body immediately rises at a finite distance l^*. The gap l increases with the frequency. When the frequency decreases, l decreases monotonically and the body continuously approaches the wall; however, it completes a stepwise return at the last instant (hysteresis is observed in the transitions).

An important parameter in vibrational hydromechanics is the dimensionless frequency $\omega = \frac{\Omega d^2}{\nu}$ ($\Omega \equiv 2\pi f$ is the angular frequency of the vibrations), which characterizes the ratio of the body size d to the Stokes boundary layer thickness $\delta = \sqrt{\frac{2\nu}{\Omega}}$. For high frequencies, the dynamics of the body is governed by the vibrational parameter $W = \frac{(b\Omega)^2}{gd}$ [4], which has the form $W = \frac{(b\Omega)^2}{dg\sin\alpha}$ [5] in the case of the reduced action of the gravitational force.

The force of the vibrational repulsion of the body from the cavity wall depends on ω. In the (ω, W) plane, the boundaries of the rise (vibration suspension) and fall of the body are shown by the closed and open

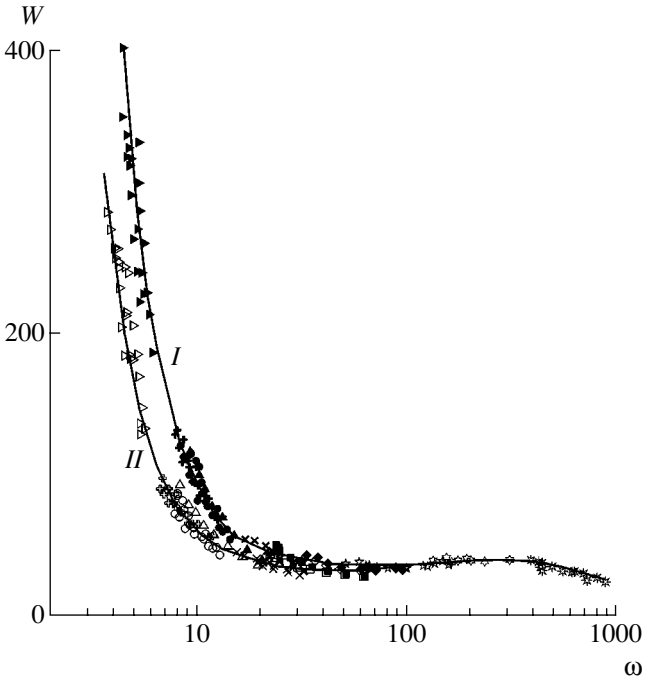

Fig. 2. Boundary of (*I*) the rise of the body and (*II*) the return to the initial state in the (ω, *W*) plane (α = 0.157 rad) for *d* = 9.2 mm and ν = (⊕) 5.6, (○) 4.6, (×) 1.6, (□) 1.1, (◇) 0.73, (☆) 0.46, (✡) 0.18, and (✳) 0.063 St and for *d* = 6.0 mm and ν = (▷) 5.8 and (△) 1.5 S. For ω > 100, the lines coincide with each other (closed points are omitted).

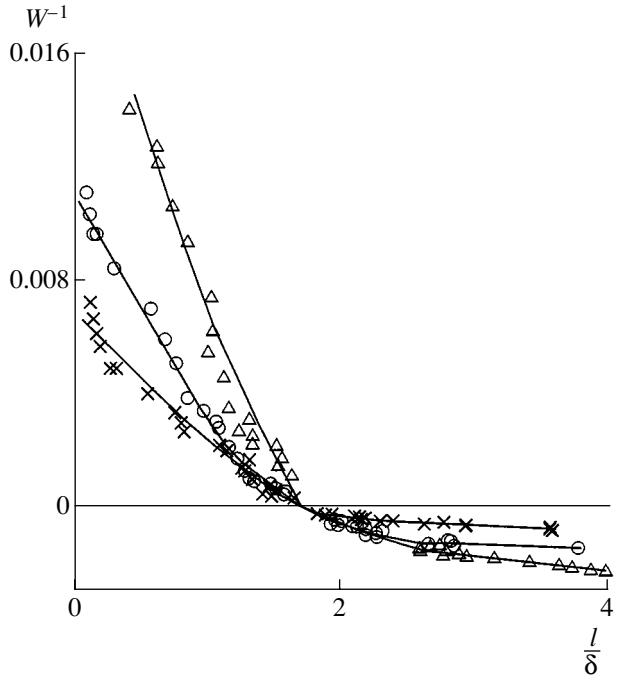

Fig. 3. Vibrational lift force W^{-1} vs. the dimensionless distance $\frac{l}{\delta}$ for moderate dimensionless frequencies (ω = 25–160, *b* = 17.9 mm, and ν = 0.20 S) for α = (×) 0.0051, (○) 0.0108, and (△) 0.03 rad.

points, respectively (see Fig. 2). The results that are obtained with fluids of various viscosities, with bodies of various sizes, and with various coefficients of the reduction of the gravitational force agree satisfactorily with each other (curves *I* and *II*). For frequencies ω < 100, the separation of the body from the wall when the vibration parameter increases, as well as the fall of the body when *W* decreases, occurs with hysteresis. For ω > 100, the boundaries *I* and *II* coincide with each other (open points are retained in the plot) and hysteresis is absent.

For low frequencies, the threshold value of the parameter *W* increases sharply when the frequency decreases. For ω < 10, the frequency dependence has the form $W^* \sim \omega^{-2}$.

Analysis shows that the repulsion force is manifested only at short distances comparable with the Stokes layer thickness. This conclusion is valid for the entire range of dimensionless frequencies under investigation.

For moderate frequencies, the vibrational lift force changes sign when the dimensionless distance $\frac{l}{\delta}$ between the body and wall increases (see Fig. 3). The parameter W^{-1} characterizes the vibrational lift force (with a dimension unit of $\rho_L b^2 \Omega^2 d^2$) disregarding the coefficient $\frac{(\rho_S - \rho_L)\pi}{6}$. Positive and negative W^{-1} values correspond to the repulsion force (rise of the body over the bottom of the vibrating cavity) and attraction to the top, respectively (see Fig. 1). The force vanishes at $\frac{l}{\delta} \approx 1.8$, which corresponds both to the maximum distance at which the body can rise over the bottom of the cavity and to the minimum distance at which the body can be attracted to the top. The separation of the curves is associated with different values of the dimensionless frequency ω.

The extreme right points in Fig. 3 correspond to the minimum in the interaction curves. With a further increase in the distance, the attraction force decreases (in these sections of the curves, the equilibrium of the body is instable), which agrees with the theory of the interaction of a vibrating body under the conditions of potential flow for $\omega \gg 1$ [1–3].

For low frequencies ω < 10, when $W^* \sim \omega^{-2}$, the vibrational lift force is characterized by the product $W^{-1}\omega^{-2}$, and the role of the Stokes boundary layer continues to be decisive. In the $(\frac{l}{\delta}, W^{-1}\omega^{-2})$ plane (see Fig. 4), all points corresponding to the suspension of the body over the bottom of the cavity agree with each

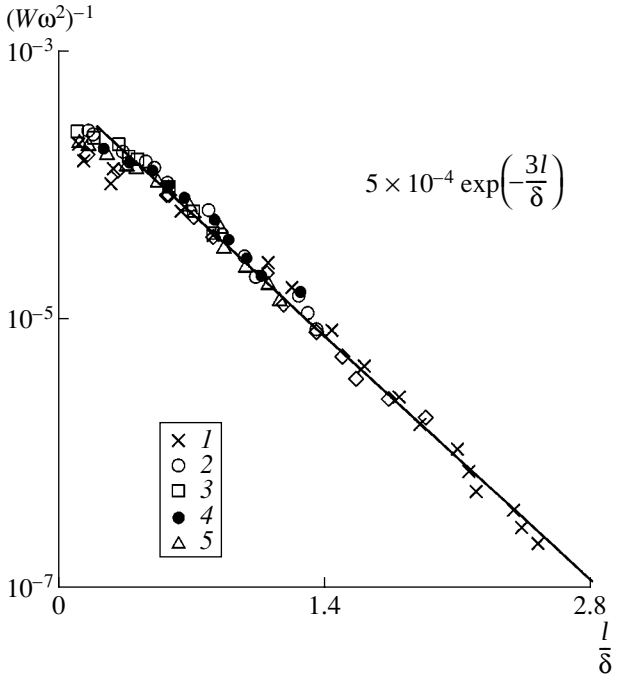

Fig. 4. Vibrational interaction curve in the $(\frac{l}{\delta}, W^{-1}\omega^{-2})$ plane for low frequencies ($\omega < 10$, (*1–3*) $b = 24.7$ mm, and α = (*1*) 0.005, (*2*) 0.204, and (*3*) 0.307 rad, (*4*) $b = 19.2$ mm and $\alpha = 0.234$ rad, and (*5*) $b = 11.8$ mm and $\alpha = 0.078$ rad.

other. For $\frac{l}{\delta} > 0.2$, the repulsion force decreases exponentially when the distance increases, $W^{-1}\omega^{-2} \sim \exp\left(-\frac{3l}{\delta}\right)$. The attraction force is not manifested for low frequencies.

The vibrational repulsion force, which can raise a heavy spherical particle in the static gravitational field, is generated by the viscous interaction of the body with the walls of the cavity. This force is manifested when the gap width is comparable to the Stokes layer thickness, and it decreases monotonically when the distance increases.

For low frequencies, the results are qualitatively consistent with those obtained in [7], where a repulsion force also acts on a particle moving uniformly parallel to a planar surface. In the case analyzed in [7], as the distance increases, the force decreases rapidly beyond the radius of the viscous interaction between the particle and wall (in our case, the Stokes layer thickness serves as this radius). Moreover, this force is proportional to the velocity squared of the body. The latter dependence is consistent with the controlling parameter $W^{-1}\omega^{-2}$ that is found in the experiment and characterizes the vibrational lift force in the low-frequency region, where the role of viscous forces is decisive and the velocity of the vibrational motion of the body is proportional to $b\Omega\omega$.

Thus, the vibrational repulsion of a solid spherical body that vibrates in an incompressible viscous fluid from the wall of the cavity has been experimentally detected and analyzed in this work. It has been shown that the repulsion force is generated by the viscous interaction of the body with the wall and that it is manifested over the entire range of dimensionless frequencies at distances comparable with the Stokes-layer thickness. For high frequencies beyond the viscous interaction region, the repulsion force is changed to the attraction force at distances $\frac{l}{\delta} > 2$.

For low frequencies $\omega < 10$, the vibrational repulsion force is characterized by the dimensionless parameter $W^{-1}\omega^{-2}$ and it depends exponentially on the distance, $W^{-1}\omega^{-2} \sim \exp\left(-\frac{3l}{\delta}\right)$. The boundary of the vibrational suspension of a heavy sphere in a static force field is determined as a function of the dimensionless frequency.

ACKNOWLEDGMENTS

This work was supported by the Russian Foundation for Basic Research (project no. Ural 04-01-96055).

REFERENCES

1. H. Lamb, *Hydrodynamics*, 6th ed. (Cambridge Univ. Press, Cambridge, 1932; Gostekhizdat, Moscow, 1947).
2. B. A. Lugovtsov and V. L. Sennitskiĭ, Dokl. Akad. Nauk SSSR **289** (2), 314 (1986) [Sov. Phys. Dokl. **31**, 530 (1986)].
3. D. V. Lyubimov, T. P. Lyubimova, and A. A. Cherepanov, *Convective Flows* (Perm. Ped. Inst., Perm, 1987) [in Russian].
4. V. G. Kozlov, Europhys. Lett. **36**, 651 (1996).
5. A. A. Ivanova and V. G. Kozlov, Izv. Akad. Nauk, Ser. Mekh. Zhidk. Gaza, No. 5, 35 (2001) [Fluid Dyn. Res. **36**, 701 (2001)].
6. S. S. Tabakova and Z. D. Zapruanov, ZAMP **33**, 344 (1982).
7. P. Vasseur and R. G. Cox, J. Fluid Mech. **80**, 561 (1977).

Translated by R. Tyapaev

Doklady Physics, Vol. 50, No. 6, 2005, pp. 315–319. Translated from Doklady Akademii Nauk, Vol. 402, No. 5, 2005, pp. 617–622.

MECHANICS

Model of the Deformation and Fracture of a Metal Ceramic Based on $TiB_2 + B_4C$ upon Dynamic Loading

N. N. Belov, N. T. Yugov, S. A. Afanas'eva, A. N. Tabachenko, A. A. Konyaev, V. F. Tolkachev, and A. A. Yugov

Presented by Academician N.F. Morozov December 3, 2004

Received December 3, 2004

In the case of high-speed collisions, ceramic materials based on refractory compounds are brittle and unreliable. A promising direction for improving the physical–mechanical characteristics of ceramics operating at high pressures and temperatures is the introduction of an efficient metal matrix into their content. A reliable tool for designing materials with a given directivity of properties is a computational–experimental method based on the mathematical simulation of shock wave processes and experiments. A mathematical model describing the deformation and fracture of a metal ceramic based on titanium diboride and bore carbide ($TiB_2 + B_4C$) with a metal matrix upon dynamic loading is proposed in this work.

The metal ceramic based on $TiB_2 + B_4C$ with a metal matrix was obtained using the method of self-propagating high-temperature synthesis. Figure 1 shows the microstructure of this metal ceramic. Against the background of the bright metallic component, large dark B_4C fragments and small TiB_2 particles (whose sizes are smaller by an order of magnitude) are seen. Table 1 presents certain physical–mechanical characteristics of the metal ceramic based on $TiB_2 + B_4C$ for various fractions of the metal matrix. In Table 1, C_l and C_t are the velocities of longitudinal and transverse waves, respectively; c_0 is the volume speed of sound; K is the volume-compression modulus; μ_0 is the shear modulus; and ν is Poisson's ratio.

The fundamental advantage of this metal ceramic over the single-phase high-strength ceramics that constitute its components is its increased crack fracture toughness. Moreover, this metal ceramic is very hard, and it possesses high refractoriness, comparatively low density, and high wear resistance. The introduction of the metal matrix makes the material more plastic and viscous and prevents the growth of cracks upon compression and particularly upon tension, when fracture occurs primarily along grain boundaries.

The metal ceramic based on $TiB_2 + B_4C$ is characterized by high impact-protective properties. Figure 2 shows the x-ray patterns of the piercing of (left) an aluminum plate by a steel projectile 5.8 mm in diameter and 3.5 g in mass with an ogival head at an impact velocity of 763 m/s and of (right) a metal ceramic plate based on $TiB_2 + B_4C$ by the same projectile with a velocity of 766 m/s. The fracture of the aluminum plate upon penetration of the projectile occurs as a puncture, and the projectile remains undeformed. The residual velocity is equal to 724 m/s. When piercing the metal ceramic plate, a semispherical dome is formed from the fractured metal ceramic, and the plate holds integrity beyond the contact zone. The projectile wears intensely upon interaction, and its residual assumes a mushroom-like shape. The residual velocity is equal to 552 m/s. Thus, the metal ceramic plate provides higher resistance against penetration of the projectile than the aluminum plate.

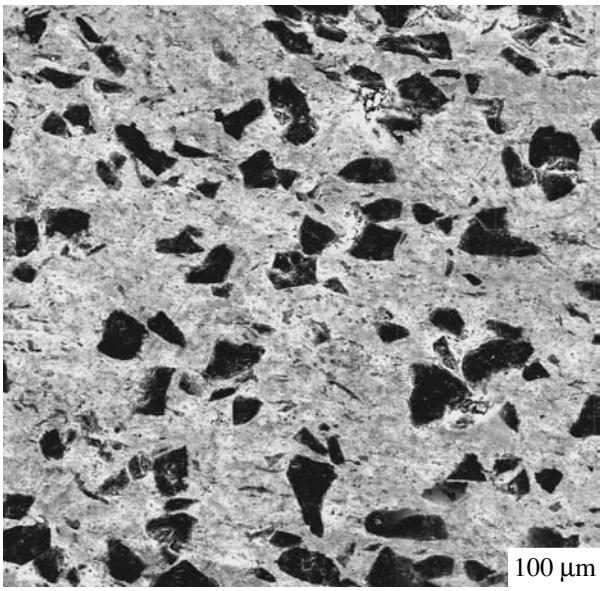

Fig. 1. Microstructure of the metal ceramic based on $TiB_2 + B_4C$.

Tomsk State University, Tomsk, 634050 Russia
e-mail: svetl@niipmm.tsu.ru

1028-3358/05/5006-0315$26.00

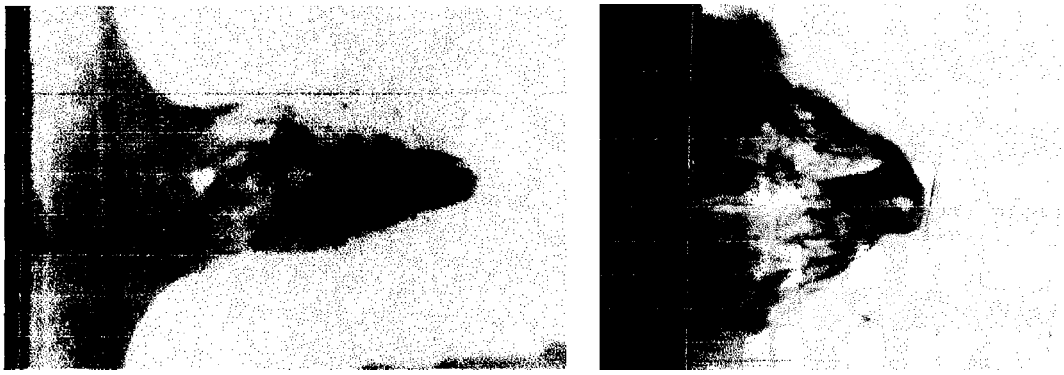

Fig. 2. Piercing of the (left panel) aluminum and (right panel) metal ceramic plates by a steel projectile.

When the shock wave propagates in the metal ceramic, a pronounced elastic sighting is not observed, which indirectly testifies to the presence of a viscous component [1]. The fracture of the metal ceramic in the shock wave occurs through the shear mechanism in brittle components.

To calculate the stress–strain state and fracture of the metal ceramic based on $TiB_2 + B_4C$ upon dynamic loading, we propose a generalization of the model of porous high-strength ceramic [2] to this material. The necessary characteristics of this model as applied to the TiB_2 and B_4C ceramics were obtained using experimental data [3].

The metal ceramic based on $TiB_2 + B_4C$ is treated as a homogeneous three-phase mixture with an initial density of

$$\rho_0 = \nu_1\rho_{01} + \nu_2\rho_{02} + \nu_3\rho_{03},$$

where ρ_{0i} and ν_i are, respectively, the initial densities and volume concentrations ($\nu_1 + \nu_2 + \nu = 1$) of ($i = 1$) TiB_2, ($i = 2$) B_4C, and ($i = 3$) the metallic component. In the model of the porous elastoplastic medium, the metal ceramic is considered as a two-component material consisting of the solid phase, matrix with the initial density ρ_0, and inclusions, including pores with a characteristic size of a_0. The specific volume v of the porous medium is represented as the sum $v = v_m + v_p + v_c$, where v_m, v_p, and v_c are the specific volumes of the matrix material, pores, and cracks, respectively. The porosity of the material is characterized by the relative volume of cavities $\xi = \xi_p + \xi_c$, where $\xi_p = \frac{v_p}{v}$ and $\xi_c = \frac{v_c}{v}$ are the relative volumes of pores and cracks, respectively, or by the parameter $\alpha = \frac{v}{v_m} = \frac{1}{1-\xi}$.

Table 1

ρ_0, g/cm^3	C_l, km/s	C_t, km/s	c_0, km/s	K, GPa	μ_0, GPa	ν
3.18	10.5	5.81	8.13	204	104	0.28
3.5	10.5	6.89	6.9	167	166	0.12
3.8	11.1	7.82	6.5	160	160	–

The system of equations describing the behavior of the porous elastoplastic medium has the form

$$\frac{d}{dt}\int_V \rho\, dV = 0, \quad \frac{d}{dt}\int_V \rho\mathbf{u}\, dV = \int_S \mathbf{n}\cdot\boldsymbol{\sigma}\, dS,$$

$$\frac{d}{dt}\int_V \rho E dV = \int_S \mathbf{n}\cdot\boldsymbol{\sigma}\cdot\mathbf{u}\, dS,$$

$$\mathbf{e} = \frac{\mathbf{s}^J}{2\mu} + \lambda\mathbf{s}, \quad \mathbf{s}:\mathbf{s} = \frac{2}{3}\sigma_T^2.$$

Here, t is time; V is the integration volume; S is the integration surface; $\mathbf{n}$ is the outward normal unit vector; ρ is the density; $\boldsymbol{\sigma} = -p\mathbf{g} + \mathbf{s}$ is the stress tensor; $\mathbf{s}$ is its deviator; p is the pressure; $\mathbf{g}$ is the metric tensor; $\mathbf{u}$ is the velocity; $E = \varepsilon + \mathbf{u}\cdot\frac{\mathbf{u}}{2}$ is the specific total energy; ε is the specific internal energy; $\mathbf{e} = \mathbf{d} - (\mathbf{d}:\mathbf{g})\frac{\mathbf{g}}{3}$ is the deviator of the strain rate tensor; $\mathbf{d} = \frac{1}{2}(\nabla\mathbf{u} + \nabla\mathbf{u}^T)$ is the strain rate tensor; $\mathbf{s}^J = \dot{\mathbf{s}} + \mathbf{s}\cdot\boldsymbol{\omega} - \boldsymbol{\omega}\cdot\mathbf{s}$ is the Jaumann–Noll derivative of the stress-tensor deviator; $\boldsymbol{\omega} = \frac{\nabla\mathbf{u}^T - \nabla\mathbf{u}}{2}$ is the vortex tensor;

$$\mu = \mu_0(1-\xi)\left[1 - \frac{(6\rho_0 c_0^2 + 12\mu_0)\xi}{9\rho_0 c_0^2 + 8\mu_0}\right]$$

is the effective shear modulus; $\sigma_T = \frac{Y_0}{\alpha} + kp$ is the yield strength; and ρ_0, c_0, μ_0, Y_0, and k are the constants of the matrix material.

The parameter λ is excluded using the yield condition. The equation of state for the porous material is written in the form

$$p = \frac{\rho_0}{\alpha}\left[\gamma_0\varepsilon + \frac{c_0^2\left(1-\frac{\gamma_0\eta}{2}\right)\eta}{(1-S_0\eta)^2}\right],$$

where $\eta = 1 - \frac{\rho_0 v}{\alpha}$ and

$$\gamma_0 = \frac{v_{m0}}{\sum_{i=1}^{3}\frac{m_i}{\rho_{0i}\gamma_{0i}}}$$

is the Grüneisen parameter of the matrix material, where γ_{0i} are the coefficients of the components of the metal ceramic and $m_i = \frac{\nu_i\rho_{0i}}{\rho_0}$ are the mass concentrations ($m_1 + m_2 + m_3 = 1$).

If the dependence of the shock wave velocity D on the mass velocity u in the case of a one-dimensional deformed state of matrix material, $D = c_0 + S_0u$, the coefficients c_0 and S_0 of the linear dependence are determined in terms of the shock adiabatic relations for the components of the metal ceramic, $D_i = c_{0i} + S_{0i}u_i$. This occurs as follows: In terms of the specific volume v_m and pressure p_m (subscript "m" refers to the parameters of the matrix material), the shock adiabatic relation of the mixture has the form

$$v_m(p_m) = \sum_{i=1}^{3} m_i\left\{v_{0i} - \frac{1}{p_m}\left[\frac{c_{0i}}{S_{0i}}\left(\sqrt{\frac{p_m}{\rho_{0i}c_{0i}^2} + \frac{1}{4}} - \frac{1}{2}\right)\right]^2\right\}.$$

From the following relations on the shock wave for the mixture:

$$D = v_{m0}\sqrt{\frac{p_m}{v_{m0} - v_m(p_m)}}, \quad u = \sqrt{p_m(v_{m0} - v_m(p_m))},$$

where $v_{m0} = \frac{1}{\rho_0}$, the shock wave velocity is found as a function of the mass velocity. From this dependence, the coefficients c_0 and S_0 are then determined. Table 2 presents the parameters of the equation of state for the TiB_2 and B_4C ceramics and for the metal ceramic based on $TiB_2 + B_4C$.

The metal ceramic is broken due primarily to the growth of microcracks. The maximum elastic half-opening of a coin-like crack under the tensile stress that is perpendicular to the crack plane is determined from the relation [4]

Table 2

Material	ρ_0, g/cm^3	c_0, cm/μs	S_0	γ_0
TiB_2	4.51	0.9	0.75	1.5
B_4C	2.52	0.93	1.44	1.5
$TiB_2 + B_4C$ + metal	3.494	0.71	1.32	1.5

$$\delta = -\frac{2(1-\nu)}{\pi\mu_0}Rp_m,$$

where ν is Poisson's ratio, R is the crack radius, and $p_m = \alpha p$ is the pressure in the matrix material. When the crack opens, its faces form an ellipsoid of revolution with the semiaxes δ, R, and R. The crack volume is determined by the expression

$$V_T = -\frac{8(1-\nu)}{3\mu_0}R^3\alpha p.$$

Therefore,

$$\xi_c = -\frac{8(1-\nu)}{3\mu_0}N_0R^3\alpha p,$$

where N_0 is the number of cracks per unit volume. Assuming that the volume of pores remains equal to ξ_0 up to the time at which the material damaged with cracks undergoes fragmentation, we obtain

$$\xi_c = \xi - \xi_0 = \frac{\alpha - \alpha_0}{\alpha_0\alpha}.$$

In this case, the pressure in the material is determined as

$$p = -\frac{3\mu_0(\alpha - \alpha_0)}{8(1-\nu)N_0\alpha_0R^3\alpha^2}.$$

Therefore, discontinuities grow more freely as the crack radius increases.

The growth of cracks is determined by the equation $\frac{\dot{R}}{R} = F_1 + F_2$. Here,

$$F_1 = \begin{cases}\frac{\alpha s_i - s_*}{\eta_1} & \text{for } \alpha s_i > s_*,\\ 0 & \text{for } \alpha s_i \le s_*;\end{cases}$$

$$F_2 = \begin{cases}\frac{|\alpha p| - p_*}{\eta_2} & \text{for } p < 0 \wedge |\alpha p| > p_*,\\ 0 & \text{for } p \ge 0 \vee |\alpha p| \le p_*;\end{cases}$$

Table 3

Parameter	TiB_2	B_4C	$TiB_2 + B_4C$ + metal
ρ_0, g/cm^3	4.51	2.52	3.494
μ_0, GPa	210.0	182.0	166.0
N	0.28	0.17	0.12
R_0, μm	2.5	2.5	2.5
R_*, μm	11.6	11.6	11.6
N_0, 10^7, cm^{-3}	64.0	64.0	64.0
η_1, GPa μs	0.75	0.7	1.6
η_2, GPa μs	0.5	0.5	0.7
p_0, GPa	0.5	1.8	1.22
S_0, GPa	5.0	6.0	5.0
α_0	1.0006	1.0006	1.0006

where

$$s_i = \sqrt{\frac{3}{2}\mathbf{s} : \mathbf{s}}; \quad s_* = s_{01}\left(1 - \frac{R}{R_*}\right);$$

$$p_* = p_0\left(1 - \frac{R}{R_*}\right); \quad R_* = \frac{\beta}{\sqrt[3]{N_0}};$$

and s_{01}, p_0, η_1, η_2, and β are the constants of the material. The equality $R = R_*$ is a criterion for the complete fragmentation of the material. Under this condition, the material assumes the properties of a granulated medium, which carries compressing and shear stresses but does not hold tensile forces.

The shock wave compaction of the fractured metal ceramic is calculated using the equation

$$Y_0\tau^2 Q(\alpha, \dot\alpha, \ddot\alpha) = \alpha p + \frac{Y_0}{k}\left[1 - \left(\frac{\alpha}{\alpha - 1}\right)^{\frac{2k}{3-2k}}\right],$$

$$\tau^2 = \frac{\rho_0 a_0^2}{3(\alpha_0 - 1)^{2/3} Y_0},$$

$$Q(\alpha, \dot\alpha, \ddot\alpha) = \frac{3-2k}{3+4k}\frac{\ddot\alpha}{\alpha^{1/3}}\left[1 - \left(\frac{\alpha}{\alpha - 1}\right)^{\frac{3+4k}{3(3-2k)}}\right]$$

$$-\frac{3-2k}{3(6-k)}\frac{\dot\alpha^2}{\alpha^{4/3}}\left[1 - \left(\frac{\alpha}{\alpha - 1}\right)^{\frac{2(6-k)}{3(3-2k)}}\right],$$

where coefficients Y_0 and k of the Mohr–Coulomb condition are determined by comparing the theoretical and experimental adiabatic relations. The fractured material upon tension is described as a medium free of stresses. In this case, the relative concentration of cavities is determined from the equation of state for the material with zero pressure in particles. Table 3 presents the constant for the model of the fracture of TiB_2, B_4C, and of the metal ceramic based on $TiB_2 + B_4C$. The yield strength of the metal ceramic is taken as the maximum of the yield strengths of its components.

Using the above model, we solve the problem of the penetration of a projectile made of the metal ceramic based on $TiB_2 + B_4C$ into a semi-infinite aluminum target. The parallelepiped-shaped projectile with a height of l_0 = 30 mm and a square base with a side of d_0 = 9.3 mm normally falls with a velocity of 870 m/s onto the semi-infinite aluminum plate. Figure 3 shows the calculation results for the sections of isometric projections of the colliding bodies for various times. The photograph of a crater that was formed upon impact in an experiment specially carried out with the same initial conditions is also shown. To calculate the behavior of the fractured material, the algorithm of the rearrangement of the calculation grid was applied [5]. Particles of the fractured material were simulated by the site elements of an elementary tetrahedron that had mass and velocity and obeyed the laws of conservation of mass and angular momentum. Particles are not presented in the figure, as graphical visualization is complicated.

As a result of the impact by the metal ceramic projectile, a cone-like crater with a depth of 40 mm is formed in the aluminum plate. The height of the undestroyed projectile fragment was equal to 10 mm. Small pressed particles of the metal ceramic lie under this fragment at the crater bottom.

The calculation of the penetration of the projectile into the aluminum plate reveals the following processes. At the beginning of the interaction, shock waves, whose maximum amplitude reaches 8 GPa to 4 μs, propagate in the colliding bodies from the contact boundary. The propagation of compression waves in the projectile is accompanied by the intense growth of cracks. In this case, the region where cracks reach the critical value takes approximately 3/4 of the projectile height to the sixth μs. In this time range, owing to unload propagating from the free surfaces of the projectile and target, the tensile stress region is formed in the projectile near the contact surface. In this region, the projectile decays into two fragments. Beginning with the 24th μs, both these fragments and particles of the fractured projectile material are involved in the interaction. When penetrating, the part of the fractured material is displaced in a radial direction and acts on the target material, which leads to the formation of a conic crater. At the 280th μs, the projectile velocity becomes equal to zero, and the interaction process ends. The differences between the calculation and experiment in terms of the residual length of projectile, crater depth,

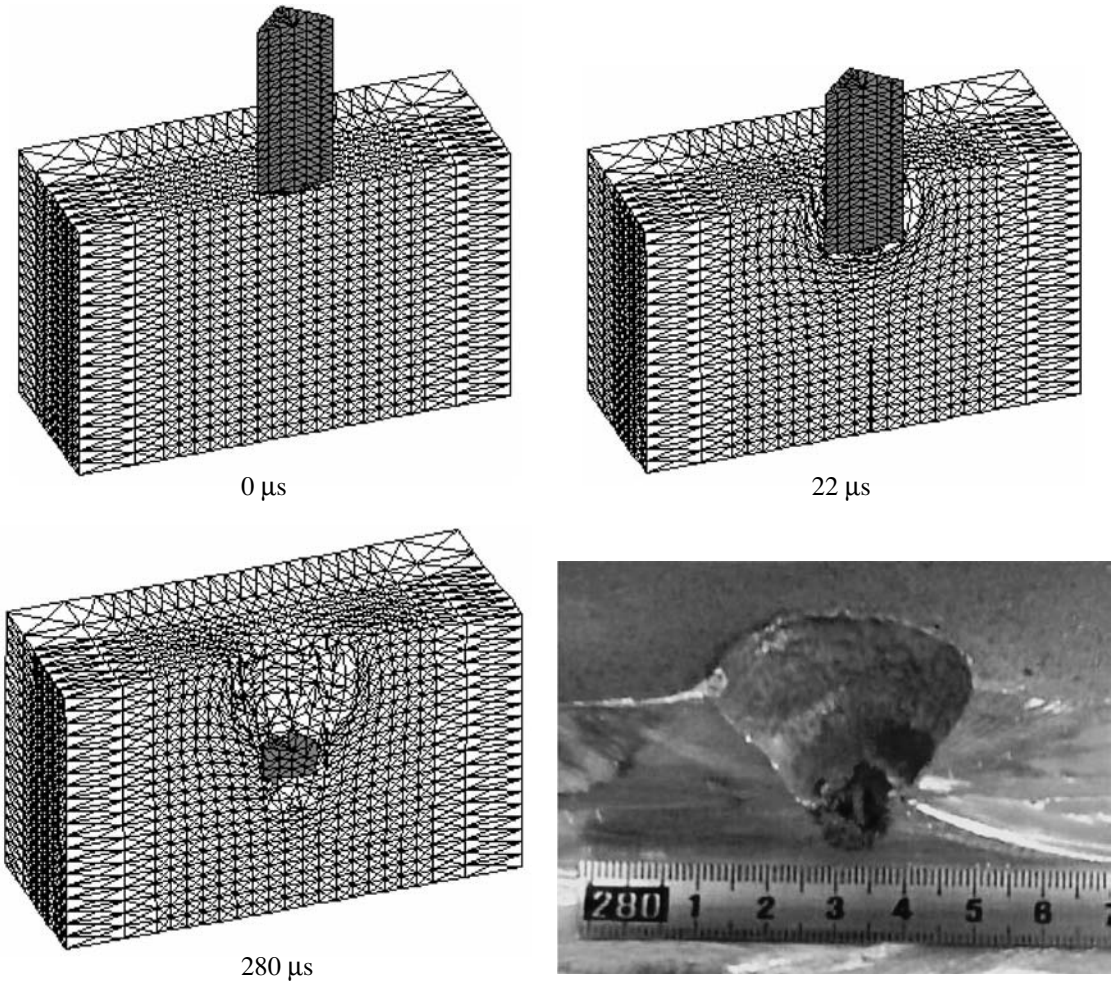

Fig. 3. Chronogram of the penetration of the metal ceramic projectile into the aluminum target and crater photograph.

and input crater diameter are equal to 8, 3, and 30%, respectively.

ACKNOWLEDGMENTS

This work was supported by the Ministry of Education of the Russian Federation (project no. E02-4-198) and the Russian Foundation for Basic Research (project no. 04-01-00856).

REFERENCES

1. G. I. Kanel', S. V. Razorenov, A. V. Utkin, and V. E. Fortov, *Shock-Wave Phenomena in Condensed Media* (Yanus-K, Moscow, 1996) [in Russian].
2. S. A. Afanas'eva, N. N. Belov, V. F. Tolkachev, *et al.*, Dokl. Akad. Nauk **368** (4), 477 (1999) [Dokl. Phys. **44**, 683 (1999)].
3. A. David, Int. J. Impact Eng. **1** (14), 491 (1993).
4. L. Seaman, D. R. Gurran, and D. A. Shockey, J. Appl. Phys. **47** (11), 4814 (1976).
5. N. T. Yugov, N. N. Belov, and S. V. Pan'ko, *Application of the Finite Element Method to Study High-Speed Interaction of Deformable Solids* (Izd. Tomsk. Univ., Tomsk, 2000) [in Russian].

Translated by R. Tyapaev

Doklady Physics, Vol. 50, No. 6, 2005, pp. 320–323. Translated from Doklady Akademii Nauk, Vol. 402, No. 5, 2005, pp. 623–626.

MECHANICS

Solution Nonuniqueness for the Problem of Salt Precipitation Due to the Evaporation of Ground Water

G. G. Tsypkin

Presented by Academician D.M. Klimov December 30, 2004

Received January 30, 2005

1. Processes of salt precipitation that occur when fluids flow through a permeable soil are of great interest for oil and gas extraction problems, soil science, geothermal reservoir engineering, ecology, etc. [1–4]. The precipitate occupies a certain part of the porous space, hampers mass transfer, and significantly changes porosity and permeability. Observations show that this circumstance sometimes causes the formation of impermeable layers, where salt in the solid form completely occupies the porous space. From the practical point of view, the main goal is to define the critical conditions under which certain properties of the porous medium are qualitatively changed.

A mathematical model of salt precipitation due to the evaporation of ground water was presented in [5, 6]. It was found that the mass of precipitate depends on both the front velocity and the rate of advective salt transport towards the front. Numerical experiments have shown that the mass of the precipitate increases sharply in a certain region of parameters, but the critical parameters that correspond to porous space clogging have not been determined.

The purpose of this work is to explore the processes of salt precipitation in the region of critical parameters and porous space clogging due to the evaporation of ground water, which contains salt in the dissolved form. Analysis of the one-dimensional flow shows that the solution of the problem is nonunique. Transition from the salt accumulation regime to the salt precipitation regime is accompanied by the formation of a second solution, which has no physical meaning. The first solution satisfies the criterion of the transition to the unique solution for the salt accumulation problem. If the mass of precipitate increases due to variation in parameters, these two solutions approach each other. When the parameters reach certain critical values, two branches of the solutions converge and coincide with each other. In the region above these critical values, the solution of the problem does not exist at all. From the physical point of view, the coincidence of the branches corresponds to the porous space that is being clogged with salt.

2. Let us consider soil that was initially saturated with saline water. If air humidity near the ground surface is less than the saturation value, ground water evaporates and a region that is saturated with air-vapor mixture is formed. As a result, the salt concentration increases ahead of the evaporation front. For the sake of simplicity, we assume that the velocity of water and air humidity are known parameters [5].

In the region behind the front, the vapor diffusion equation and the Clapeyron equation of state have the form

$$\frac{\partial \nu}{\partial t} - \mathrm{div} D_v \mathrm{grad} \nu = 0,$$
$$P_v = \rho_v R_v T, \quad P = \rho_a R_a T, \quad \nu = \frac{R_a P_v}{R_v P_a}. \tag{1}$$

Ahead of the front, the salt concentration is determined by the diffusion equation

$$m\frac{\partial c}{\partial t} + \mathbf{v} \cdot \mathrm{grad} c - \mathrm{div} D_c \mathrm{grad} c = 0. \tag{2}$$

If the filtration velocity is low, the heat conduction equation

$$\frac{\partial T}{\partial t} = a_{1,2} \Delta T \tag{3}$$

is valid in both regions. Here, v is the velocity, m is the porosity, ν is the humidity, P is the pressure, D is the diffusion coefficient, R is the gas constant, ρ is the density, c is the salt concentration, T is the temperature, and a is the thermal diffusivity. The subscripts a, v, and c refer to the properties of air, vapor, and salt, respectively; and the subscripts 1 and 2 refer to the regions saturated with saline water and air–vapor mixture, respectively.

We assume that all phases are in local thermodynamic equilibrium and the evaporation pressure is a

Institute for Problems in Mechanics,
Russian Academy of Sciences,
pr. Vernadskogo 101, Moscow, 119526 Russia
e-mail: tsypkin@ipmnet.ru

1028-3358/05/5006-0320$26.00

function of the evaporation temperature and salt concentration

$$T_+ = T_- = T_*, \quad P_{v*} = F(T_* - \alpha c_*),$$
$$\nu = \frac{R_a P_{v*}}{R_v P_a}, \tag{4}$$

where the function F is defined as [7]

$$F(x) = 10^5 \exp\left[-7226.6\left(\frac{1}{x} - \frac{1}{373.16}\right) + 8.2\ln\frac{373.16}{x} - 0.0057(373.16 - x)\right].$$

Here, α is the coefficient that changes evaporation temperature due to salt concentration and $c_* = c_s(T_*)$, where $c_s(T)$ is the known salt solubility function. The subscripts plus (+) and minus (–) refer to the parameters ahead of the front and behind the font, respectively, and asterisk corresponds to the values at the front.

The laws of conservation of the masses of H_2O and salt have the form

$$\left[\frac{\rho_w}{\rho_a} - \left(1 - \frac{m_c}{m_0}\right)\frac{\rho_{v*}}{\rho_a}\right]V_n = D_v\left(1 - \frac{m_c}{m_0}\right)(\mathrm{grad}\nu)_{n2}, \tag{5}$$

$$\left(c_* - \frac{m_c\rho_c}{m_0\rho_w}\right)V_n - \frac{c_*}{m_0}\nu_{n1} + D_c(\mathrm{grad}c)_{n1} = 0. \tag{6}$$

It was shown in [8] that energy absorption at the front due to evaporation is negligible compared to the advective heat transfer. As a result, the energy balance at the front takes the form

$$(\lambda \mathrm{grad}T)_{n1} = (\lambda \mathrm{grad}T)_{n2}. \tag{7}$$

Here, m_0 is the initial porosity, m_c is the fracture of porous space saturated with precipitate, V is the velocity of the evaporation front, λ is the heat conductivity, and the subscript n denotes the normal component.

The initial and boundary conditions have the form

$$t = 0: \quad T = T_0, \quad c = c_0;$$
$$z = 0: \quad \nu = \nu_a, \quad T = T_a. \tag{8}$$

3. Let us consider the motion of the front from the flat ground surface $z = 0$ in the positive z direction under constant initial and boundary conditions for a given flow rate $v = \frac{U}{\sqrt{t}}$, where U = const. The problem admits the similarity solution

$$T = T(\zeta), \quad \nu = \nu(\zeta), \quad c = c(\zeta),$$
$$\zeta = \frac{z}{2\sqrt{D_c t}}, \quad Z(t) = 2\gamma\sqrt{D_c t}, \quad V = \frac{dZ}{dt}.$$

Solutions in each region are expressed in terms of error functions. These solutions are substituted into boundary conditions (5)–(8), which, together with relation (4), lead to the system of transcendental equations. The system was solved in [5] by using the Newton method. The roots of the system were easily computed with a given accuracy for the parameters that differ strongly from certain critical values. When the parameters approach their critical values, the accuracy decreases and eventually the method ceases to work altogether.

Analysis shows that the system can be transformed to a single equation for the velocity of an unknown front. We utilize this circumstance to graphically trace the evolution of the transcendental curve in order to understand what happens when the parameters are close to their critical values.

The transcendental equation for the unknown parameter γ has the form

$$G \equiv \nu_* \frac{R_v}{R_a} - \frac{F(T_* - \alpha c_s)}{P_a} = 0, \tag{9}$$

where unknown values ν_*, T_*, and m_c depend on γ and may be written as

$$m_c(\gamma) = m_0\frac{\rho_w}{\rho_{salt}}\left[c_s(T_*(\gamma))\left(1 + \frac{U}{\gamma}\right) - \frac{c_s(T_*(\gamma)) - c_0}{\sqrt{\pi}}\frac{\exp(-(\gamma + U)^2)}{\gamma \mathrm{erfc}(\gamma + U)}\right],$$

$$\nu_*(\gamma) = \nu_a\frac{A_1(\gamma)}{\sqrt{\pi}\gamma + A_1(\gamma)} + \frac{\sqrt{\pi}\rho_w m_0(\gamma + U)}{\rho_a(m_0 - m_c(\gamma))[\sqrt{\pi}\gamma + A_1(\gamma)]},$$

$$T_*(\gamma) = T_0\frac{A_2(\gamma) + c_1 A_3(\gamma)}{c_2 A_3(\gamma) + A_2(\gamma)}, \quad c_1 = \frac{\lambda_2\sqrt{a_1}}{\lambda_1\sqrt{a_2}},$$

$$c_2 = \frac{\lambda_2\sqrt{a_1}}{\lambda_1\sqrt{a_2}}\frac{T_a}{T_0},$$

$$A_1(\gamma) = \frac{\exp\left(-(\gamma + U)^2\frac{D_c}{D_v}\right)}{\mathrm{erf}\left((\gamma + U)\sqrt{\frac{D_c}{D_v}}\right)},$$

$$A_2(\gamma) = \frac{\exp\left(-(\gamma + U)^2\frac{D_c}{a_1}\right)}{\mathrm{erfc}\left((\gamma + U)\sqrt{\frac{D_c}{a_1}}\right)},$$

$$A_3(\gamma) = \frac{\exp\left(-(\gamma + U)^2\frac{D_c}{a_2}\right)}{\mathrm{erf}\left((\gamma + U)\sqrt{\frac{D_c}{a_2}}\right)}.$$

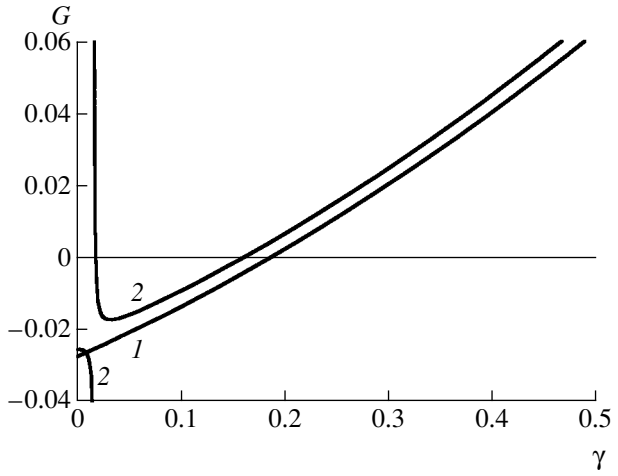

Fig. 1. Transcendental functions for the regimes of salt accumulation and salt precipitation. The parameters are T_0 = 283.15 K, T_a = 310 K, U = 1.119, ν_a = 0, and c_0 = (*1*) 0.0635 and (*2*) 0.1.

Transcendental curves *1* and *2* in Fig. 1 correspond to the regimes of salt accumulation ahead of the front and salt precipitation, respectively. As is seen, the first curve is monotonic and continuous for $0 < \gamma < \infty$, but it has a discontinuity at $\gamma = 0$. The unique point of intersection is the root of the system and, if $c_0 \longrightarrow 0$, this solution is transformed to the solution of the problem of the evaporation of pure water. When the initial salt concentration increases, there occurs a transition from the salt accumulation regime to the precipitation regime. Figure 1 also illustrates the appearance of a new second-order discontinuity at $\gamma = 0$, as well as the appearance of the second root in the neighborhood of the origin. The behavior of the transcendental curve is the same if the flow rate increases at a fixed initial concentration.

Calculations show that precipitate increases with the initial concentration and flow rate. As a result, the transcendental curve deforms and the roots converge. When the initial salt concentration or flow rate reaches the respective critical value, the roots coincide with each other and the transcendental curve touches the γ axis. Beyond the critical values, there are no roots of the transcendental equation and the curve lies above the abscissa axis (see Fig. 2). When the curve touches the axis and the roots coincide with each other, this condition provides the criterion for the existence of the similarity solution.

Figure 3 shows the roots of the transcendental equation as functions of the flow rate of ground water. As is seen, the roots coincide with each other for a certain critical value U and there is no solution above the critical flow rate. The upper part of the curve (solid line) corresponds to the root that has physical meaning, while the second part of the curve (dashed line) corresponds to the smaller γ values and has no physical meaning. The dependence of γ on the initial concentration is similar.

Figure 4 shows the porous-space fraction occupied with precipitate as a function of the flow rate of ground water. In this case, the lower part of the curve corresponds to the physical solution (first root) and the upper part corresponds to the second root, which has no physical meaning. This fact can be regarded as follows. A decrease in the flow velocity must lead to an increase in the front velocity and to the reduction of precipitate. The largest root γ (upper branch) and the lower branch of m_c correspond to this condition and may be regarded as the physical solution of the problem.

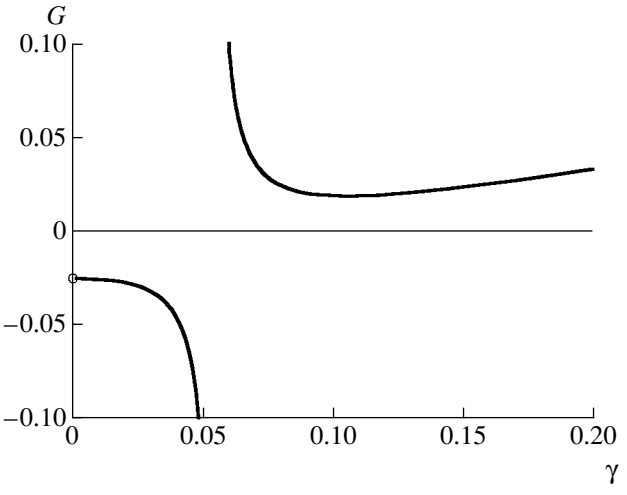

Fig. 2. Transcendental functions for the case in which the similarity solution of the problem is absent. The parameters are T_0 = 283.15 K, T_a = 310 K, U = 1.721, ν_a = 0, and c_0 = 0.1.

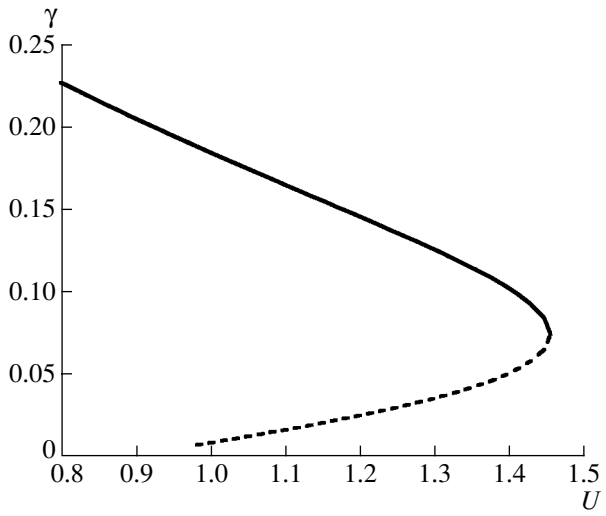

Fig. 3. Two solutions for the evaporation front velocity γ vs. the velocity of ground water for the same parameters as in Fig. 2. The dashed line is the solution that has no physical meaning.

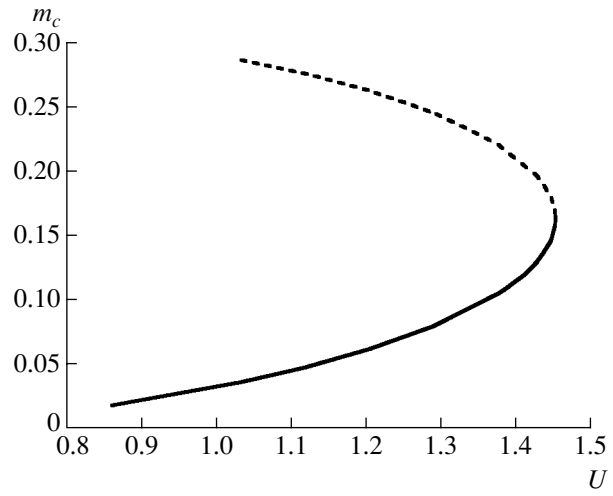

Fig. 4. Two solutions for the volume fraction saturated with salt in the solid state vs. the flow rate. The parameters are the same as in Fig. 2. The dashed line is the solution that has no physical meaning.

4. In this work, we have explored the similarity problem of salt precipitation due to the evaporation of ground water. Our analysis has established that there are two solutions for the same initial and boundary conditions. For the critical values of parameters, the roots of the transcendental equation coincide with each other and the solution of the problem ceases to exist. The absence of the similarity solution in a certain region of the parameters means that soil becomes clogged with salt near the ground surface when the similarity solution has not yet been formed. If the boundary values vary with time, clogging may occur at arbitrary depths, but this problem cannot be solved analytically. In [9], the problem of salt precipitation in geothermal systems was investigated, and there, too, more than one solution was obtained. We can assume that problems of precipitation are characterized by multivalued solutions, and the fusion of roots corresponds to porous space clogging and leads to the termination of a fluid flow. When the parameters approach their critical values, numerical simulation of these processes will be characterized by the deterioration of the convergence of numerical schemes.

ACKNOWLEDGMENTS

This work was supported by the Russian Foundation for Basic Research (project no, 03-01-00068) and the Council of the President of the Russian Federation for Support of Young Russian Scientists and Leading Scientific Schools (project no. NSh-1697.2003.1).

REFERENCES

1. W. Kleinitz, M. Koehler, and G. Dietzsch, SPE J., No. 68953 (2001).
2. A. Yakirevich, P. Berliner, and S. Sorek, Water Resour. Res. **33**, 1021 (1997).
3. A. Battistelli, C. Calore, and K. Pruess, Geothermics **26**, 437 (1997).
4. R. Helmig, *Multiphase Flow and Transport Processes in the Subsurface* (Springer, Berlin, 1997).
5. G. G. Tsypkin, Dokl. Akad. Nauk **389** (6), 759 (2003) [Dokl. Phys. **48**, 198 (2003)].
6. G. G. Tsypkin, Izv. Ross. Akad. Nauk, Mekh. Zhidk. Gaza, No. 6, 83 (2003).
7. M. P. Vukalovich, *Thermodynamic Properties of Water and Water Vapor* (MashGIZ, Moscow, 1955) [in Russian].
8. G. Tsypkin and L. Brevdo, Transp. Porous Media **37**, 129 (1999).
9. G. Tsypkin and A. Woods, in *Proceedings of XXI International Congress on Theoretical and Application Mechanics, Warsaw, Poland, 2004* (Warsaw, Poland, 2004).

Translated by G. Tsypkin

Doklady Physics, Vol. 50, No. 6, 2005, pp. 324–327. Translated from Doklady Akademii Nauk, Vol. 402, No. 6, 2005, pp. 762–765.

MECHANICS

On a Classical Variational Problem of Flight Dynamics

V. F. Krotov

Presented by Academician A.B. Kurzhanskiĭ December 10, 2004

Received December 23, 2004

FORMULATION OF THE PROBLEM

Flight dynamic problems associated with the launching of space rockets and maneuvers of high-speed aircrafts were the first applied problems to stimulate the development of the modern optimal control theory. These problems became important in the 1940s and 1950s in view of the necessity to minimize expensive and limited resources (amount of fuel, maneuver time, etc.). An appropriate technique for analyzing such problems is provided by calculus of variations. Certain of these flight dynamic problems became the first serious objects to which the latter classical section of mathematical analysis was applied. Many of the basic ideas associated with adapting variational calculus to modern control problems and modern optimal control theory were developed in investigations of flight dynamics. The first of these problems was to find a program for controlling the thrust of a jet engine of a rocket in order to ensure the maximum altitude when it rises vertically from the ground with a given amount of fuel by taking into account the effect of gravitation and air resistance. Goddard [1] was the first to point to the variational character of this problem: motion in a vacuum requires the fastest transformation of fuel to velocity and further free flight, whereas the atmosphere is an alternative factor that requires the deceleration of motion. Hammel [2] provided a strict formulation of this problem as a Boltza variational problem. Since instantaneous fuel consumption (infinite thrust) is assumed to be possible, the initial mass and velocity are not fixed (they are related by the Tsiolkovsky formula), nor are the final velocity, altitude, and time. Okhotsimskiĭ [3] solved this variational problem in an even more realistic formulation that took into account limited thrust. This result was important both for mathematical control theory and for the insights it provided into the features of the optimal trajectories of rockets. Constraints that are present in this problem for control functions are nonstandard for variational calculus, but they are characteristic of the modern control problem, and Okhotsimskiĭ proposed a method for the "direct analysis of variations," which included certain ideas that have more recently been completely developed in the Pontryagin maximum principle. The optimal trajectory is a sequence of rise–acceleration with the maximum thrust, motion in a special control regime, and free flight after the complete consumption of fuel. The Hammel problem was independently solved by Tsien and Evans [4]. Their solution is similar to the solution found in [3], where an instantaneous impulse was assumed instead of the acceleration with maximum thrust. The solutions obtained in [3] and [4] are based on the first-order necessary optimizing conditions of the variational calculus and they do not guarantee their optimum: their correction remains possible in theory. An approach based on the sufficient optimizing conditions of the controlled processes was proposed in [5].

The motion of the center of mass of the rocket is described by the equations

$$\frac{dx(t)}{dt} = f[x(t), u(t)], \quad u(t) \in U, \quad x(0) = x_0, \quad x(T) \in X_T. \tag{1}$$

Here, $x = (x^1, x^2, x^3)$ is the phase coordinate vector, X_T is the set of its admissible terminal values, $x^1 = V$ is the velocity of the rocket, $x^2 = h$ is the altitude, $x^3 = m$ is the mass, the control function u is the consumption of the working medium (fuel), U is the set of its admissible values,

$$f(x, u) = (f^1(x, u), f^2((x, u), f^3(x, u));$$

$$f^1(x, u) = \frac{(P - X - G)}{m}, \tag{2}$$

$$f^2(x, u) = V, \quad f^3(x, u) = -cu;$$

$P = cu$ is the jet thrust, c is the flow velocity of the working medium, $G = mg$ is the weight of the rocket, $g(h) > 0$ is the gravitational acceleration such that $\frac{dg(h)}{dh} < 0$ and $g(h) \longrightarrow 0$ for $h \longrightarrow \infty$, $X = c_x(h, \mathrm{M}) \times$

Institute of Control Sciences, Russian Academy of Sciences, Profsoyuznaya ul. 65, Moscow, 117997 Russia
e-mail: vfkrotov@ipu.ru

1028-3358/05/5006-0324$26.00

$\frac{\rho(h)V^2}{2}S$ is the aerodynamic drag, $\rho(h) > 0$ is the atmospheric density such that $\frac{d\rho(h)}{dh} < 0$ and $\rho(h) \longrightarrow 0$ for $h \longrightarrow \infty$; S is the effective wing area, $M = \frac{V}{a(h)}$ is the Mach number, $a(h)$ is the speed of sound, and $c_x(h, M)$ is the aerodynamic coefficient whose plot as a function of M for a fixed h has a pronounced hill with the maximum at M = 1. The controlled process is the motion of the rocket during an unfixed time interval $(0, T)$ with the phase coordinates h, V, and m and control function u. The constraints and boundary conditions have the form

$$U: u \geq 0, \quad x_0: V = 0, \quad h = 0, \quad m = m_0; \qquad X_T: m = m_1; \tag{3}$$

where m_0 and $m_1 < m_0$ is given positive numbers. Values $h(t)$ that can be reached according to Eqs. (1)–(3) are limited: $h(t) > b > 0$. Each allowable process is specified by the value T and functions $x(t) = (h(t), V(t), m(t))$ and $u(t)$, which are defined in the segment $[0, T]$ and satisfy Eqs. (1)–(3), as well as by the standard functional-theory restrictions: the function $u(t)$ is piecewise continuous and the function $x(t)$ is piecewise differentiable. It is necessary to find the sequence $\{\nu_s\}$ on the set D of the triples $\nu = [x(t), u(t), T]$ that minimizes the functional $J(\nu) = h(T)$:

$$J(\nu_s) \to \sup J(\nu), \quad \nu \in D. \tag{4}$$

The above-formulated variational problem of flight dynamics, whose history reaches back almost a century, has been analyzed in this work in the framework of the approach proposed in [5]. Its complete solution has been derived, considerably correcting the results obtained in [3, 4]. New solutions have been found and they have proven to be optimal; i.e., they ensure the absolute maximum of the reached altitude. Similar to [2, 4], instantaneous accelerations with infinite thrust are allowed, but they are obtained as the properties of a solution (so-called singular solution) rather than being formalized and fixed in time *a priori*. Since there is no constraint such as $u(t) \leq u_1$, the formulation of the problem is more idealized than that in [3]; at least in the case of sufficiently large u_1 values, though, the qualitative structure of the solution remains. New properties of the optimal control function appear. Indeed, this control was synthesized in [3, 4] as a sequence of the acceleration with maximum (infinite) thrust, the section of motion with a special continuous control regime (so-called special optimal control regime), and free flight after the consumption of fuel. At the same time, according to the results obtained in this work, there are two sections of the special regime—with subsonic and supersonic velocities—and two sections of the maximum thrust—the initial acceleration and acceleration near the sound threshold $V = a(h)$. The optimal regimes found in [3, 4] are also possible for certain parameters of the rocket.

SUFFICIENT OPTIMIZING CONDITIONS FOR THE CONTROLLED PROCESSES AND REDUCTION OF THE EQUATIONS OF MOTION

Here we recall some necessary information from [6]. Let conditions (1) describe a dynamic process with the n-dimensional vector of the phase coordinates x and r-dimensional control vector u. Problem (4) is formulated in application to such a system, with the functional of the form $J(\nu) = -F(x(T), T)$; i.e., the functional $I(\nu) = F[x(T), T]$ is minimized.

Definition. Let a pair of piecewise continuous functions $(x^*(t), u^*(t))$, where $x^*(t)$ is the discontinuous component, be defined in the segment $[0, T^*]$, and let the sequence $\{\nu_s\}$ converge to the triple $\nu^* = (x^*(t), u^*(t), T^*)$, i.e., $T_s \longrightarrow T^*$; $F(x_s(T_s), T_s) \longrightarrow F(x^*(T^*), T^*)$; for any $\varepsilon > 0$, the measure of the set $M_s(\varepsilon)$: $\min T_s, T^*) < t < \max(T^*, T_s)$, $|x_s(t) - x^*(t)| > \varepsilon$, $|u_s(t) - u^*(t)| > \varepsilon$, is infinitely small. Such a sequence $\{\nu_s\}$, as well as the set ν^*, is called a discontinuous solution of problem (4).

Let $\varphi(t, x)$ be a continuously differentiable function of time and coordinates and

$$R(x, u) = \Sigma_i f^i(x, u)\frac{\partial\varphi}{\partial x^i} + \frac{\partial\varphi}{\partial t}, \qquad G(x, t) = F(x, t) + \varphi(t, x). \tag{5}$$

Let $\varphi(t, x)$ and $\nu^* = (x^*(t), u^*(t), T^*) \in D$ exist such that

$$R(t, x^*(t), u^*(t)) = 0 = \max_{x, u} R(t, x, u) \ \forall t, \qquad G[x^*(T^*), T^*] = \min_{x, t} G(x, t).$$

In this case, the process ν^* is optimal.

Let u be a scalar such that $f(x, u) = f_1(x) + f_2(x)\,u$, $R(t, x, u) = R_1(t, x) + R_2(t, x)u$, $R_1(t, x) = \Sigma_i f_1^i(x)\frac{\partial\varphi}{\partial x^i} + \frac{\partial\varphi}{\partial t}$, and $R_2(t, x) = \Sigma_i f_2^i(x)\frac{\partial\varphi}{\partial x^i}$.

In this case, n-dimensional controlled system (1) is reduced to an $(n-1)$-dimensional system. The new vector $y = (y^1, y^2, y^{n-1})$ of the phase coordinates is related to x as the set of linearly independent solutions

$$y = Y(x) \tag{6}$$

of the linear homogeneous partial differential equation $R_2(t, x) = 0$ and

$$\frac{dy}{dt} = g(x), \quad g(x) = \Sigma_i f_1^i(x)\frac{\partial Y(x)}{\partial x^i}. \tag{7}$$

The new control is the vector x constrained by Eq. (6). By definition, the control program $x(t)$ for the new system may have first-order discontinuities, which is in contrast to the trajectory $x(t)$ of system (1). Let a pair $(y(t), x(t)$ satisfy Eqs. (6) and (7). In this case, at points where $x(t)$ is differentiable, there is a function $u(t)$ that satisfies Eq. (1).

Let $\Phi(y, T) = \min F(x,T)$: $x \in X_T$, $Y(x) = y$, and let the triple $w^* = (y^*(t), x^*(t), T^*)$ be a solution of the variational problem $I(w^*) \equiv \Phi(y^*(T^*), T^*) = \min_w$ under conditions (6) and (7). In this case, the program $x^*(t)$ that is complemented by the values $x^*(0) = x_0$, $x^*(T^*) = \arg\min_x F(x, T^*)$: $x \in X_T$, $Y(x) = y^*(T^*)$, together with the corresponding function $u^*(t)$, constitutes a discontinuous solution of problem (4) if this pair is consistent with the constraint $u^*(t) \in U$, including discontinuities of $x^*(t)$.

In application to the rocket motion,

$$R_2(x) \equiv \frac{c}{m}\frac{\partial \varphi}{\partial V} - \frac{\partial \varphi}{\partial m} = 0.$$

The expression

$$y = c\ln\frac{m_0}{m} - V \tag{8}$$

is a solution of this equation and, according to the above consideration, new phase coordinates h and y can be assigned. The new control $x = (V, h, m)$ has the only independent component and it is either V or m. Let it be V. According to Eqs. (7) and (8),

$$\frac{dh}{dt} = V, \quad \frac{dy}{dt} = g + \frac{X(h, V)}{m(y, V)}; \tag{9}$$

$$m(y, V) = m_0\exp\left(-\frac{y + V}{c}\right), \quad y(0) = 0, \quad h(0) = 0, \quad V \le B - y, \tag{10}$$

where $B = c\ln\frac{m_0}{m_1}$. The jumps $\Delta V(t) = V(t + 0) - V(t - 0)$ of the control function $V(t)$ are approximated by the sequence $u_s \longrightarrow \infty$, i.e., in the limit, by infinite thrust P instantaneously consuming a finite amount of fuel. Only jumps $\Delta V(t) \ge 0$ can be realized in view of the inequality $u \ge 0$. For any functions $V(t)$ satisfying Eq. (10), $\frac{dy(t)}{dt} > 0$. Reaching the constraint $V(t) = B - y(t)$ at $t = t^{**}$ means that the fuel has been completely consumed and flight is free uncontrollable motion with decreasing velocity [increasing $y(t)$] for $t > t^{**}$. If $y^{**} = y(t^{**}) < B$, there is $T^* > t^{**}$ such that $y(T^*) = B$ and, correspondingly, $V(T^*) = 0$, $h(t) < h(T^*)$ for $t > T^*$. This means that values $T > T^*$ and $h(T)$ are certainly nonoptimal.

SYNTHESIS OF OPTIMAL MOTION

Let

$$W(h, y, V) = V\left[g + \frac{X(h, V)}{m(y, V)}\right]^{-1},$$

$$V^*(h, y) = \arg\max_V W(h, y, V)\text{: } V \le B - y, \tag{11}$$

$$W^*(h, y) = \max_V W(h, y, V), \quad V \le B - y,$$

$(h^*(t), y^*(t))$ be the solution of the problem given by Eqs. (9) and (10) for $V(t) = V^*(t) = V^*(h(t), y(t))$, and

$$W^*(t) = W^*(h^*(t), y^*(t)).$$

Theorem. *Functions $h^*(t)$, $y^*(t)$, and $V^*(t)$ are defined in any segment $[0, T]$, $h^*(t)$ and $y^*(t)$ are piecewise differentiable, and $\frac{dy^*(t)}{dt} > 0$; $V^*(t)$ and the corresponding $m^*(t)$ are piecewise continuous and have no more than two discontinuities at $t = 0$ and $t = t^* > 0$: $W^*(t^* + 0) = W^*(t^* - 0)$. In this case, $\Delta V^*(t) \ge 0$, $\Delta m^*(t) \le 0$, $\frac{dm^*(t)}{dt} \le 0$; there is $t = t^{**} > t^*$ such that $m^*(t^{**}) = m_1$, $V^*(t) = B - y^*(t)$ for $t \ge t^{**}$; there is $T^* > t^{**}$ such that $y^*(T^*) = B$, $V^*(T^*) = 0$, and $h^*(T^*) = \max h^*(t)$ for any $t > 0$. The quintuplet $v^* = \left(V^*(t), h^*(t), m^*(t), u^*(t) = -\frac{dm^*}{dt}, T^*\right)$ is a discontinuous solution of problem* (4).

Proof. In view of Eqs. (8), (10), and $\frac{dy(t)}{dt} > 0$, we can write

$$\frac{dh}{dy} = W(h, y, V), \quad h(0) = 0, \quad V \le B - y. \tag{12}$$

Let $h^*(y)$ be a solution of Eq. (12) for $V = V^*(h, y)$ and $V^*(y) = V^*(h^*(y), y)$. We use the following property in application to Eq. (12). Let system (1) be one-dimensional, i.e., $x \in R$, $u(t, x) = \arg\max_u f(t, x, u)$, and $x^*(t)$ be the only solution of Eq. (1) complemented by the value $u = u(t, x)$ in the segment $[0, T]$ for fixed initial conditions. In this case, $x(t) \le x^*(t)$ for all t values and pairs $(x(t), u(t))$ satisfying Eq. (1), these initial conditions, and the above conditions of the theory of functionals. In application to Eq. (12), y, h, $V^*(h, y)$, and $h^*(y)$ play the roles of t, x, $u(t, x)$, and $x^*(t)$, respectively. It follows from Eq. (11) that the function $W^*(h, y)$ is a continuous, Lipschitz, and bounded function, $V^*(h, y) > 0$ and $W^*(h, y) > 0$ for the region given

by the inequalities $0 \le y < B$ and $0 \le h \le b$, and $V^*(h, B) = W^*(h, B) = 0$. Correspondingly, an increasing function $h^*(y)$ is defined in the segment $[0, B]$: it is a solution of Eq. (12) and is the exact upper boundary of the accessibility region of Eq. (12) for $V \le B - y$. The value $V^*(h(y), y)$ for $y = B$ lies on the upper boundary of the allowable velocities $V = B - y$, and further motion occurs along it. Since, as was mentioned above, $V^*(h(y), y) = B - y < 0$ for $y > B$ and $h^*(y)$ decreases, the maximum altitude is $h^*(B)$ or $h(T^*)$ in terms of Eqs. (9) and (10). The other statements of the theorem are proved as follows.

Analysis. It is easy to verify that the function $W(h, y, V)$ has the only maximum in V at $V^*(h, y) = V_c(h, y)$ if $c_x(h, \mathrm{M}) = \mathrm{const}$. The value $V_c(h(y), y)$ increases along the trajectory $h^*(y)$ up to the boundary value $V = B - y$. The plot of the real function $c_x(h, \mathrm{M})$ for a fixed h value has a pronounced hill with the maximum at $\mathrm{M} = 1$. This property is responsible for the minimum of the function $W(h, y, V)$ at $V_a(h, y)$ near $V = a(h)$ and two relative maxima at the subsonic point $V_1(h, y)$ and supersonic point $V_2(h, y)$ instead of the only maximum at the point $V_c(h, y)$. The value $V^*(h, y)$ coincides with one of these maximum points and increases along the trajectory $h^*(y)$ up to $y^{**} < B$, beginning with which $V^* = B - y$ and further to $y = B$. In this case, the difference $W[h, y, V_2] - W[h, y, V_1]$ increases and is positive for a sufficiently large parameter B at $y = y^{**}$; i.e., $V^*(y^{**}) = V_2(y^{**})$. Let this difference be negative at $t = 0$; i.e., $V^*(0, 0) = V_1(0, 0)$ [this property depends on the input rocket parameters $c_x(h, \mathrm{M})$, S, and B]. In this case, there is a time t^* where $W[h, y, V_2] = W[h, y, V_1]$ and the velocity displays a jump from $V_1(h, y)$ to $V_2(h, y)$.

As a whole, the optimal flight program consists of the following regimes.

(i) Instantaneous acceleration at $t = 0$ from $V = 0$ to $V^*(0, 0) = \arg\min_V W(0, 0, V)$. In dependence of the input rocket parameters, $V^*(0, 0)$ coincides with either $V_1(0, 0)$ or $V_2(0, 0)$. For low fuel resource $m_0 - m_1$, $V^*(0, 0) = B = c\ln\dfrac{m_0}{m_1}$ is also possible.

(ii) Then, if $W[0, 0, V_2(0, 0)] < W[0, 0, V_1(0, 0)]$, i.e., $V^*(0, 0) = V_1(0, 0)$, the following section of motion is determined by the law $V = V_1(h, y)$ and Eqs. (8) and (9), $u(t) = -\dfrac{dm}{dt}$ to the time $t = t^*$.

(iii) Instantaneous acceleration at $t = t^*$ from $V = V_1(h, y)$ to $V_2(h, y)$.

(iv) Motion that is determined by the law $V = V_2(h, y)$, the initial conditions $y(t^* + 0) = y(t^*)$ and $h(t^* + 0) = h(t^*)$, and Eqs. (8) and (9), $u(t) = -\dfrac{dm}{dt}$ to the time $t = t^{**}$: $V_2(h, y) = B - y$.

(v) Free flight to the time $t = T^*$: $y(T^*) = 0$ [$V(T^*) = 0$].

If $V^*(0, 0) = V_2(0, 0)$, the optimal motion for $t > 0$ is described by (iv) and (v). If $V^*(0, 0) = B$, the optimal motion for $t > 0$ is described by (v).

The maximizing sequence $\{v_s\}$ is constructed as follows. A numerical sequence $\{u_s > 0\} \longrightarrow \infty$ is assigned. For each s,

(a) the system given by Eqs. (1)–(3), which is complemented by the program $V_s(t) = c\ln\dfrac{m_0}{m_s(t)} - y_s(t)$, where $m_s(t) = m_0 - u_s t$, is integrated to the time $t = t_{1s}$: $V_s(t) = V_1(y_s(t), h_s(t))$;

(b) see (ii);

(c) see (a) for $m_s(t) = m(t^*) - u_s t$ to the time $t = t_{2s}$: $V_s(t) = V_{2s}(y_s(t), h_s(t))$;

(d) see (iv) and (v) [generally, $V_s(T^*) \ne 0$, but $V_s(T^*) \longrightarrow 0$].

Note 1. The above results provide the complete solution of the problem given by Eqs. (1)–(4) in which the jet thrust is not limited. In the presence of the constraint $u(t) \le u_1$ and for sufficiently large u_1, the structure of the solution remains the same with the following correction: the discontinuous trajectory that is specified by $h^*(t)$, $y^*(t)$, and $V^*(t)$ is changed to a trajectory similar to the elements of the sequence $\{v_s\}$ for $u_s = u_1$ with the correction of the onset time t_{2s} of the second acceleration section. For small u_1 values, specific trajectories may be unrealizable and an additional analysis is required.

REFERENCES

1. R. H. Goddard, Smithson. Misc. Collect. **71** (2) (1919).
2. G. Hammel, Z. Angew. Math. Mech., No. 7 (1927).
3. D. E. Okhotsimskiĭ, Prikl. Mat. Mekh. **10** (1946).
4. H. S. Tsien and R. S. Evans, J. Am. Rocket Soc. **21** (5), 99 (1951).
5. V. F. Krotov, V. Z. Bukreev, and V. I. Gurman, *New Variational Methods in Flight Dynamics* (Mashinostroenie, Moscow, 1969; Keter, Jerusalem, 1971).
6. V. F. Krotov, *Global Methods in Optimal Control Theory* (Marcel Dekker Inc., New York, 1996).

Translated by R. Tyapaev

Doklady Physics, Vol. 50, No. 6, 2005, pp. 328–332. Translated from Doklady Akademii Nauk, Vol. 402, No. 6, 2005, pp. 766–770.

MECHANICS

Three-Dimensional Formulation of the Novozhilov Criterion for Mode I Cracks

S. A. Nazarov

Presented by Academician N.F. Morozov December 20, 2004

Received May 19, 2005

Problems of brittle fracture mechanics are by nature three-dimensional, because, in addition to the determination of the onset of the quasi-static growth of a crack, it is necessary to determine the shape of the formed free surface, which significantly affects the fracture process but is rarely known *a priori*. The application of classical Griffith and Irwin, energy and stress, criteria to through cracks in thin plates under conditions of the generalized plane stress state represents only the leading approximation: it is not an unconditional result. Indeed, as was shown in [1], for the parallel transfer of the through-crack front, the relative increment of the total energy (surface energy + elastic energy – external-force work) determined by solving the two-dimensional problem differs from this increment as calculated for the three-dimensional problem by $O(\mathbf{h})$, where $\mathbf{h}$ is the relative thickness of the plate. Moreover, according to that work, the stress intensity factor $K_I(s)$ (a function of the arc length) on the crack front is indirectly related to the stress intensity factor K_I^0 (a scalar) at the vertex of a plane image of the crack.

For thick plates with cracks, which are most frequently used as experimental samples, the two-dimensional energy criterion is altogether inapplicable. This is because the latter involves the global characteristics of the stress–strain state, and two-dimensional analysis that is based on the stress criterion is difficult in view of the change in the order of singularities when approaching the end points $\mathbf{P}^\pm$ of the crack front, which are vertices of polyhedral angles, and the possible singularities of the function K_I at these points. If the exponent μ of the spatial singularity $O(\rho^{-\mu})$ of stresses at the points $\mathbf{P}^\pm$ is less than 1/2, $K_I(\mathbf{P}^\pm) = 0$ and the vertices hinder the quasi-static propagation of the entire edge of the through crack and form the local-fracture stage (cf. [1]). If $\mu > \frac{1}{2}$ and, correspondingly, $K_I(\mathbf{P}^\pm) = \infty$, the propagation of the crack begins near the vertices, and the aforementioned stage is dynamic. The above conclusions clearly refer to brittle fracture, and plastic effects can completely change the pattern. However, forecasts of crack propagation are approximate in any case, and the estimation of errors in this situation is complicated.

As was revealed in [2, 3] for two-dimensional problems, the quasi-static growth of cracks is of the variational nature. On this basis, variational asymptotic models of energy and stress criteria were formulated and analyzed in [4, 5], describing the quasi-static propagation of smooth fronts of mode I plane cracks in an elastic brittle medium. Mathematical formulation of the three-dimensional problem of fracture mechanics involves the variational inequality on the crack front. The solution of this inequality yields the critical load and front shape as functions of the timelike load parameter in a small range of variation in this parameter. Moreover, analysis of the variational inequality reveals the onset of the avalanche-like growth of the crack, as well as the possibility of crack bifurcation.

Numerous fracture criteria, in which a special structure of the crack mouth is postulated and fracture is associated with other physical processes, especially require three-dimensional formulations, because errors caused by the transition to the two-dimensional formulation of the problem can exceed and sometimes definitely do exceed the corrections associated with the introduction of additional parameters—the characteristics of the crack mouth—to the criterion. In this paper, a new three-dimensional formulation is proposed for the fracture criterion that was developed by Novozhilov in [6] for segment cracks and was applied [7–9] for other stress concentrators, mostly two-dimensional.

If M is a segment crack $\{y = (y_1, y_2): |y_1| \le l, y_2 = 0\}$ in a plane elastic body $\Omega \subset \mathbb{R}^2$ and load $p(y)$ is applied to its boundary, the growth of the crack at the vertex

Institute of Problems of Mechanical Engineering, Russian Academy of Sciences, Bol'shoĭ pr. 61, Vasil'evskiĭ Ostrov, St. Petersburg, 199178 Russia
e-mail: serna@snark.ipme.ru

1028-3358/05/5006-0328$26.00

$P^+ = (l, 0)$ can occur, according to Novozhilov, only under the condition

$$\frac{1}{d}\int_0^d \sigma_{22}(1+\eta, 0)d\eta = \sigma_c. \quad (1)$$

Here, y is the Cartesian coordinate system, l is the half-length of the crack, σ_{22} is the rupture stress in the y_1 axis, and the characteristic size d and theoretical critical stress σ_c of the material are the parameters of the fracture criterion. The integration in Eq. (1) along the segment that is a continuation of the crack means that the direction of the crack propagation is predefined, which is acceptable for symmetric data and, correspondingly, the stress state of the first mode near the crack vertex.

We emphasize that the above formulation of the criterion indicates only the *possibility of fracture*, but it does not answer the following questions: Does the crack grow? How does its length increase? Does the fracture process remain quasi-static? The three-dimensional case, in which the determination of the shape of the propagating crack is of primary importance, requires answers to these questions. For this reason, the initial formulation of the problem should be changed, introducing a new time scale that is longer than the real scale. This scale is associated with the loading process, and it justifies one in disregarding the inertial terms in the equations.

Let us consider the plane crack

$$M = \{x \in \mathbb{R}^3: y = (x_1, x_2) \in G, z = x_3 = 0\}$$

in the three-dimensional isotropic elastic brittle body Ω; i.e., the crack lies in the plane $\Pi = \{x: z = 0\}$ and has the profile $G \subset \Pi$. This profile is a closed set in the plane and it is bounded by the simple smooth contour Γ, which is the crack front. Mass forces are absent and loads $p(\tau; x)$ are applied to the surface $\partial\Omega$, where $\tau \in [0, \tau_0)$ is the timelike loading parameter (e.g., the relative force increment under simple loading). Let $M(\tau)$ be the position of the crack at the instant τ and $\Gamma(\tau)$ be its front. In this case, $M \subset M(\tau)$ (fracture is an irreversible process), but the case $M = M(\tau)$ (crack is at rest) is not excluded. Stresses arising in the body $\Omega\backslash M(\tau)$ under load $p(\tau; x)$ are denoted as $\sigma(\tau; x)$, and $\sigma_{zz}(\tau; y, 0)$ are rupture stresses in the crack plane Π. In the vicinity of the contour $\Gamma = \Gamma(0)$, we introduce the orthogonal curvilinear coordinate system (n, s, z), where s is the arc length in Γ and $|n|$ is the distance from Γ in the plane Π such that $n > 0$ beyond the set G. In the formula

$$\Gamma(\tau) = \{x: s \in \Gamma, n = h(\tau; s), z = 0\} \quad (2)$$

a nonnegative function $h(\tau; \cdot)$ arises, which indicates the depth of propagation of the front $\Gamma(\tau)$ at the point $s \in \Gamma$ (the same character is used for the point and its coordinate). Contours $\Gamma(\tau)$ are also parameterized by the variable $s \in \Gamma$ for small τ values, and $s(\tau)$ and $\kappa(\tau; s)$ are the corresponding point in $\Gamma(\tau)$ and the arc curvature, respectively. This curvature is positive for the convex case. Let $I_d(\tau; s) \subset \Pi$ be segments that begin at the points $s(\tau)$, have length d, and are directed along the outward normal vectors to $\Gamma(\tau)$.

A posteriori three-dimensional variant of criterion (1) is formulated as follows (cf. [5]). It is necessary to find a function $h \geq 0$ such that, for any small parameter $\tau \geq 0$ and all points $s \in \Gamma$, there is the alternative

$$h(\tau; s) > 0 \Rightarrow J(\tau; s) = \left(1 + \frac{d}{2}\kappa(\tau; s)\right)\sigma_s, \quad (3.1)$$

$$h(\tau; s) = 0 \Rightarrow J(\tau; s) \leq \left(1 + \frac{d}{2}\kappa(\tau; s)\right)\sigma_s. \quad (3.2)$$

Here,

$$J(\tau; s) = \frac{1}{d}\int_{I_d(\tau; s)} \sigma_{zz}(\tau; y(\tau; r, s), 0)(1 + r\kappa(\tau; s))dr, \quad (4)$$

where $y(\tau; r, s)$ is the point in the segment $I_d(\tau; s)$ and is spaced at a distance r from the front $\Gamma(\tau)$. Formulas (3.1) and (3.2) mean that, for the moving point $s(\tau)$ of the front $\Gamma(\tau)$, the stress that is averaged along the segment $I_d(\tau; s)$ (i.e., that is divided by

$$1 + \frac{1}{2}d\kappa = \frac{1}{d}\int_0^d (1 + r\kappa)dr,$$

which arises from the Jacobian of the transition to the curvilinear coordinates, see below) coincides with the theoretical critical stress σ_c and does not exceed this stress for an immovable point. We emphasize that the inequality

$$J(\tau; s) > \sigma_c\left(1 + \frac{1}{2}d\kappa(\tau; s)\right)$$

is impossible by the definition of the parameter σ_c, and a simultaneous satisfaction of the inequalities

$$h(\tau; s) > 0, \quad J(\tau; s) < \sigma_c\left(1 + \frac{1}{2}d\kappa(\tau; s)\right)$$

contradicts the criterion, because the latter of these inequalities means that the motion of point s must cease at a preceding instant in time.

One additional new property—the appearance of weighted average stresses in Eq. (4)—requires more detailed analysis. First, we consider the circle crack $M = \{x: |y| < R, z = 0\}$ that grows under an axisymmetric load and assume that the crack is developed conserving its symmetry; i.e., the problem is two-dimensional. According to the concept of microstructure fracture [6, 8] (the number of elementary fracture events is proportional to the area of the formed free surface Ξ_d),

Novozhilov criterion (1) for the circle crack has the form

$$\frac{1}{\pi d(2R+d)}\int_{\Xi_d}\sigma_{zz}(y,0)dy = \sigma_c. \quad (5)$$

Here, the denominator is the area of the ring $\Xi_d = \{y: R < |y| < R + d\}$. Due to axial symmetry, $\sigma_{zz}(y, 0) = \sigma_{zz}(R + r, 0)$ and equality (5) is transformed to

$$\frac{1}{d}\int_0^d \sigma_{zz}(R+r,0)(1+r\kappa)dr = \left(1+\frac{d}{2}\kappa\right)\sigma_c; \quad (6)$$

where $\kappa = \dfrac{1}{R}$ is the curvature of the crack front. It is seen that Eq. (6) is a partial case of the first of Eqs. (3).

We now continue our discussion of integral (4) for an arbitrary crack. The possibility of dealing with smooth crack fronts in bodies with a microstructure is ensured by a feature of the Novozhilov criterion: Eq. (1) contains the characteristic size d of the material, but stresses σ_{zz} are calculated without regard for microirregularities. For a one-dimensional crack, the size d is related to the diameter of a grain or a conglomerate of grains (see [8]), and it is reasonable to associate $\dfrac{\pi d^2}{4}$ for a two-dimensional crack with the area of the section of these irregularities. If dl is the arc length element on $\Gamma(\tau)$, $(1 + r\kappa(\tau; s))dl\,d\eta$ is the surface area element on Π, which is written in the curvilinear coordinates. Therefore, the integral formulation of criterion (3)

$$\int_{\Gamma(\tau)}\left(J(\tau;s)-\sigma_c\left(1+\frac{d}{2}\kappa(\tau;s)\right)\right)\times(\chi(\tau;s)-h(\tau;s))dl \le 0 \quad (7)$$

$$\forall\chi \in C^\infty(\Gamma(\tau)), \quad \chi \ge 0,$$

contains the integral over the strip that has width d and covers the contour $\Gamma(\tau)$ in the plane Π. Note that variational inequality (7) is derived from conditions (3) by the classical scheme. In particular,

$$\left\{J(\tau;s)-\sigma_c\left(1+\frac{1}{2}d\kappa(\tau;s)\right)\right\}h(\tau;s) = 0$$

according to Eqs. (3); i.e., Eq. (7) follows from point relations (3), because the test function χ is nonnegative. The inverse statement is also valid.

The presence of the Jacobian $1 + r\kappa$ on the right-hand sides of Eqs. (3) and (4) not only reflects the curvature of the crack front and corrects the calculation of the strip area, but also imposes a constraint: the product $d\max\{\kappa(s)\}$ must be small. The latter constraint agrees with the above feature of the Novozhilov criterion, because the microstructure of the material cannot be neglected during the averaging that occurs as part of the calculation of stresses near front sections, where the curvature radius is comparable with d. For two-dimensional problems, $\kappa = 0$ and no constraints are required.

The direct application of fracture criteria in the *a posteriori* formulation is very laborious, because elastic fields under the arbitrary perturbation of the crack front must be known in this case. For this reason, it is appropriate to construct their variational asymptotic models, which are based on asymptotic formulas for the stress–strain state and that lead to well posed mathematical problems. The use of the asymptotic formulas and the approximate inclusion of the effect of variations in the crack front require that the timelike parameter τ be small, as well as the stepwise application of a model in the case that a long-term forecast is necessary.

Let us construct a variational asymptotic model for the criterion given by Eq. (3) or (7) with the following additional assumption proposed in [8]: for small d values (compared to the contour curvature radius), the stress $\sigma_{zz}(\tau; y(\tau; s, r), 0)$ in integral (4) can be replaced by the leading term $(2\pi r)^{-1/2}K_I(\tau; s)$ of its expansion near the crack front. In [4], the asymptotic formula was obtained for the stress intensity factor on the front $\Gamma(\tau)$ under the symmetric (with respect to the plane Π) tensile stress $p(\tau; y) = p(y) + \tau p'(y) + O(\tau^2)$, which is applied to the faces of the crack $M(\tau)$ in the elastic homogeneous medium $\Omega = \mathbb{R}^3$:

$$K_I(\tau;s) \sim K_I(s) + \tau K_I'(s) + B(K_I h(\tau;\cdot);s) + \left\{q(s) - \frac{3}{8}\kappa(s) + \frac{1}{2}K_I(s)^{-1}k_I(s)\right\}K_I(s)h(\tau;s). \quad (8)$$

Here, $K_I(s) = K_I(0; s)$ and $k_I(s)$ are the coefficients in the representation

$$\sigma_{zz}(s, n, 0) = (2\pi n)^{-1/2}\{K_I(s) + k_I(s)n + O(n^2)\} \quad (9)$$

of stresses that are induced in the body $\mathbb{R}^3\backslash M$ by the load $p(y) = p(0; y)$, $K_I'(s)$ is the intensity factor that is induced on the front $\Gamma = \Gamma(0)$ by the load $p'(y) = \partial_\tau p(0; y)$, $\kappa(s) = \kappa(0; s)$ is the curvature,

$$B(H;s) = \int_\Gamma (H(t)-H(s))Q(t,s)dt, \quad (10.1)$$

is the integral operator with the symmetric positive kernel

$$Q(s,t) = Q(t,s) = (2\pi)^{-1}|s-t|^{-2} + O(1), \quad (10.2)$$

and $q(s)$ is the jump of the limited part of the indefinite integral $\Gamma\backslash\{s\} \ni t \mapsto Q(s, t)$ that arises when regularizing the hypersingular integral in Eq. (10.1).

Let the crack M be completely open by load p, more specifically, $K_I(s) > 0$ for $s \in \Gamma$. We introduce the dimensionless parameter $\beta = d\max\{K_I(s)^{-1}k_I(s), \kappa(s)\}$, which should be small enough to ensure the above

replacement for $\sigma_{zz}(\cdot)$ in Eq. (4) [$K_I(s)^{-1}k_I(s)$ cannot be introduced into max when the gradients of normalized stresses $r^{1/2}\sigma(0; x)$ are large]. In addition, similar to [4, 5], we introduce the following new unknown in terms of h from Eq. (2):

$$H(\tau; s) = K_{Ic}^{-1}K_I(s)h(\tau; s), \tag{11}$$

where K_{Ic} is the critical stress intensity factor such that $K_{Ic} = \left(\frac{\pi d}{2}\right)^{1/2}\sigma_c$ in agreement with [8]. Substituting expansions (8) and (9) into Eqs. (3) and (4), omitting terms that are small compared to $O(\tau + \beta)$, and performing simple transformations, we arrive at the variational inequality

$$\int_\Gamma (b(s)H(\tau; s) - B(H(\tau; \cdot); s))(X(s) - H(\tau; s))dl \tag{12}$$
$$\geq \int_\Gamma F(\tau; s)(X(s) - H(\tau; s))dl \ \forall X \in C^\infty(\Gamma), \quad X \geq 0,$$

where B is the integral operator given by Eq. (10.1), b is the quantity opposite to the expression in the braces in Eq. (8), and

$$F(\tau; s) = -1 + \frac{1}{K_{Ic}}(K_I(s) + \tau K_I'(s)) + \frac{1}{3}\frac{d}{K_{Ic}}(k_I(s) + \kappa(s)K_I(s)) - \frac{d}{2}\kappa(s). \tag{13}$$

We emphasize that all quantities entering into inequality (12) are obtained by solving problems of elasticity theory for a given initial position of the crack. Determining the solution H of this inequality, we reconstruct the shape of the crack front at the time instant τ according to Eqs. (2) and (11). As was shown in [4], the properties of the integral operator B ensure the correct formulation of inequality (12) on the convex cone

$$W_2^{1/2}(\Gamma)_+ = \{X \in W_2^{1/2}(\Gamma): X \geq 0\}$$

in the Sobolev–Slobodetskiĭ space [in particular, the test function X in inequality (12) is taken from the cone $W_2^{1/2}(\Gamma)_+$]. Moreover, when $b > 0$, problem (12) has the unique solution $H \in W_2^{1/2}(\Gamma)_+$ for any right-hand side $F \in L_2(\Gamma)$. In this case, if $F \in L_p(\Gamma)$ and $p \in [2, +\infty)$, then $H \in W_p^1(\Gamma)$ (the smoothness of the solution increases) and there is the estimate

$$\|H; W_p^1(\Gamma)\| \leq C_p\|F + |F|; L_p(\Gamma)\|.$$

Analysis of variational inequality (12) shows that

(i) if there is only a trivial solution, the crack is at rest;

(ii) if there is the unique small solution, the propagation of the crack is quasi-static and stable;

(iii) if there are several small solutions, the bifurcation of the shape of the crack front can occur;

(iv) if small solutions do not exist, the propagation of the crack is avalanche-like, and the above analysis is invalid in the case that the dynamic effects are not included.

If the load increases, $K_I'(s) \geq 0$, and the start of the crack occurs at $\tau = 0$ [for small $\tau < 0$, inequality (12) has only the trivial solution $H = 0$], then function (13) must satisfy the relation

$$F(0; s) \leq 0, \quad s \in \Gamma, \tag{14}$$

and have a zero global maximum. It is easy to see that the last term in Eq. (13) is negligibly small only when β is infinitesimal. Therefore, the critical load according to Novozhilov coincides with the critical load obtained according to the Irwin criterion from the condition $\max\{K_I(s)\} = K_{Ic}$ (see [4]). Recall that the stress and energy three-dimensional fracture criteria yield identical loads under which the crack loses stability. However, owing to positive curvature $\kappa(s)$ for convex cracks, the former criterion predicts a deeper propagation of the front than the does the latter (see [5, 10]).

According to Eqs. (13) and (14), fracture on concave sections of the front Γ begins earlier than fracture on convex sections under other identical conditions. Asymptotic formulas that were obtained in [11] for the front $\Gamma(\tau)$ of the crack $M(\tau)$ for small τ values are applicable to model (12) of the three-dimensional Novozhilov criterion. In this case, similar to other models, the local fracture (crack shoot) is characterized by the singular perturbation of the front Γ: the first derivative of the function h from Eq. (2) with respect to τ is equal to zero at $\tau = 0$, and the second derivative does not exist. This effect appears due to different velocities (in terms of the timelike parameter τ) $O(\tau^{3/2})$ and $O(\tau^{1/2})$ of the depth and lateral propagations of the branch, respectively. The irregular behavior of front (2) at the initial stage of propagation is responsible for the paradoxical result $\partial_\tau h(0; s) = h_0\delta(s - s_0)$ that was obtained in some investigations using classical asymptotic analysis methods. This formula contains the Dirac delta function δ and signifies that only one point s_0 starts from the entire front Γ. These features of the solutions to variational models of fracture criteria were discussed in detail in [5].

In contrast to the three-dimensional fracture criteria analyzed in [4, 5], the Novozhilov criterion given by Eq. (3) or (7) is applicable to the problem associated with the growth of a through crack in a thick plate, which was mentioned at the beginning of this paper, as it is independent of a specific form of stress singularities. At the same time, it is difficult to develop a variational asymptotic model for the criterion that is similar

to the model given by Eq. (12), because there are no asymptotic formulas for the increment of the stress intensity factor under variation in the edge of the through crack. When the asymmetric growth of the segment crack in the plane elastic body is admissible, criterion (1) should also be reformulated as a variational algebraic inequality (cf. [10]).

ACKNOWLEDGMENTS

This work was supported by the Russian Foundation for Basic Research (project no. 03-01-00838).

REFERENCES

1. S. A. Nazarov, Prikl. Mat. Mekh. **55**, 500 (1991).
2. E. M. Morozov, Dokl. Akad. Nauk SSSR **184** (6), 1308 (1969) [Sov. Phys. Dokl. **14**, 181 (1969)].
3. S. Nemat-Nasser, Y. Sumi, and L. M. Keer, Int. J. Solids Struct. **16**, 1017 (1980).
4. S. A. Nazarov, Mekh. Tverd. Tela, No. 2, 152 (1989).
5. S. A. Nazarov and O. R. Polyakova, Mekh. Tverd. Tela, No. 2, 101 (1992).
6. V. V. Novozhilov, Prikl. Mat. Mekh. **33** (5), 797 (1969).
7. N. F. Morozov, Dokl. Akad. Nauk SSSR **253** (6), 1336 (1980) [Sov. Phys. Dokl. **25**, 656 (1980)].
8. N. F. Morozov and V. V. Novozhilov, Fiz.-Khim. Mekh. Mater. **24** (1), 21 (1988).
9. N. F. Morozov and Yu. V. Petrov, *Problems of Dynamic Fracture in Solids* (S.-Peterb. Gos. Univ., St. Petersburg, 1990) [in Russian].
10. S. A. Nazarov, Prikl. Mat. Mekh. **64**, 484 (2000).
11. L. G. Kolton and S. A. Nazarov, Mekh. Tverd. Tela, No. 3, 125 (1997).

Translated by R. Tyapaev